WWU
MÜNSTER

Calibration and background reduction of the KATRIN experiment

Mariia Fedkevych née Kostina, Dissertation 2019

wissen.leben
WWU Münster

Institut für Kernphysik

Westfälische Wilhelms-Universität Münster

Experimentelle Physik

Calibration and background reduction of the KATRIN experiment

Inaugural-Dissertation
zur Erlangung des Doktorgrades
der Naturwissenschaften im Fachbereich Physik
der Mathematisch-Naturwissenschaftlichen Fakultät
der Westfälischen Wilhelms-Universität Münster

vorgelegt von
Mariia Fedkevych geb. Kostina
aus Cherson, Ukraine
- 2019 -

Dekan:	Prof. Dr. Gerhard Wilde
Erste Gutachter:	Prof. Dr. Christian Weinheimer
Zweiter Gutachter:	Prof. Dr. Alexander Kappes
Tag der mündlichen Prüfung:	.....
Tag der Promotion:	.....

"Why do you believe what you believe? What do you think you know and how do you think you know it?"

— Eliezer Yudkowsky

Abstract

Neutrino masses, recently proven to be non-zero by neutrino oscillation experiments, are important parameters in particle and nuclear physics, as well as in cosmology and astrophysics, but they were not measured until now. There are several experiments trying to determine neutrino masses. The low-background KArlsruhe TRItium Neutrino experiment (KATRIN), as well as its predecessors in Mainz and Troitsk which were able to put independently an upper limit of $\sim$2 eV for the neutrino mass, is based on a direct model-independent way to determine average electron neutrino mass from the kinematics of tritium β-decay. It considers β-spectrum in the endpoint region using MAC-E spectroscopy technique. KATRIN is aiming to reach the sensitivity of 0.2 eV (90% C.L.) in 3 years of pure measurement time; already from four weeks of data taking, it has pushed the experimental limit down to 1.1 eV.

KATRIN measures the energy of β-decay electrons emitted in Windowless Gaseous Tritium Source (WGTS) via a tandem of so-called pre- and main spectrometers (MAC-E-filters). In the region between the two spectrometers, a Penning trap is created by the combination of retarding potentials of -18.3 kV in the pre-spectrometer and -18.6 kV in the main spectrometer together with a magnetic field of about 4.5 T (nominal value) produced by a common superconducting magnet.

Even at the ultra-high vacuum conditions of KATRIN, electrons lose energy due to synchrotron radiation and (in)elastic scattering with residual gas. It leads to their accumulation in the trap causing background increase which raises the statistical uncertainty of the experiment. They could even produce discharges which may interrupt the data-taking process and damage parts of the spectrometer and detector section of KATRIN. As have been demonstrated in tests of the system at various pressure conditions, higher pressure leads to higher background level and less time for a discharge formation. As a countermeasure, three pneumatically-driven *electron catchers* (Inconel rods) were implemented in the beamline part between the two spectrometers. Trapped electrons are guaranteed to hit an inserted catcher within one magnetron turn (on a sub-ms scale). As is demonstrated in the present work, the electron catchers proved to have a good efficiency to quench discharges at up to $\sim 10^{-9}$ mbar therefore being a perfect safety measure in case of possible discharge appearance. Keeping the spectrometer pressure at the nominal level of the order of 10^{-11} mbar is crucial to sufficiently suppress the Penning trap contribution to the KATRIN background.

For the absolute energy calibration monitoring and precise determination of transmission functions of pre- and main spectrometers (vital to allow KATRIN to reach its sensitivity goal), among the other sources a Condensed Krypton Source (CKrS) is used. It has been developed at the University of Münster and was installed at the KATRIN cryogenic pumping section (CPS) at the Karlsruhe Institute of Technology (KIT) in 2017. Its core component is a 4 cm^2 HOPG (highly oriented pyrolytic graphite) substrate on which gaseous $^{83\mathrm{m}}$Kr is condensed. This makes the CKrS a point-like source which in combination with an ability to be moved in vertical and horizontal directions across the flux tube allows per-pixel calibration of the KATRIN focal plane detector (FPD) with comparatively high rates. It can be exploited for frequent measurements due to its relative operational simplicity comparing to the gaseous $^{83\mathrm{m}}$Kr source (GKrS) which KATRIN is using as another calibration source.

The cleanliness of the substrate and quality of frozen radioactive films are crucial for the source characterization and control of the stability and reproducibility of the conversion electron spectrum.

At the CKrS this is monitored by means of laser ellipsometry which allows to extract information about film thickness growth with a conservatively estimated uncertainty of 2.4 Å. In this thesis, analysis of the ellipsometry data and comparison with the spectroscopic data in terms of line stability from measurements with the CKrS in krypton campaigns of 2017 and 2018 are discussed.

Zusammenfassung

Neutrinomassen, die vor kurzem mit Neutrinoszillationsexperimenten als ungleich Null erwiesen wurden, sind wichtige Parameter in der Teilchen- und Kernphysik sowie in der Kosmologie und Astrophysik, wurden aber bisher nicht gemessen. Es gibt mehrere Experimente, die versuchen, Neutrinomassen zu bestimmen. Das KArlsruhe TRItium Neutrino-Experiment (KATRIN) sowie seine Vorgänger in Mainz und Troitsk, die unabhängig voneinander eine Obergrenze von $\sim$2 eV für die Neutrinomasse festlegen konnten, basiert auf einer direkten modellunabhängigen Methode zur Bestimmung der durchschnittlichen Elektronneutrino-Masse aus der Kinematik des Tritium β-Zerfalls. Es untersucht das β-Spektrum im Endpunktbereich mittels MAC-E-Spektroskopietechnik. KATRIN strebt danach, die Sensitivität von 0.2 eV zu erreichen (90% C.L.) in 3 Jahren reiner Messzeit; bereits nach vier Wochen Datenaufnahme hat es die obere experimentelle Grenze auf 1.1 eV gesenkt.

KATRIN misst die Energie von β-Zerfallelectronen, die von einer fensterlosen gasförmigen tritium Quelle (Windowless Gaseous Tritium Source, WGTS) stammen, mittels eines Tandems von sogenannten Vor- und Hauptspektrometern (MAC-E-Filtern). Im Bereich zwischen den beiden Spektrometern entsteht eine Penningfalle durch die Kombination von Retardierungspotentialen von -18.3 kV im Vorspektrometer und -18.6 kV im Hauptspektrometer zusammen mit einem Magnetfeld von etwa 4.5 T (Nennwert), der durch einen gemeinsamen supraleitenden Magneten erzeugt wird.

Selbst unter den Ultrahochvakuumbedingungen von KATRIN verlieren Elektronen durch Synchrotronstrahlung und (un)elastische Streuung mit Restgas Energie. Es führt zu ihrer Anhäufung in der Falle, was zu einer Zunahme des Untergrundes und der statistischen Unsicherheit des Experiments führt. Sie könnten sogar Entladungen erzeugen, die den Datenerfassungsprozess unterbrechen und Teile des Spektrometers und des Detektors von KATRIN beschädigen könnten. Wie in Tests des Systems unter verschiedenen Druckbedingungen gezeigt wurde, führt ein höherer Druck zu einem höheren Untergrundwert und zu kürzeren Zeiten für eine Entladungsbildung. Als Gegenmaßnahme wurden drei pneumatisch angetriebene *Elektronenfänger* (Inconel-Stäbe) im Strahllinienteil zwischen den beiden Spektrometern implementiert. Die eingeschlossenen Elektronen treffen garantiert innerhalb einer Magnetronumdrehung (auf einer Subms-Skala) auf einen eingesetzten Fänger. Wie in der vorliegenden Arbeit gezeigt, haben die Elektronenfänger eine gute Effizienz beim Löschen von Entladungen bei Drücken bis zu $\sim 10^{-9}$ mbar und sind somit eine perfekte Sicherheitsmaßnahme bei einem möglichen Auftreten von Entladungen. Das Halten des Spektrometerdrucks auf dem nominalen Druckniveau in der Größenordnung von 10^{-11} mbar ist entscheidend, um den Beitrag der Penningfalle zum KATRIN-Untergrund ausreichend zu unterdrücken.

Für die absolute Energiekalibrierung Überwachung und präzise Bestimmung von Transmissionsfunktionen von Vor- und Hauptspektrometer (wichtig, damit KATRIN sein Sensitivitätsziel erreichen kann), unter den anderen Quellen wird eine kondensierte Kryptonkonversionselectronenquelle (CKrS) verwendet. Sie wurde an der Universität Münster entwickelt und in 2017 im KATRIN Kryopumpenbereich (Cryogenic Pumping Section, CPS) am Karlsruher Institut für Technologie (KIT) installiert. Ihre Kernkomponente ist ein 4 cm^2 HOPG (hochorientierter pyrolytischer Graphit) Substrat, auf dem gasförmiges ^{83m}Kr kondensiert ist. Dies macht die CKrS zu einer punktförmigen Quelle, die in Kombination mit der Möglichkeit, sich in vertikaler und horizontaler Richtung über

das Flussschlauch zu bewegen, eine Pro-Pixel-Kalibrierung des KATRIN-Focal-Plane-Detektors (FPD) mit vergleichsweise hohen Raten ermöglicht. Es kann für häufige Messungen genutzt werden, da es im Vergleich zu der gasförmigen ^{83m}Kr-Quelle (GKrS), die KATRIN als weitere Kalibrierquelle verwendet, relativ einfach zu bedienen ist.

Die Sauberkeit des Substrats und die Qualität der gefrorenen radioaktiven Schichten sind entscheidend für die Quellencharakterisierung und kontrolle der Stabilität und Reproduzierbarkeit des Konversionselektronenspektrums. Bei der CKrS wird dies mittels Laser-Ellipsometrie überwacht, die es ermöglicht, Informationen über das konservativ geschätzten Schichtdickenwachstum mit einer Unsicherkeit von 2.4 Å zu extrahieren. In dieser Arbeit werden die Analyse der Ellipsometriedaten und der Vergleich mit den spektroskopischen Daten in Bezug auf die Linienstabilität aus Messungen mit dem CKrS in Kryptonmesskampagnen von 2017 und 2018 diskutiert.

Acknowledgments

I would like to express my sincere gratitude to my supervisor, Christian Weinheimer, for accepting me as a PhD student, providing me an interesting research topic and for all his support, suggestions and encouragement during my PhD time. His guidance helped me immensely in all the time of research and writing of this thesis.

I would like to thank all the board members of the Research Training Group "GRK 2149: Strong and Weak Interactions - from Hadrons to Dark Matter" for accepting me as an associated GRK student which allowed me to take an advantage of the excellent qualification programme with all its valuable courses, workshops, scientific and educational events. My PhD training within the framework of "GRK 2149" included three months of work on a theory side project dedicated to a review of possible explanations for the observation of ultra-high energy neutrinos in various theoretical extensions of the Standard Model. I would like to thank to my second supervisor, Anna Kulesza, for guiding my work on this project.

I also would like to express my gratitude to Volker Hannen for all his help with my experimental research and proofreading the thesis. I would like to thank Alexander Kappes for accepting to be the second referee for my PhD thesis. I also acknowledge my fellow working group mates and all members of the Institute of Nuclear Physics and the Institute of Theoretical Physics of the University of Münster, the Institute of Nuclear Physics of the Karlsruhe Institute of Technology and the KATRIN collaboration for a warm and friendly atmosphere and fruitful discussions.

I would like to thank my family and friends, and especially my parents Kateryna and Vladyslav, my husband Oleh, my parents-in-law Tatyana and Oleh for all their love and support throughout all the years.

Contents

Chapter 1

Introduction

1.1 A short historical overview of neutrino physics

Neutrinos play an essential role in particle physics and in theories of structure formation in the Universe. Their nature and properties were actively studied since their discovery. About a hundred years ago people were puzzled with behavior of nuclear β-decay. Experimental data of Chadwick [Cha14] showed that the energy of electrons emitted in the decay is continuously varying over a wide range while it was expected that a β-decay should generate electrons of a strictly defined energy. In the context of a two-body problem, which it was believed to be at this time, this anomaly could only be explained by a violation of fundamental conservation laws, which was considered to be too much of a sacrifice. In 1930 as a "desperate remedy" W. Pauli postulated in his letter [Pau] to the participants of a physics conference in Tübingen a neutral $\frac{1}{2}$ spin particle which carries away a part of the energy lost by the mother nucleus so that in each β-decay the sum of its energy and the electron's energy is constant. In 1933-1934 E. Fermi established a mathematical theory of β-decay involving the new particle which he renamed as "neutrino". He explained its appearance in a different way than W. Pauli: while the latter considered neutrino to be present in the nucleus already before its decay, Fermi assumed it to be born in the conversion of a neutron into a proton and an electron [Fer34].

Neutrino have been recognized to have an extraordinary penetrating ability: H. Bethe and R. R. Peierls calculated that a neutrino with MeV energy can travel through a 1000 light years thick liquid hydrogen layer [BP34]. Despite of the seeming detection impossibility, its existence was confirmed by the Reines and Cowan experiment in 1956 [Cow+56]. As a neutrino source they used a nuclear reactor of the Savannah River complex. According to the Fermi theory, an antineutrino colliding with a proton produces a neutron and an electron (inverse β-decay). Those interactions were registered by detectors surrounding a container filled with cadmium chloride via a reaction chain $\bar{\nu}_e + p \to e^+ + n$, $n + {}^{108}\mathrm{Cd} \to {}^{109\mathrm{m}}\mathrm{Cd}^* \to {}^{109}\mathrm{Cd} + \gamma$.

The muon neutrino produced together with a muon in pion decays $\pi^+ \to \mu^+\nu_\mu$ was first discovered in 1962 by Lederman, Schwartz and Steinberger [Dan+62]. And only in 2000 the DONUT collaboration proved the existence of the third sort of neutrino - ν_τ [Kod+01] in the reaction sequence $D_S \to \tau\nu_\tau$, $\tau \to \nu_\tau X$, producing ν_τ and $\bar{\nu}_\tau$ every $D_S \to \tau$ decay.

Neutrinos are one of the most abundant particle species in our Universe and, despite of their weak interaction with matter, a large amount of knowledge about them has been gained since their

discovery. Oscillations of neutrinos and, therefore, their massiveness, which is discussed in the next section, were discovered by atmospheric (Super-Kamiokande [Fuk+99]), solar (SNO [Sno]) and reactor (KamLAND [Egu+03]) experiments. This fact points to new physics since in the Standard Model neutrinos do not possess mass. Still, individual masses of neutrinos, as well as some aspects of their mixing, are not known yet, while they are important parameters in many cosmological and BSM (Beyond the Standard Model) theories. In the next section, neutrinos in the Standard Model and theory of neutrino oscillations is briefly discussed. Also, another exciting feature connected to these particles was discovered recently - the existence of cosmic neutrinos of extremely high (TeV-PeV range) energies. Many cosmic sources are considered as their possible birthplaces. Interestingly, apart from the old physics models, various BSM models were proposed to explain their generation mechanisms. Some of them, specifically in the connection to the IceCube experiment, are discussed in appendix A.

1.2 Neutrinos in the Standard Model

The weak interaction involving neutrinos maximally violates P-parity and this phenomenon gave a key to build the Standard Model where leptons and quarks are combined in left-handed[1] doublets

$$L = \begin{pmatrix} \nu_L^\alpha \\ l_L^\alpha \end{pmatrix} \tag{1.1}$$

for leptons, where $\alpha = e, \mu, \tau$, and

$$Q = \begin{pmatrix} U_L \\ D_L \end{pmatrix} \tag{1.2}$$

for quarks, where $U = (u, c, t)$ and $D = (d, s, b)$.

One of the main features of the Standard Model is its ability to explain masses of elementary particles within a frame of the spontaneous symmetry breaking called Higgs mechanism which generalizes the Goldstone theorem which says that spontaneous breaking of global symmetry leads to the appearance of a massless and spinless particle - a Goldstone boson, in case of breaking local symmetry.

In practice, we make the assumption that the Universe is filled with a spin-0 field, so called Higgs field, which is a doublet in SU(2) space, carries a nonzero U(1) hypercharge and is a singlet in color space. It can be represented as

$$\phi = \begin{pmatrix} \phi^+ \\ \phi^0 \end{pmatrix}, \tag{1.3}$$

where ϕ^+ is a charged field and ϕ^0 is a neutral one. These fields are complex

$$\phi^+ = \frac{1}{\sqrt{2}}(\phi_1 + i\phi_2), \tag{1.4}$$

[1] left(right)-handed field is defined as $\psi_{L,R} \equiv \frac{1}{2}(1 \mp \gamma_5)\psi$

$$\phi^0 = \frac{1}{\sqrt{2}}(\phi_3 + i\phi_4). \tag{1.5}$$

A Lagrangian of this field is added into the Lagrangian of the Standard Model

$$\mathcal{L} = |D_\mu \phi|^2 - \frac{\lambda^2}{4}(|\phi|^2 - v^2)^2. \tag{1.6}$$

It has a minimum of self-interaction potential for a nonzero vacuum average of the field $v = \langle 0|\phi^0|0\rangle$. This has a consequence that the Lagrangian and the motion equations are invariant under a global calibration transformation

$$\phi(x) \to \phi'(x) = e^{i\alpha_i \tau_i/2}\phi(x), \tag{1.7}$$

(where α is an arbitrary number and τ are Pauli matrices) while their solutions may not be due to spontaneous falling in one of the local minima. As a result of this spontaneous symmetry breaking, the Lagrangian gives nonzero masses to three linear combinations (*i.e.* physical states) of the four gauge bosons W^1, W^2, W^3, B:

$$W^\pm_\mu = \frac{1}{\sqrt{2}}(W^1_\mu \pm iW^2_\mu),\ Z_\mu = \cos\theta_W W^3_\mu - \sin\theta_W B_\mu \tag{1.8}$$

with

$$\cos\theta_W = \frac{g}{\sqrt{g^2 + g'^2}}, \tag{1.9}$$

which correspond to the appearance of $W^\pm$- and Z-bosons respectively, with masses

$$m_{W^\pm} = \frac{gv}{2} \text{ and } m_Z = \frac{gv}{2\cos\theta_W}. \tag{1.10}$$

and one of the gauge fields remains massless:

$$A_\mu = \cos\theta_W B_\mu + \sin\theta_W W^3_\mu,\ m_\gamma = 0. \tag{1.11}$$

After combining the Higgs fields in the SU(2) doublet, one postulates an SU(2)-invariant interaction of fermions with the Higgs fields, called Yukawa interaction, which is given by the term in the Lagrangian

$$\mathcal{L}_{Yukawa} = -\lambda_e \bar{l}_L \phi e_R - \lambda_u \bar{q}_L \phi^c u_R - \lambda_d \bar{q}_L \phi d_R + h.c. + (\text{for 2nd and 3rd generations}) \tag{1.12}$$

where $l_L = \begin{pmatrix}\nu_L \\ e_L\end{pmatrix}$, $q_L = \begin{pmatrix}u_L \\ d_L\end{pmatrix}$, $\phi^c = i\sigma_2\phi^* = \begin{pmatrix}\phi^*_0 \\ -\phi^-\end{pmatrix}$ with $\phi^- = \frac{1}{\sqrt{2}}(\phi_1 - i\phi_2)$. After application of the Higgs mechanism, the masses of the particles are generated: $m_e = \lambda_e \frac{v}{\sqrt{2}}$, $m_u = \lambda_u \frac{v}{\sqrt{2}}$ and $m_d = \lambda_d \frac{v}{\sqrt{2}}$ being masses of the electron, u- and d- quarks respectively (and analogously for the other generations). However, in general case the fields from different doublets can interact with each other. Therefore, the coupling constants in eq. (1.12) turn into matrices λ_{ij} which implies that after a spontaneous symmetry breaking one gets the "mass therms" proportional to $m_{ij} = \lambda_{ij}\frac{v}{\sqrt{2}}$. Therefore, in order to interpret the elements of m_{ij} as physical masses one has to diagonalize it in terms of new fields which are linear combinations of massless interaction fields. The unitary matrix U, connecting mass eigenstates with massless interaction fields for quarks is known as CKM

(Cabibbo-Kobayashi-Maskawa) mixing matrix, and analogously the matrix for neutrinos is known as PMNS (Pontecorvo–Maki–Nakagawa–Sakata) matrix [2].

In the considered theory, no "mass term" for neutrinos appears. Formally it is connected to the presence of only the left-handed neutrino and the right-handed antineutrino and the absence of the right-handed neutrino state. However, there are multiple indications that the Standard Model cannot be considered as a complete theory: for example, it does not explain dark matter and the baryon asymmetry of the Universe, as well as inflation and the nature of cosmological perturbations. Moreover, it has been found that neutrinos in fact have non-vanishing masses, which was discovered in oscillation experiments. Neutrino oscillations and their connection to neutrino masses is discussed in the next section.

1.3 Neutrino oscillations and masses

When lepton family numbers L_e, L_μ, L_τ are not conserved quantum numbers and if neutrinos have non-zero masses, then a transformation of a neutrino from one type into another is possible. This process can be described in terms of quantum mechanics as neutrino oscillations (see, for example, [GK07]).

These oscillations, *i.e.* change of the flavor after a propagation over a certain distance, happen due to the fact that the flavor states of neutrinos $|\nu_\alpha\rangle$ ($\alpha = e, \mu, \tau$) are not identical to their mass eigenstates $|\nu_i\rangle$ ($i = 1, 2, 3$), and those sets are interconnected by the unitary PMNS matrix analogous to the CKM matrix for quarks:

$$\begin{pmatrix} \nu_e \\ \nu_\mu \\ \nu_\tau \end{pmatrix} = U_{\text{PMNS}} \begin{pmatrix} \nu_1 \\ \nu_2 \\ \nu_3 \end{pmatrix}, \tag{1.13}$$

$$U_{\text{PMNS}} = \begin{bmatrix} C_1 & S_1C_3 & S_1S_3 \\ -S_1C_2 & K_1 & K_2 \\ S_1S_2 & K_3 & K_4 \end{bmatrix}, \tag{1.14}$$

where $S_i = \sin\theta_i$, $C_i = \cos\theta_i$, $K_1 = C_1C_2C_3 - S_1S_3e^{i\phi}$, $K_2 = C_1C_2C_3 - S_2C_3e^{i\phi}$, $K_3 = -C_1S_2C_3 - S_2S_3e^{i\phi}$, $K_4 = -C_1S_2C_3 + C_2C_3e^{i\phi}$ ($i = 1, 2, 3$).

This matrix contains four parameters: three mixing angles θ_1, θ_2, θ_3 ($0 < \theta_i < \frac{\pi}{2}$) and the complex phase ϕ ($-\pi < \phi < \pi$). If the mixing angles are zero, the mixing does not happen; when $\phi \neq 0$ CP-parity is violated similarly as it is observed in quarks.

In a weak interaction reaction, a neutrino flavor state is born as a superposition of mass eigenstates

$$|\nu_\alpha\rangle = \sum_i U_{\alpha i}|\nu_i\rangle. \tag{1.15}$$

During propagation the mass eigenstates $|\nu_i\rangle$ with different masses m_i will experience a different

[2] To date, there are no accurate experimental data indicating oscillations of charged leptons. However, the possibility of an experimental search for such oscillations was considered by Widom and Srivastava [WS97].

time evolution

$$|\nu_i(t)\rangle = e^{-iE_i t}|\nu_i\rangle, \tag{1.16}$$

where

$$E_i = \sqrt{p_i^2 + m_i^2} \approx p + \frac{m_i^2}{2p} \approx E + \frac{m_i^2}{2E}, \ (\hbar = c = 1) \text{ for } p \gg m_i, \tag{1.17}$$

which will result in a transformation of the flavor eigenstate from α into β with a probability of

$$P(\alpha \to \beta, t) = |\sum_i U_{\beta i} e^{-iE_i t} U^*_{\alpha i}|^2. \tag{1.18}$$

For a simplified case involving only two neutrino flavors, ν_e and ν_μ, and mass eigenstates, ν_1 and ν_2, this results (taking into account eq. (1.17)) for the case of ultra-relativistic neutrinos in:

$$P(\alpha \to \beta, t) = \sin^2(2\theta) \sin^2 \frac{(E_2 - E_1)t}{2}. \tag{1.19}$$

Therefore, the neutrino oscillation probability depends on three parameters:

- the mixing angle θ;
- the magnitude of the squared mass difference Δm^2

$$(E_2 - E_1) = \frac{m_2^2 - m_1^2}{2p} := \frac{\Delta m^2}{2p}; \tag{1.20}$$

- the time passed since a neutrino of a certain type was born, or the distance traveled if we rewrite

$$\frac{(E_2 - E_1)t}{2} = \frac{\Delta m^2 L}{4E_\nu}, \tag{1.21}$$

  where E_ν is the energy of the neutrino.

The theoretical expectation for the flavor composition of neutrinos from a reactor as a function distance (according to eq. (1.18)) is represented in fig. 1.1.

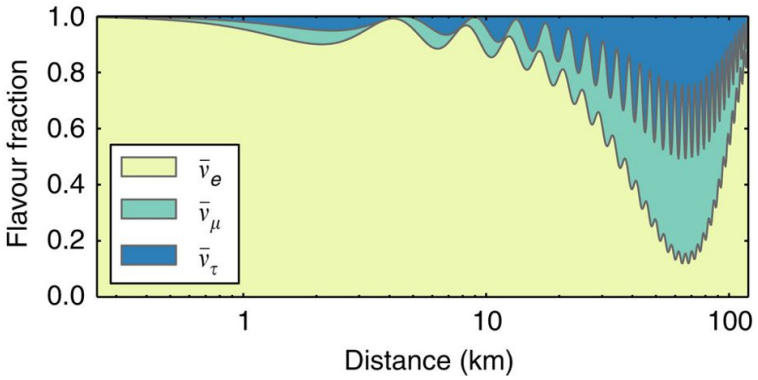

Figure 1.1: Theoretical neutrino flux flavor composition of a reactor beam assuming pure $\bar{\nu}_e$ at the start depending on distance. From [VWZ].

This consideration is valid for neutrinos traveling in vacuum; in matter, the oscillation process is more complicated due to elastic coherent forward scattering and is described by the Mikheew-Smirnow-Wolfenstein effect (or MSW-effect).

Mixing angles		Mass splitting	
$\sin^2(\theta_{12})$	$0.307^{+0.013}_{-0.012}$	Δm^2_{21}	$7.53(18) \cdot 10^{-5}$ eV^2
$\sin^2(\theta_{23})$	$0.536^{+0.023}_{-0.028}$ [NH] $0.512^{+0.019}_{-0.022}$ octant I, $0.542^{+0.019}_{-0.022}$ octant II [IH]	$\lvert\Delta m^2_{23}\rvert$	$2.444(34) \cdot 10^{-3}$ eV^2 [NH] $-2.55(4) \cdot 10^{-3}$ eV^2 [IH]
$\sin^2(\theta_{13})$	$2.18(7) \cdot 10^{-2}$	Δm^2_{13}	$\approx \lvert\Delta m^2_{23}\rvert$

Table 1.1: Current status of the measured oscillation parameters. Since the sign of Δm^2_{23} is still unknown, the cases of normal and inverted mass hierarchies (NH and IH) are distinguished [Tan+18].

In the experiments searching for neutrino oscillations, θ and Δm^2 parameters are measured. The experiments are, however, unable to determine the absolute neutrino masses. The ways to approach this parameter is discussed in the next section.

The first experimental hint to existence of neutrino oscillations was obtained by Raymond Davis' Homestake experiment for the registration of solar ν_e which used the idea of Bruno Pontecorvo to use the reaction of the conversion of chlorine into a radioactive isotope of argon under the influence of a neutrino (inverse β-decay)

$$\nu_e + {}^{37}\mathrm{Cl} \rightarrow {}^{37}\mathrm{Ar} + e^-. \tag{1.22}$$

The detected ν_e rate appeared to be about tree times less [Cle+98] than the one theoretically calculated by John Bahcall [BU88]. Since neither the experimental method nor the calculations revealed an error (the Sun model appeared to be too rigid to allow such a deviation) this lack of observed rate was called "the solar neutrino problem". The two gallium-germanium experiments, SAGE and GALLEX/GNO, which came afterwards, confirmed the lack of electron neutrinos.

The next step to give a conclusion on the problem was the SNO (Sudbury Neutrino Observatory) experiment. The radiochemical methods used by the Homestake and the gallium-germanium experiments, are only sensitive to electron neutrinos. The SNO experiment is sensitive to all three flavors. It has been observed that the total neutrino flux from the Sun is in the agreement with the standard Sun model and the electron neutrino flux is about 1/3 of the flux predicted by it. Therefore, the experiment proved that the deficiency of the ν_e from the sun observed in the radiochemical experiments comes from the phenomenon of neutrino oscillations [Ahm+02], [Ahm+04]. This experiment, however, does not measure neutrino mixing in vacuum since the MSW-effect takes place in the Sun. Neutrino oscillations in vacuum were discovered even earlier by the Super-Kamiokande experiment by observing atmospheric ν_μ [Fuk+98]. The results were confirmed in reactor and accelerator experiments. For example, measured oscillation parameters in the KamLAND reactor experiment are in good agreement with parameters obtained in the solar neutrino experiments and the ones measured in the accelerator experiments K2K, T2K, MINOS, NOvA and Opera and are coinciding with the Super-Kamiokande results.

The reactor experiments Double Chooz, Daya Bay and Reno helped to complete the oscillation parameters by measuring θ_{13}. In these experiments, oscillation physics transfers from the stage of discoveries to the stage of precision measurements. In table 1.1 current measurement results of the oscillation parameters are presented. Meanwhile, the questions of mass hierarchy, CP-violating phase and Majorana or Dirac nature of the neutrinos still remain open.

There are many different extensions of the Standard Model allowing to generate neutrino masses. Not all of them, however, allow to explain their extreme smallness compared to the masses of other

fermions. The most straightforward way to overcome this issue is a postulation of the existence of right-handed neutrinos and left-handed antineutrinos which results in the appearance of Dirac mass terms in the Lagrangian but poses the problem of coupling constants which have to be extremely small to generate the tiny neutrino masses.

Another way could be an assumption that neutrinos are Majorana particles (*i.e.* are their own antiparticles) which is not prohibited by any quantum number conservation law. Then the Lagrangian gets Majorana mass terms which include a mass matrix

$$M = \begin{bmatrix} m_L^M & m^D \\ m^D & m_R^M \end{bmatrix}, \tag{1.23}$$

where m^D, m_L^M, m_R^M are coupling parameters (Dirac and Majorana masses). The physical mass of the neutrino is the eigenvalue of M after a unitary transformation with eigenvalues

$$m_{1,2} = \frac{m_L^M + m_R^M}{2} \pm \sqrt{\frac{(m_L^M - m_R^M)^2}{4} + m_D^2}. \tag{1.24}$$

There are three cases of interest:

- $m_L^M = m_R^M = 0$: there is only the Dirac neutrino with $m = m_1 = m_2 = m^D$ consisting of two Majorana states with degenerated masses;
- $m^D \gg m_L^M = m_R^M = \varepsilon$: there are two Majorana states with quasi-degenerated masses $m_{1,2} = m^D \pm \varepsilon$ and opposite CP-violating phases. They form a Dirac neutrino with a small L-violating admixture. This is so called pseudo-Dirac neutrino;
- $m_L^M = 0$, $m_R^M \gg m^D$: in this case a heavy

$$m_1 = m_R^M \left[1 + \left(\frac{m^D}{m_R^M}\right)^2\right] \approx m_R^M \tag{1.25}$$

and a light

$$m_2 = \frac{(m^D)^2}{m_R^M} \ll m^D \tag{1.26}$$

mass eigenstate comes out. This is the so called *see-saw mechanism type I*: the big Dirac mass is very much suppressed because of even bigger Majorana mass. This gives a natural explanation of the neutrino mass smallness due to the presence of a second very heavy neutrino. Moreover, the assumption $m_L^M = 0$ is natural, since a Majorana mass term for the left-handed chiral field ν_L is forbidden by the symmetries and renormalizability of the Standard Model.

There is also a *see-saw mechanism type II* where neutrino masses are provided by introducing an additional Higgs-triplet Δ which is present in some extensions of the Standard Model. In this model, degenerated neutrino masses ($m_1 \approx m_2 \approx m_3$) are favored.

An accurate neutrino mass measurement would allow therefore to distinguish and rule out some of the theoretical models, as well as to answer the neutrino mass hierarchy question. Different ways to measure neutrino masses is discussed in the next subsection.

1.4 Methods to experimentally determine neutrino mass

In this section, the main ideas, as well as advantages and disadvantages of different ways of neutrino mass determination is explained ending up with the kinematic measurements from β-decay used in the KATRIN experiment.

1.4.1 From cosmological observations

Being present in the Universe throughout its history, massive neutrinos affect structure formation by interacting with matter fields at different stages of its evolution. Relativistic neutrinos having tiny but non-zero masses and interacting gravitationally are smearing out small-scale structures in the early Universe on a scale of their free-streaming (which is connected to the sum of the three neutrino masses $M_\nu = \sum_i m_i$) thus called *hot dark matter*. In the process of expansion and cooling of the Universe the thermal equilibrium between neutrinos and the other particles broke and neutrinos decoupled ($\sim$1 s after the Big Bang). The decoupling resulted in small density fluctuations which turned later into the structure of the Universe observed nowadays. Since photons decoupled from the rest of the matter later than neutrinos the properties of neutrinos (such as their masses) are imprinted into the temperature spectrum and anisotropy of the cosmic microwave background (CMB).

The CMB properties are probed by observatories such as Planck or WMAP [Pla+14], [BM14], [PD+15]. Their data are compared to theoretical cosmological models which yield constrains on the M_ν as one of their parameters (which makes the constrains therefore model-dependent) [LP06]. The present limit on the combined analysis is [Agh+18]

$$M_\nu < 0.12 \text{ eV (68\% C.L.)[Planck]}. \tag{1.27}$$

Apart from the CMB, M_ν also influences power spectrum of matter distribution in the Universe. In [Lou+19], the neutrino mass estimation has been further precised to be

$$M_\nu < 0.26 \text{ eV (95\% C.L.)} \tag{1.28}$$

by combining data from the large scale structure of galaxies, CMB, type I supernovae, measurements of Big Bang deuterium-hydrogen fraction and constrains for mass splittings from oscillation experiments.

1.4.2 From neutrinoless double beta decay

Another way to determine neutrino masses would be the measurement of neutrinoless double beta ($0\nu\beta\beta$) decay. This is a hypothetical not yet discovered process of a double beta decay without production of neutrinos in the final state

$$A(Z, N) \rightarrow A(Z + 2, N - 2) + 2e^-. \tag{1.29}$$

In this case an antineutrino produced in the decay of one of the neutrons of the (A, Z) nucleus interacts as a neutrino with the another neutron of the formed $(A, Z+1)$ nucleus

$$n \rightarrow p + e^- + \bar{\nu}_e, \tag{1.30}$$

$$n + \nu_e \rightarrow p + e^-. \tag{1.31}$$

As a consequence, the charge of the nucleus is increased by 2 and 2 electrons are created which carry all the kinetic energy. The latter manifest themselves as a sharp peak at the end of the decay spectrum.

Such a decay is possible if the neutrino ν_e is identical to its antiparticle $\bar{\nu}_e$:

$$\nu_e \equiv \bar{\nu}_e. \tag{1.32}$$

This implies a violation of lepton number conservation and, moreover, because of the lefthandedness of weak charge currents the decay can only take place under the condition of a helicity change in the neutrino. This, in turn, directly implies that neutrinos have a non-zero mass. Therefore, $0\nu\beta\beta$-decay is a sensitive probe of the neutrino mass and nature (Dirac or Majorana).

If it were possible to determine experimentally how often the decay occurs, it would allow to deduce an effective neutrino mass since the decay rate is proportional to the square of the coherent sum of the three neutrino mass eigenstates:

$$\Gamma \propto |\sum_i U_{ei}^2 m_i|^2 \equiv m_{\beta\beta}^2. \tag{1.33}$$

The mass term is the coherent sum over the three neutrino mass eigenstates, but holds the possibility for contributions to be cancelled partially due to the phase factors of the PMNS matrix. Up to now, neutrinoless double beta decays have not been registered, it has only been possible to constrain the Majorana mass of neutrinos. Reliability and accuracy of those limits are to a large extent determined by the quality of nuclear matrix element (NME) calculation which makes this method model-dependent as well. Nonetheless, it is possible to obtain upper limits by using the most conservative estimations of the NME.

The number of candidates for the observation of double beta decay is quite large: 35 nuclei. However, because the probability of the decay is strongly dependent on the transition energy, the most interesting are the ones with transition energies $E_{2\beta} > 2\,\mathrm{MeV}$. The GERDA experiment using enriched-^{76}Ge detectors provided a the limit of [Ago+18]

$$\langle m_{\beta\beta} \rangle < 0.12 - 0.26 \text{ eV}, \tag{1.34}$$

while the EXO-200 experiment based on enriched ^{136}Xe constrained the mass to [Alb+18]

$$\langle m_{\beta\beta} \rangle < 0.15 - 0.40 \text{ eV}. \tag{1.35}$$

There has been a claim in 2006 from the Heidelberg-Moscow group using a germanium-based detector about an observation of a $0\nu\beta\beta$-decay with a corresponding neutrino mass of 0.3 eV

[KKK06] which, however, has been disproved later by other experiments [MAC14].

1.4.3 From supernova explosions

The time-of-flight difference between neutrinos and photons from supernova explosions can be used to determine the average mass of the electron neutrino due to the fact that massive neutrinos travel somewhat slower than light. The observable in this case is an incoherent sum over the mass eigenstates

$$m_{\nu_e} = \sqrt{\sum_i |U_{ei}|^2 m_i^2}. \tag{1.36}$$

not subject to cancellations as in eq. (1.33) For example, it was possible to obtain a limit from an observation of 24 neutrino events with energies between 10 MeV and 40 MeV from the SN1987A supernova (which happened in the Large Magellan Cloud $\sim 168 \cdot 10^3$ly from us) detected within 13 s by the Kamiokande, IMB, LSD and Baksan detectors [Bar+09].

If neutrinos have a non-zero mass m_ν and the supernova emits two neutrinos of energies E_1 and E_2 at the same time, the signals will arrive at the detector in a distance L from the supernova with the time difference equal to their time-of-flight difference:

$$\Delta t_{tof} = \frac{L}{2c}(m_\nu c^2)^2 \left(\frac{1}{E_1^2} - \frac{1}{E_2^2}\right). \tag{1.37}$$

In reality supernovae do not emit all neutrinos at the same time. The emission time cannot be known exactly and therefore does not allow to precisely deduce neutrino masses from expression (1.37). However, the full duration of neutrino emission ΔT can be derived from modeling of the supernova event which gives a possibility to estimate a model-dependent neutrino mass constraint from difference in measured arrival times

$$\Delta t_{arrival} \leq \Delta t_{tof} + \Delta T \tag{1.38}$$

The current upper limit from such an estimation for the SN1987A is [Tan+18]

$$m_{\nu_e} < 5.8 \text{ eV (95\% C.L.)}. \tag{1.39}$$

1.4.4 From direct kinematic measurements

For cases of zero and non-zero neutrino mass, the energy spectrum of electrons observed in the process of radioactive beta decay will be different near its endpoint $E_0 = Q - E_{rec} - m_{\nu_e}c^2$ (where Q is the total decay energy, E_{rec} is the recoil energy of the nucleus and m_{ν_e} is the neutrino mass). Relying only on energy-momentum conservation (thus not depending on any model) and investigating the endpoint region of the β-spectrum, one can determine the "average electron neutrino mass squared"

$$m_{\nu_e}^2 = \sum_i |U_{ei}|^2 m_i^2. \tag{1.40}$$

if the individual neutrino masses m_i cannot be resolved.

According to Fermi's golden rule, the electron kinetic energy spectrum in the decay $(A, Z) \rightarrow$

$(A, Z+1) + e^- + \bar{\nu}_e$ in the energy interval $[E, E+dE]$ can be calculated as

$$\frac{dN^2}{dtdE} = \frac{d\dot{N}}{dE} = \frac{2\pi}{\hbar}|M|^2\rho(E), \tag{1.41}$$

where $\rho(E)$ is the phase-space density and M is the NME.

Neglecting the nuclear recoil energy, one can obtain the following expression for the β-spectrum as [ee03]:

$$\frac{d\dot{N}}{dE} = \frac{G_F^2}{\pi^3\hbar^7c^5}\cos^2\theta_C|M|^2F(Z+1,E)p(E+m_ec^2)(E_0-E)p_{\nu_e}\Theta(E_0-E-m_{\nu_e}c^2), \tag{1.42}$$

where G_F is the Fermi coupling constant, θ_C is Cabbibo angle, m_e, p and E are mass, absolute value of the momentum and kinetic energy of the electron correspondingly, $F(Z+1,E)$ is the Fermi function describing the Coulomb interaction of the final particles, $\Theta(E_0-E-m_{\nu_e}c^2)$ is the Heaviside step function taking into account that the neutrino state ν_e is only born if the total energy is greater then the mass of the neutrino: $E_{\nu_e} = E_0 - E \geqslant m_{\nu_e}$ and $p_{\nu_e} = \sqrt{E_{\nu_e}^2 - m_{\nu_e}^2c^4} = \sqrt{(E_0-E)^2 - m_{\nu_e}^2c^4}$ is the neutrino momentum. The latter is the term by which the neutrino mass affects the spectrum. The recoil energy to the nucleus is neglected in this equation. As can be seen, indeed, the largest distortion of the β-spectrum due to the neutrino mass could be observed in the region

$$E_0 - E \sim m_{\nu_e}c^2. \tag{1.43}$$

However, the statistics there is scarce and the endpoint energy E_0 is not known precisely enough, therefore, a larger region of the spectrum is used for experimental analysis, see fig. 1.2. Sources with a low endpoint energy improve the experimental sensitivity and resolution since for them a greater fraction of electrons are located near the endpoint.

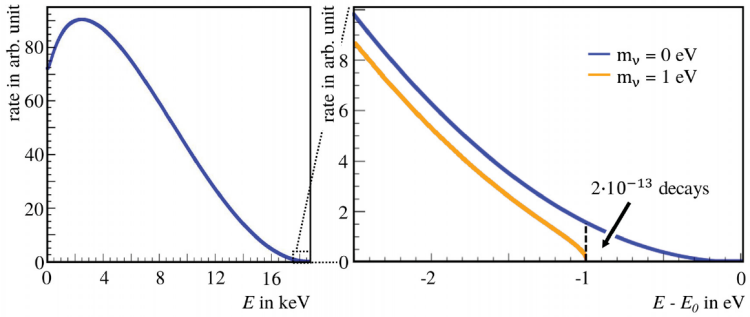

Figure 1.2: Differential β-spectrum of tritium. On the right plot a zoomed endpoint region is presented showing the influence of the neutrino mass on the spectral shape. Due to poor statistics in this region, a luminous source and high-resolution spectrometer is needed to be able to resolve this effect. From [Dyb18] (adapted from [Val09]).

A suitable candidate for this method is the hydrogen isotope ^{3}H (tritium). It has decay energy Q =18.6 keV, the half life $T_{1/2}$ =12.3 years and a superallowed type of β-transition $1/2^+ \to 1/2^+$

$$^3\mathrm{H} \to {}^3\mathrm{He}^+ + e^- + \bar{\nu}_e, \tag{1.44}$$

that makes the NME energy-independent.

Tritium-based experiments usually have an external source providing a large luminosity and use the MAC-E filter technique to achieve a large angular acceptance and the required energy resolution. The two former experiments at Mainz [Kra+05] and Troitsk [Ase+11] provided upper limits of

$$m_{\nu_e} < 2.3 \text{ eV (95\% C.L.) (Mainz)} \tag{1.45}$$

$$m_{\nu_e} < 2.05 \text{ eV (95\% C.L.) (Troitsk)}, \tag{1.46}$$

(due to the CPT-theorem there is no differentiation between m_{ν_e} and $m_{\bar{\nu}_e}$).At the present time, their successor, the KATRIN experiment, is taking data to improve this limit. It aims to push the sensitivity down to $0.2\,\mathrm{eV/c^2}$ at 90% C.L. after 5 years of operation. It has already recently improved the mass limits of its predecessors by almost a factor of two [Ake+19a]

$$m_{\nu_e} < 1.1 \text{ eV (90\% C.L.)} \tag{1.47}$$

using a four-week measurement.

An alternative to the previously mentioned β^--decay is so called electron capture. In this sector, the main candidate is ^{163}Ho with Q =2.8 keV and $T_{1/2}$ =4570 years. In this transformation a nucleus is capturing one of the electrons of its atomic shell followed by the emission of an electron neutrino

$$^{163}\mathrm{Ho} + e^- \rightarrow {}^{163}\mathrm{Dy}^* + \nu_e. \tag{1.48}$$

In this case as well, the mass of the neutrino influences the spectral shape near the endpoint of the electromagnetic deexcitation of the excited atom ^{163}Dy.

At the present day, there are three projects studying the calorimetric spectrum of the ^{163}Ho decay: ECHo [Gas+17] and HOLMES [Alp+15], which although studying the same process have fundamental differences in their technical realization.

As has been shown in the previous sections, there are many interconnections between particle physics, neutrino physics and astrophysics, the number of which continues to increase with time. The properties of particles and fields determine the evolution of the Universe in the past, its current state and its future fate. Therefore, experiments and observations in these areas are crucial for each other.

One of such front-rank experiments is the KATRIN experiment which in its first measurement campaign has delivered the most precise constraint on the electron neutrino mass to date. In the next chapter, a general overview of the KATRIN experiment is presented.

1.5 Thesis outline

This thesis is organized as follows:

Chapter 2 will explain the KATRIN set-up and its main subsystems, with a specific focus on the MAC-E filtering technique realized in its spectrometers. Furthermore, the statistical and systematic uncertainties of the experiment and their effect on the neutrino mass sensitivity is described.

Chapter 3 will introduce the KATRIN condensed krypton conversion electron source (CKrS) utilizing ^{83m}Kr, quench-condensed onto an HOPG substrate. After explanation of its components and the working principle, a special discussion is given to ellipsometry investigations of the krypton films prepared during measurement campaigns in 2017 and 2018.

Chapter 4 is devoted to a different topic: the problem of the inter-spectrometer Penning trap which is formed by the combination of the two KATRIN MAC-E filters (pre- and main spectrometers). A description of the physical processes leading to accumulation of electrons, which increase the detector background and can build up harmful discharges, is followed by a presentation of a countermeasure, the so called "electron catchers" which were designed and installed in the magnet bore between the spectrometers to remove trapped particles. Experimental investigations of the Penning trap behavior and the electron catcher performance with different pressure and electromagnetic field conditions are discussed and wrapped up by a presentation of the system behavior at nominal spectrometer settings.

In **Chapter 5** the conclusions of this work is given.

Chapter 2

The KATRIN experiment

The KArlsruhe TRItium Neutrino experiment (KATRIN) aims to determine the (anti)neutrino mass (or at least to lower its current experimental limit) with a sensitivity of $0.2\,\mathrm{eV/c^2}$ (90% C.L.) from energy measurements of tritium β-decay electrons exploiting the similar techniques as its forerunners in Mainz and Troitsk. The KATRIN experiment is based at the Karlsruhe Institute of Technology (KIT) due to its unique tritium handling facility, the Tritium Laboratory Karlsruhe (TLK).

The experimental set-up consists of a luminous windowless gaseous tritium source (WGTS) which provides a high rate of β-electrons, a transport section through which the electron beam is guided towards the energy analysis systems and where tritium molecules are removed, and the spectrometer and detector section (SDS), where the spectral information is extracted, see fig. 2.1.

In the following, an overview of the complex KATRIN set-up is given.

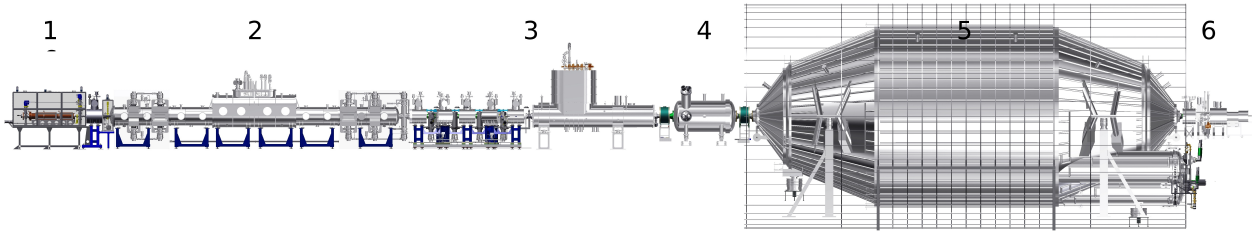

Figure 2.1: The KATRIN experimental set-up. The main components are: (1) calibration and monitoring rear section, (2) windowless gaseous tritium source, (3) transport section, (4) pre-spectrometer, (5) main spectrometer, and (6) focal plane detector.

2.1 Rear section

At the most upstream end of the beamline the rear section (see fig. 2.2) is located. It serves for control and diagnostics of various important parameters of the whole experiment. It includes, for example, an angular-selective electron gun (e-gun) to measure the overall beamline response function, which contains information about the transmission function and inelastic scattering of electrons in the tritium source, and a rear detector to monitor the source activity. The rear section also houses the gold-plated rear wall which is placed between the rear section and the WGTS and controls the plasma potential of the source. Charged particles moving towards the rear section are

magnetically guided onto the rear wall, where they are neutralized. Additionally, using illumination to eject electrons via a photoelectric effect the charging-up of the tritium gas can be prevented. [KK05], [Bab14], [Han+17].

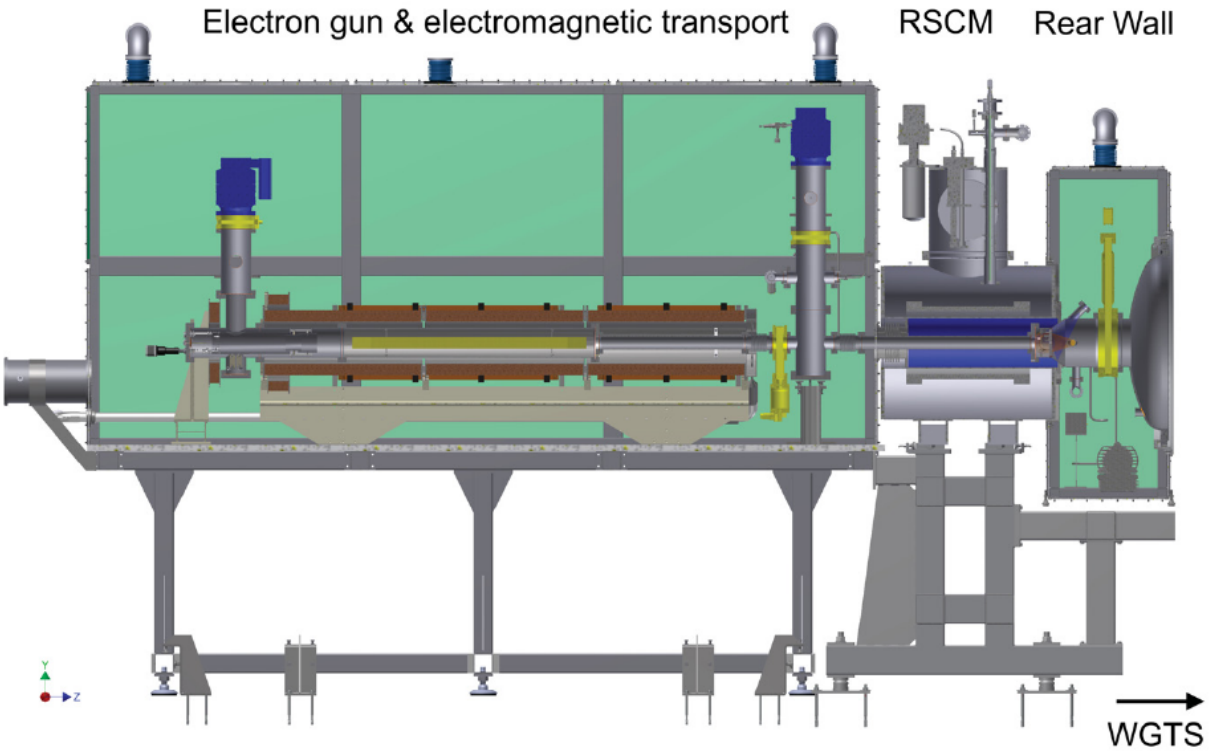

Figure 2.2: A schematic view of the KATRIN rear section. A containment for the e-gun can be seen on the left and the rear wall chamber at the exit to the WGTS is on the right side. [Bab14]

2.2 Source and Transport section

The source and transport section (STS) includes the Windowless Gaseous Tritium Source (WGTS) and the transport section divided into two pumping sections: the differential pumping section (DPS) and the cryogenic pumping section (CPS). All tritium-related parts are enclosed within the TLK safety barriers.

The core component is the windowless gaseous tritium source shown in fig. 2.3 which has a 10 m long beam tube with a diameter of 90 mm. There, the T_2 gas is injected at a pressure of P_{inj} =3.4 $\times$ 10^{-3} mbar (or 5 $\times$ 10^{19} molecules/s) for an optimum column density of ρd =5 $\times$ 10^{17} cm^{-2} (the yearly throughput is about 10 kg) and is kept at 30 K by a two-phase neon cooling system. This allows to achieve the design activity of 10^{11} Bq. The column density must be known to 0.1% accuracy to ensure the sensitivity goal [KK05], which requires the stability of the injection pressure and temperature to be $\lesssim 10^{-6}$ mbar and $\lesssim$30 mK respectively. The tritium gas is processed in a closed loop system to maintain its isotopic purity of $> 95\%$ (which is monitored by a laser Raman spectroscopy system (LARA) [Bab14]): the gas is injected at the center of the WGTS tube and is pumped out at both ends by the DPS1-R and DPS1-F pumping sections. To guide electrons from the β-decays from the source towards the spectrometer, the WGTS is surrounded by superconducting

solenoid magnets creating a field of 3.6 T.

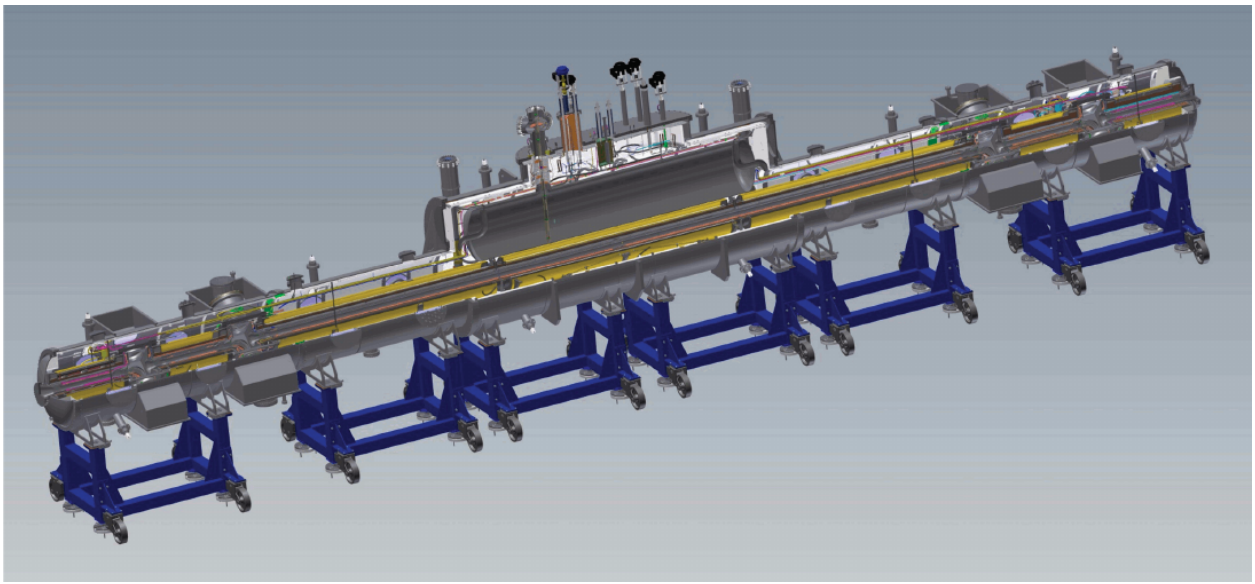

Figure 2.3: The Windowless Gaseous Tritium Source (WGTS). The 10 m beam tube is surrounded by superconducting magnets with the differential pumping sections DPS1-R and F at both ends inside a common cryostat.

The background generated by tritium decays within the spectrometers must be less than 10^{-3} counts/s which limits the permissible flow of tritium into the spectrometer section to $<10^{-14}\,\frac{\text{mbar}}{\text{l}}$ while the flow directly after the WGTS amounts to about 2 mbar·l/s. To achieve this, two pumping sections, differential (DPS-2) and cryogenic (CPS), providing a suppression factor of about 10^7 each, follow the DPS-1 at the end of WGTS [Luo+06a], [Gil+12].

The DPS-2 is a series of five one-meter-long segments (see fig. 2.4) each of which is placed at 20 ° wrt. the neighboring segments. This construction feature serves for retention of the neutral particles which go straight into the beamline bends. The latter are surrounded by superconducting coils which generate the guiding magnetic field for electrons and are instrumented in-between with turbo-molecular pumps (TMPs) that reach a final pressure of 6×10^{-10} mbar to match the ultra-high vacuum conditions of the spectrometer section [Luo+06b], [Luk+12], [Kos12]. Since positive ions also follow the magnetic field lines to some extent, at the last segment downstream of the DPS-2 there are dipole electrodes which introduce $E \times B$ drift fields to deflect ions towards the walls [Rei09], [Hac17].

Between the DPS-2 and the SDS, the CPS is situated. It has essentially the same design as the DPS-2 as is shown in fig. 2.5, but the beam tube here is kept at 3 K. At this temperature, tritium molecules are passively absorbed onto the cold inner tube surfaces which are additionally covered by a thin layer of argon frost to enhance the trapping probability (see fig. 2.5). The argon layer will be replaced every two months to remove the accumulated activity [Gil+10]. A schematic drawing of the CPS is given in fig. 2.5. As can be seen, the CPS beam tube is subdivided into seven segments where the first five have a mutual arrangement similarly to those of the DPS-2 to suppress the flow of the neutral molecules into the SDS. This first five segments are separated from the last two by the cold gate valve V3 [Gil+10]. Between the sixths and the sevenths segments, two ports are placed perpendicularly to each other: a horizontal one, allowing to move the forward beam monitor

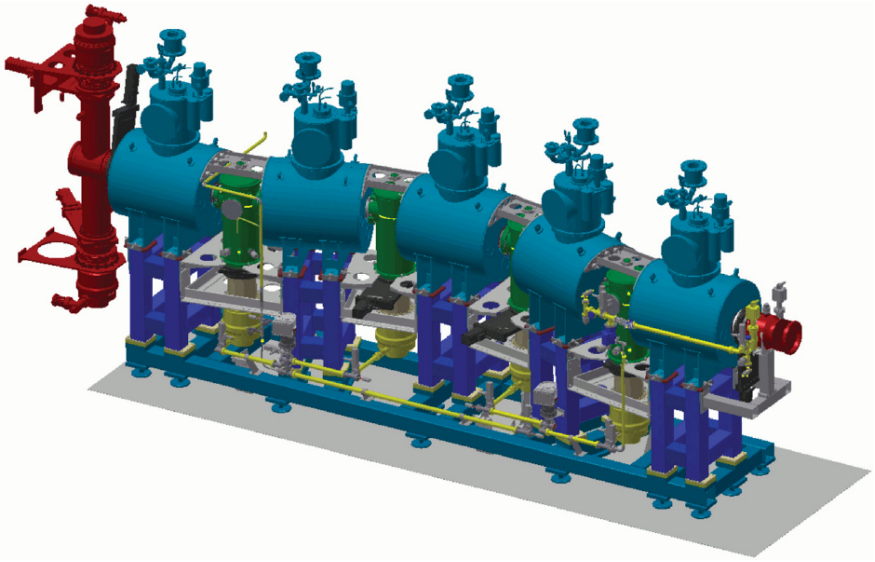

Figure 2.4: Side view of the DPS-2 with its five magnets. The bent structure and TMPs at the interconnections of the segments reduce the flow of ions and tritium molecules into the SDS system while the electrons follow the magnetic guiding fields.

(FBM) into the flux tube to measure the source activity during tritium runs, and a vertical one for the Condensed Krypton Source (CKrS) sitting on the top of the CPS to enter the beamline for calibration operations. The CKrS is discussed in details in chapter 3.

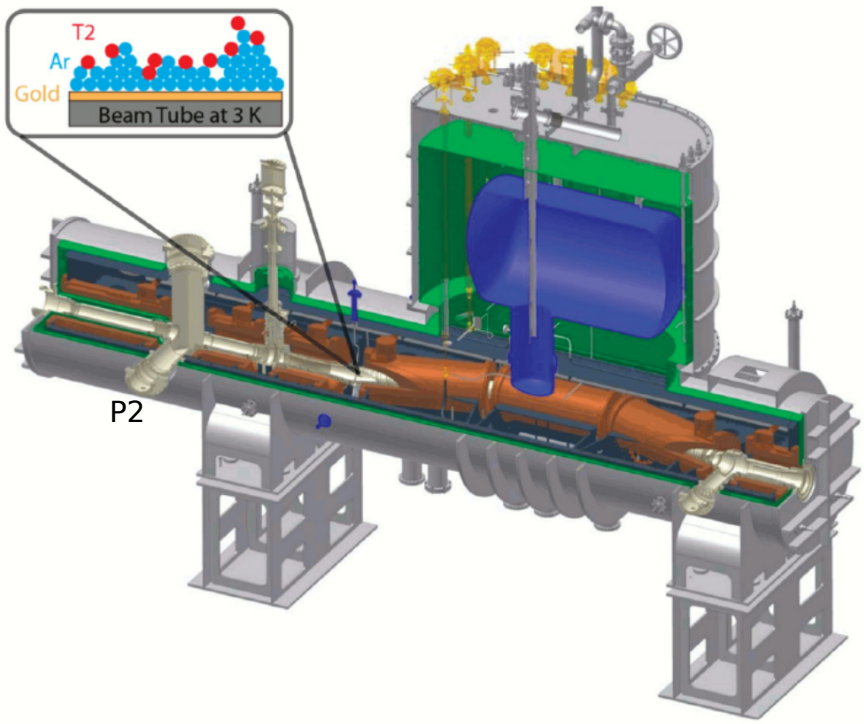

Figure 2.5: A CAD drawing of the CPS. It has the similar bent chain structure as the DPS-2 while its beam tube is cooled down to 3 K and is covered by argon frost to retain residual tritium molecules and decay products. The two ports orthogonal to the beamline (P2) allow to insert the FBM and the CKrS into the flux tube for activity and calibration measurements. Adapted from [Wan13].

2.3 Spectrometer and detector section

Directly after the CPS, the pre-spectrometer (PS) with the successive main spectrometer (MS) are placed in the main beamline (fig. 2.6) and both working in MAC-E filtering mode (an explanation of this technique is given in the next section) but serving different purposes which is described below. Parallel to the main spectrometer, in a separate "monitor beamline", a third MAC-E-type spectrometer, called the monitor spectrometer (MoS), is installed (fig. 2.7). It is a spectrometer from the former Mainz neutrino mass experiment which has been refurbished for KATRIN to monitor the retarding potential stability by measuring the position of spectral lines provided by krypton source, implanted into an HOPG (highly-oriented pyrolytic graphite) substrate and providing a natural energy standard [Erh+14], [Sle15], [Erh16].

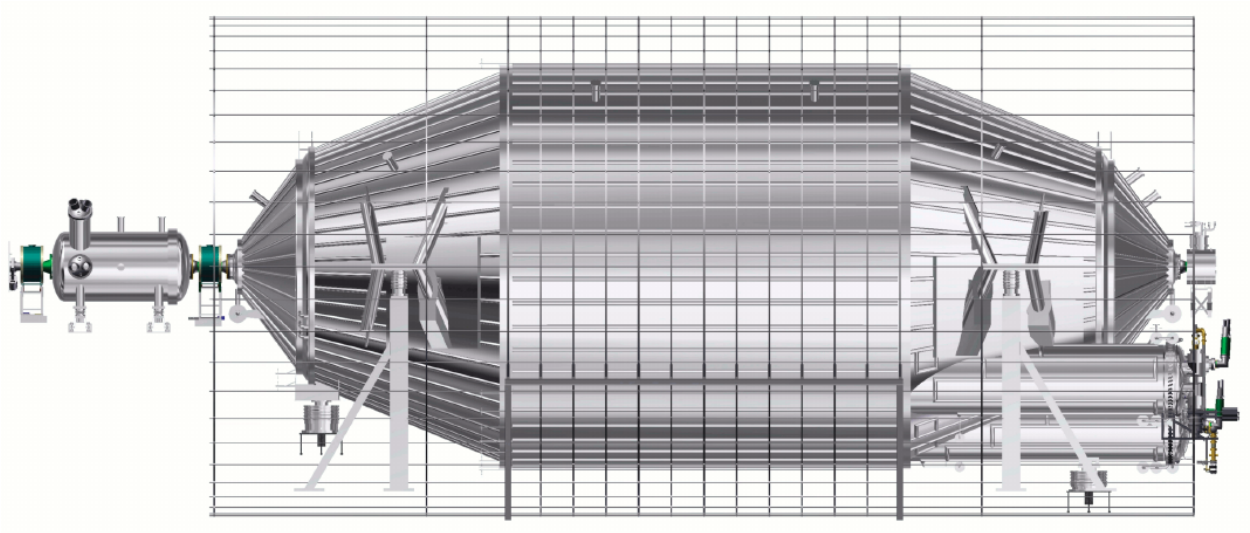

Figure 2.6: The tandem of the pre- and main spectrometers (MAC-E filters). The pre-spectrometer operates at −18.3 kV to reject low-energy electrons useless for the neutrino mass analysis but able to create additional background in the main spectrometer. The voltage of the main spectrometer is varied around −18.6 kV to measure the integrated beta spectrum in the endpoint region most sensitive to the neutrino mass.

The pre-spectrometer is a 3.4 m long stainless steel vessel with 1.7 m diameter in which a magnetic guiding field is created by 4.5 T with superconducting magnets. It is set on −18.3 kV retarding potential to pre-filter the electron flow so only the electrons with energies in the 300 eV-region below the tritium endpoint are able to get into the main spectrometer. The pre-spectrometer is additionally equipped with an inner electrode system to reduce the muon background.

The main spectrometer has larger vessel dimensions: 23.3 m length and a diameter of 10 m sufficient for the required energy analysis precision. It provides a resolution of 0.93 eV for electron energies around 18.6 keV needed to achieve the sensitivity goal of KATRIN. Its retarding potential is varied around −18.6 kV to scan the endpoint region [Val09], [Zac15], [Pic+92b]. To tune the electric field inside the vessel, it is equipped by a system of inner wire electrodes [Val09], [Zac09], [Pra11].

In order to reach the required energy measurement accuracy, the retarding potential has to be extremely stable and any remaining fluctuations have to be precisely measured. One method which

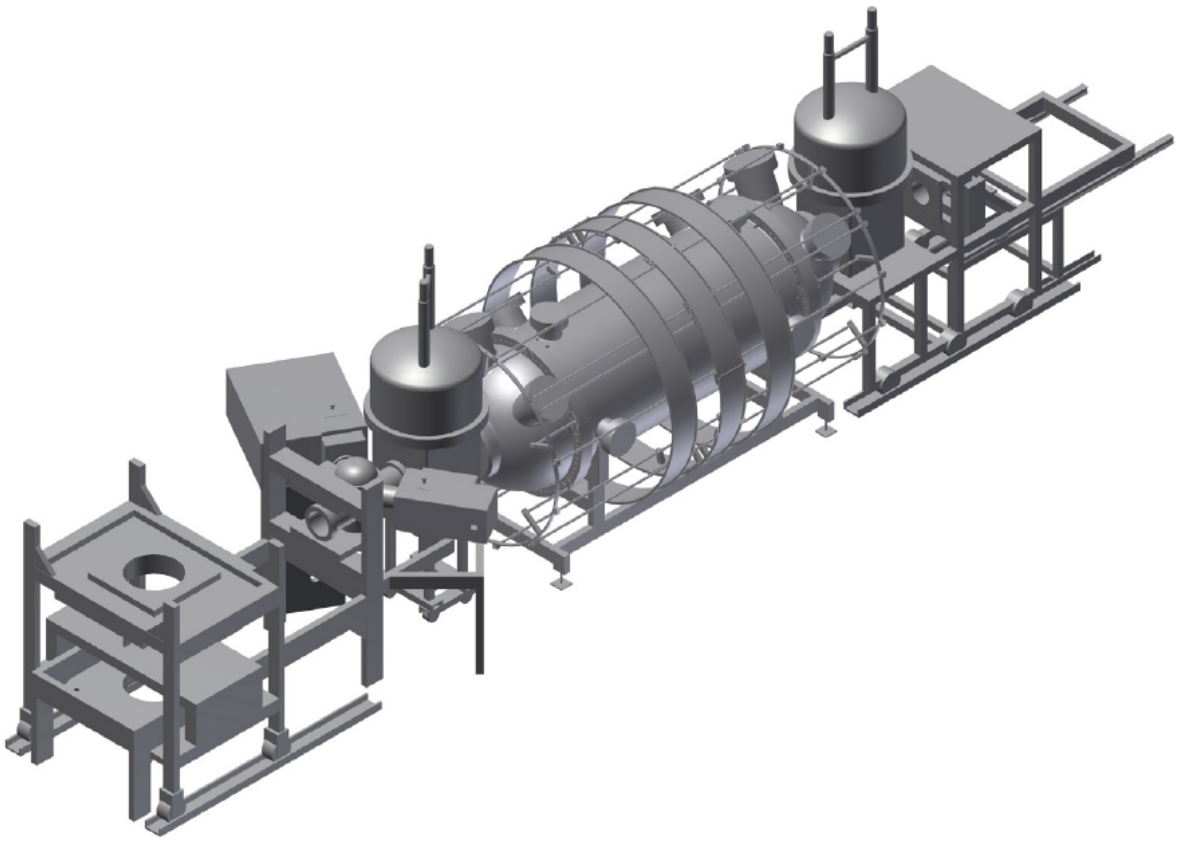

Figure 2.7: The KATRIN monitor spectrometer refurbished from the Mainz neutrino mass experiment also working in a MAC-E filter mode. Sharing the high voltage with the main spectrometer it is used to monitor its retarding potential stability by measuring ^{83m}Kr conversion electron lines.

is used in KATRIN for this purpose is the monitor spectrometer as has been mentioned above. Another method are specifically designed, ultra-precise high-voltage dividers developed together with the Physikalische Technische Bundesanstalt (PTB) at the university of Münster for the KATRIN experiment. These are directly connected to the spectrometer HV power supplies and scale down the voltage by a factor of ≈2000 [Bau14], [Thü07]. This makes it possible to measure the voltage with a commercial precision volt-meter in a 10 V range when operating the spectrometer in the kV regime. The divider itself has been calibrated using a reference divider at the PTB. In addition to that, a relative calibration against a precision 10 V source calibrated against a Josephson voltage standard at the PTB is used. Another novel method has been recently developed and described in [Res19] which allows for an absolute HV calibration on-site at the KIT.

The magnetic field inside the main spectrometer is produced by two superconducting solenoids at the ends of the vessel, one common with the pre-spectrometer and the other is a pinch magnet on the detector side creating up to 6 T field. The magnetic field is additionally shaped by a low-field correction system (LFCS) consisting of vertical air coils surrounding the vessel and by horizontal coils to compensate the Earth magnetic field (EMCS) [Gl13], [Erh+18].

The energy analysis principle of the spectrometer is explained in the next section.

For neutrino mass measurements, both spectrometers are kept at ultra-high vacuum (UHV) conditions with the main spectrometer reaching down to 10^{-11} mbar pressure. This is needed to minimize scattering of β-electrons with residual gas which would increase the experimental

background. To reach this pressure, a combination of turbo-molecular and getter pumps is used [Are+16], [Har15].

Despite the advantages given by usage of the subsequent pre- and main spectrometers, the combination of electric and magnetic fields realized in such a set-up leads to potential difficulties by creating a Penning trap in the inter-spectrometer region. A detailed discussion of the problem and its solution is given in chapter 4 of this thesis.

Electrons passing the main spectrometer are guided onto the focal plane detector (FPD) at the upstream end of the KATRIN set-up where they are counted. The FPD is a silicon-based PIN-diode array with 148 pixels arranged in a dart-board pattern which provides a spatial resolution of the flux tube, see fig. 2.8. It is housed on a monolithic silicon wafer of 9 cm sensitive diameter and 500 µm thickness. Although the energy analysis is performed by the main spectrometer, the FPD has its own energy resolution of 1.4 keV FWHM (full width at half maximum) which allows to perform energy cuts for background and electronic noise rejection. To reduce the intrinsic background of the detector, the wafer is surrounded by a passive shield of lead and copper and an active veto system based on plastic scintillators to remove signals from incident cosmic rays. Moreover, the detector wafer with a first stage of read-out electronics is operated in high-vacuum conditions ($\sim 10^{-6}$ mbar) and is cooled to $-30\,^{\circ}$C to reduce electronic noise.

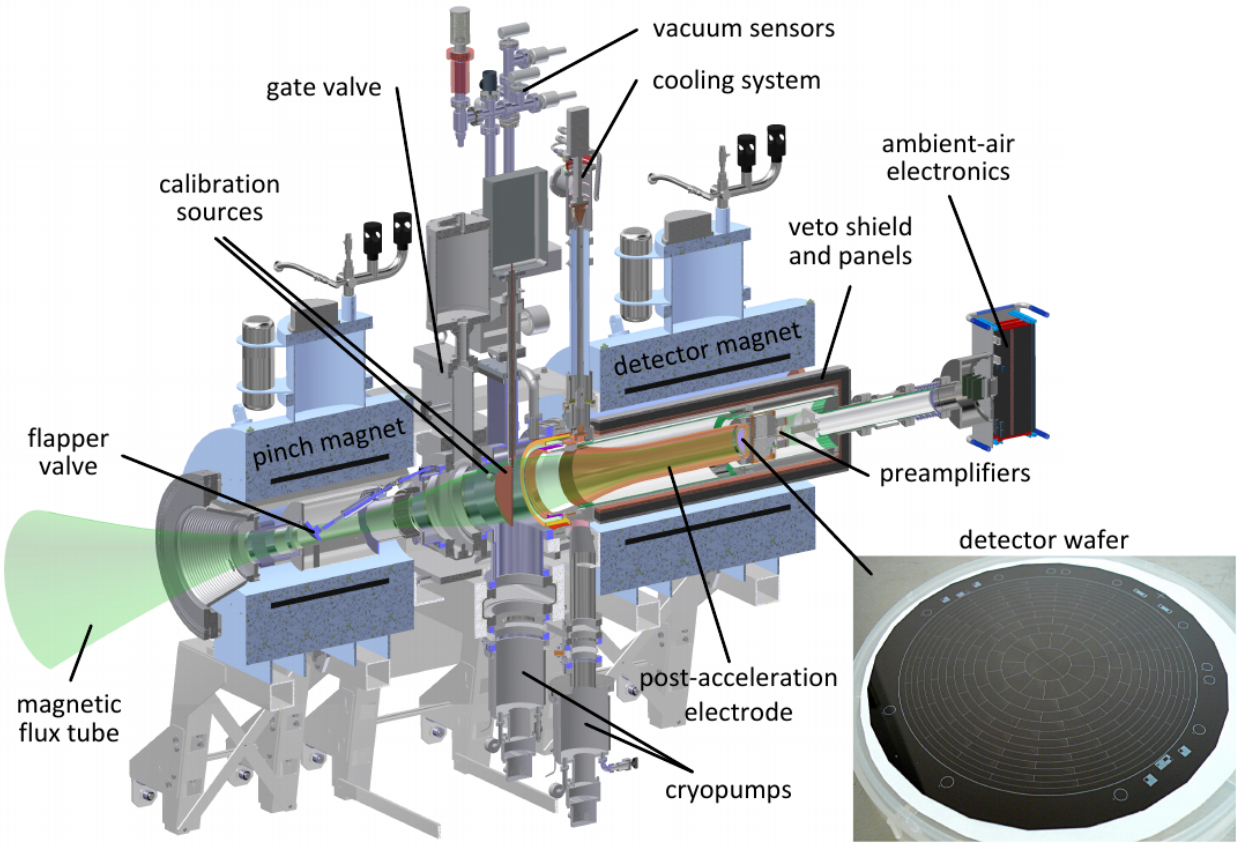

Figure 2.8: The KATRIN focal plane detector (FPD) placed inside the detector magnet which guides electrons onto the detector wafer. The segmented structure of the wafer provides spatial resolution of the electron trajectories (from [Gro15]).

Two solenoids provide a magnetic field to guide the electrons from the main spectrometer to

the detector: the pinch magnet at the downstream end of the spectrometer with up to 6 T field and the magnet surrounding the wafer with 3.6 T. A detector signal goes via optical fibers to the data-acquisition system (DAQ) which processes the events using the ORCA (Object-oriented Real-time Control and Acquisition) DAQ software [How+04] for collecting and storing the data. ORCA also allows to control operational parameters of the FPD system. Additionally, a post acceleration electrode (PAE) placed in front of the detector can accelerate electrons using voltages up to 10 kV. This helps to improve the signal-to-noise ratio of the system and makes electrons with energies below 5 keV detectable for the FPD [Har15].

2.4 The MAC-E filter

The working principle of the KATRIN spectrometer as a tool for precision energy analysis of tritium β-electrons is based on the magnetic adiabatic collimation with electrostatic (MAC-E) filtering technique. The idea of such a device was proposed in 1980 by Beamson et al. [BPT80] and has been successfully implemented in the Mainz [Pic+92a] and Troitsk [LS85] experiments. The spectrometer in this case works as a high-pass filter transmitting only those electrons which have enough energy to overcome the retarding potential which allows to measure an integrated spectrum of the electrons. In the following, the key features of the KATRIN MAC-E filter is presented.

Figure 2.9 illustrates the MAC-E filter working principle. At the source side electrons enter a spectrometer having different pitch angles $\theta = \angle(\vec{B}, \vec{p})$ of their momentum $\vec{p}$ to the magnetic field $\vec{B}$ at this point. Therefore, their total kinetic energy E_{kin} is split between longitudinal ($E_{\parallel}$) and transversal ($E_{\perp}$) parts wrt. the magnetic field lines:

$$E_{kin} = E_{\parallel} + E_{\perp}, \tag{2.1}$$

$$E_{\parallel} = E_{kin} \cos^2 \theta = E_{kin} \left(\frac{\vec{B} \cdot \vec{p}}{|\vec{B}||\vec{p}|} \right)^2, \tag{2.2}$$

$$E_{\perp} = E_{kin} \sin^2 \theta = E_{kin} - E_{\parallel}. \tag{2.3}$$

The electrons will follow the magnetic field lines in a cyclotron motion, having an orbital magnetic momentum

$$\mu = |\mu| = \frac{q}{m_e} |\vec{l}| = \frac{E_{\perp}}{B} \tag{2.4}$$

with $\vec{l}$ denoting the orbital angular momentum, q and m_e the electron charge and mass. On their way, the magnetic field drops by several orders of magnitude, which is in case of the KATRIN main spectrometer from B_{max} =4.5 T at the pre-spectrometer side to B_{min} =0.3 mT in the middle. This gradient creates a force

$$\vec{F}_{\nabla} = \nabla(\vec{\mu} \cdot \vec{B}) \text{ (non-relativistic case)}, \tag{2.5}$$

which causes an acceleration of electrons parallel to magnetic field lines. Since the magnetic field changes slowly along the electrons' paths (an early onset of the electric retarding potential ensures a low relative change of the magnetic field strength within one cyclotron loop), electrons are transported adiabatically and the magnetic momentum μ is conserved. In adiabatic motion, the total kinetic energy of an electron is conserved. Therefore, the increase of the longitudinal kinetic

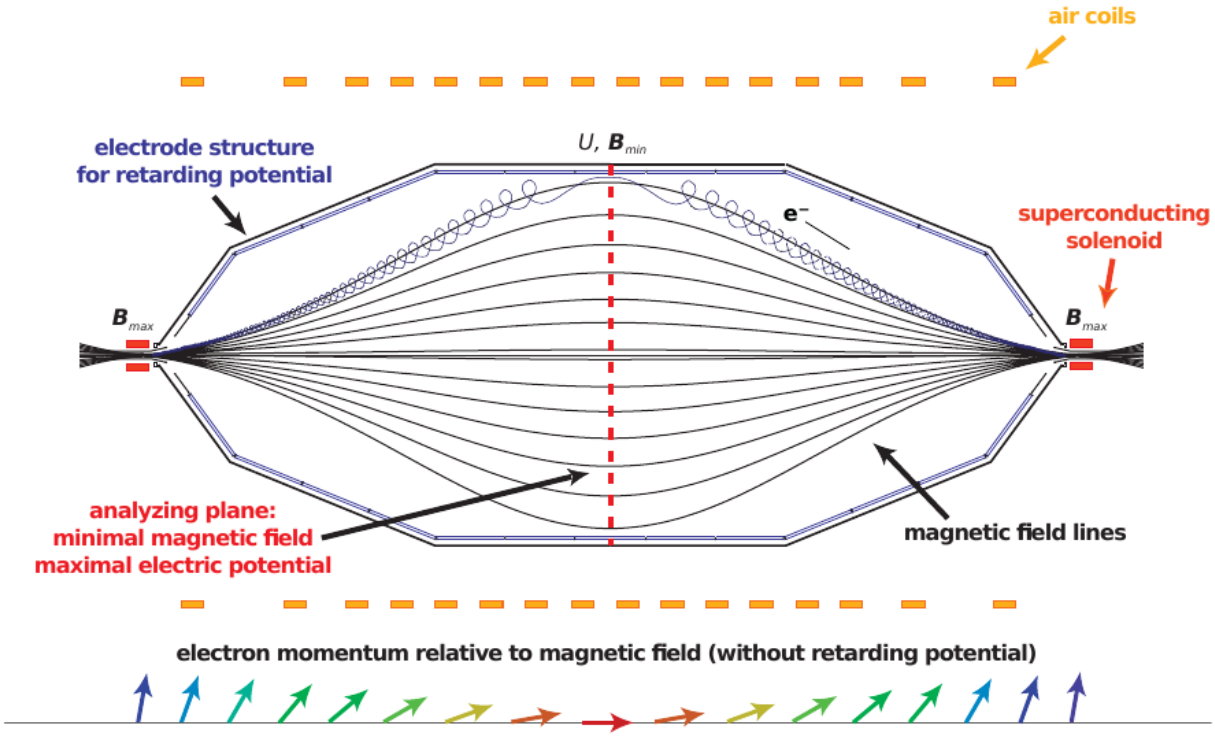

Figure 2.9: Schematic illustration of a MAC-E filter technique as is realized in the KATRIN main spectrometer. Electrons starting at the source side (on the left) are guided in a cyclotron motion (an electron trajectory is denoted by a solid blue line) by the magnetic field produced by the superconducting solenoids and fine-tuned by the air coiled system. Due to adiabatic movement in such a field, the total kinetic energy of the electron transforms almost fully to the longitudinal component which is decisive in whether the electron will pass the electrostatic barrier at the analyzing plane (red dashed line). The electron momentum transformation (without influence of the electric field) is shown with the arrows at the bottom of the picture. Energy resolution of the spectrometer is defined by the maximal amount of transverse energy remaining at the analyzing plane. Adapted from [Val09].

energy leads to an according decrease of the transverse energy. The transformation of the transverse energy component and the pitch angle can be derived from

$$\mu = \text{ const } \Rightarrow \frac{E_\perp}{B} = \frac{E'_\perp}{B'} \tag{2.6}$$

$$\Rightarrow \sin^2\theta' = \sin^2\theta \frac{B'}{B} \tag{2.7}$$

which means that the pitch angle is defined only by the ratio of the magnetic field strengths on the electron's way.

This effect is the basis of the MAC-E filter working principle: the drop of the magnetic field makes electrons with initially different pitch angles fly almost parallel to the magnetic field lines against the electric potential wall at the middle of the spectrometer (analyzing plane, with maximum of the electric potential and minimum of the magnetic field). This allows only those electrons to pass the filter which have a large enough total kinetic energy. For the electrons which make it over the electrostatic barrier, the energy transformation is reversed when they are re-accelerated towards the high magnetic field and low electric potential at the detector side.

The theoretical resolution of a MAC-E filter is defined by the maximum remaining transverse energy $(E_\perp)_{max}$ an electron has at the analyzing plane in the extreme case when its total kinetic energy at the starting point E_{start} is fully transversal (from eq. (2.6)):

$$\Delta E \equiv (E_\perp)_{max} = E_{start}\frac{B_{min}}{B_{max}}. \tag{2.8}$$

This gives for an electron with E_{start} =18.6 keV and the design magnetic field values of B_{min} =0.3 mT and B_{max} =6 T a spectrometer resolution of 0.93 eV.

If the electron source would coincide with the maximal value of the magnetic field along the whole beamline, electrons with initial pitch angles θ_{start} up to 90 ° would be accepted. However, in KATRIN the magnetic field at the WGTS is 3.6 T but the maximal magnetic field is at the pinch magnet positioned at the exit of the main spectrometer, therefore the maximal acceptance angle θ_{max} (from eq. (2.7)) is

$$\theta_{max} = \arcsin\sqrt{\frac{B_{source}}{B_{max}}} = 50.77°, \tag{2.9}$$

and all the electrons with θ_{start} exceeding θ_{max} are magnetically reflected.

If U_0 is a retarding potential applied to the spectrometer, then its transmission function can be given by [Pic+92b]

$$T(E_{start}, qU_0) = \begin{cases} 0 & \text{if } E_{start} < qU_0, \\ 1 - \sqrt{1 - \frac{E_{start}-qU_0}{E_{start}} \cdot \frac{B_{source}}{B_{min}}} & \text{if } qU_0 \leq E_{start} \leq qU_0 + \Delta E, \\ 1 - \sqrt{1 - \frac{B_{source}}{B_{max}}} & \text{if } E_{start} > qU_0 + \Delta E, \end{cases} \tag{2.10}$$

with the reduced maximal amplitude

$$T_{max} = 1 - \sqrt{1 - \frac{B_{source}}{B_{max}}}. \tag{2.11}$$

The transmission function is graphically represented in fig. 2.10: magnetic mirroring effect occurring at the pinch magnet at the exit of the spectrometer due to asymmetric magnetic field strength reduces the transmission function.

To characterize the transmission properties of the spectrometers, different calibration sources are used in KATRIN. One of them is the angular-selective electron gun which provides electrons with defined energies [Beh16]. Another one is the Condensed Krypton Source (CKrS) [Dyb18] isotropically emitting electrons with well-defined energies in various monoenergetic lines and allowing a pixel-wise calibration of the transmission function. The CKrS is discussed in detail in the next chapter.

2.5 Sensitivity to the electron (anti)neutrino mass

Assuming the β-electron rate provided by the WGTS is stable, the rate after the MAC-E filter will be determined by the retarding potential U_0 applied to the spectrometer and the ratio of magnetic fields B_{max} and B_{min} defining the transition function $T(E_{start}, qU_0)$ (see eq. (2.10)). Therefore, uncertainties of the electromagnetic fields will directly influence the detected rate introducing in

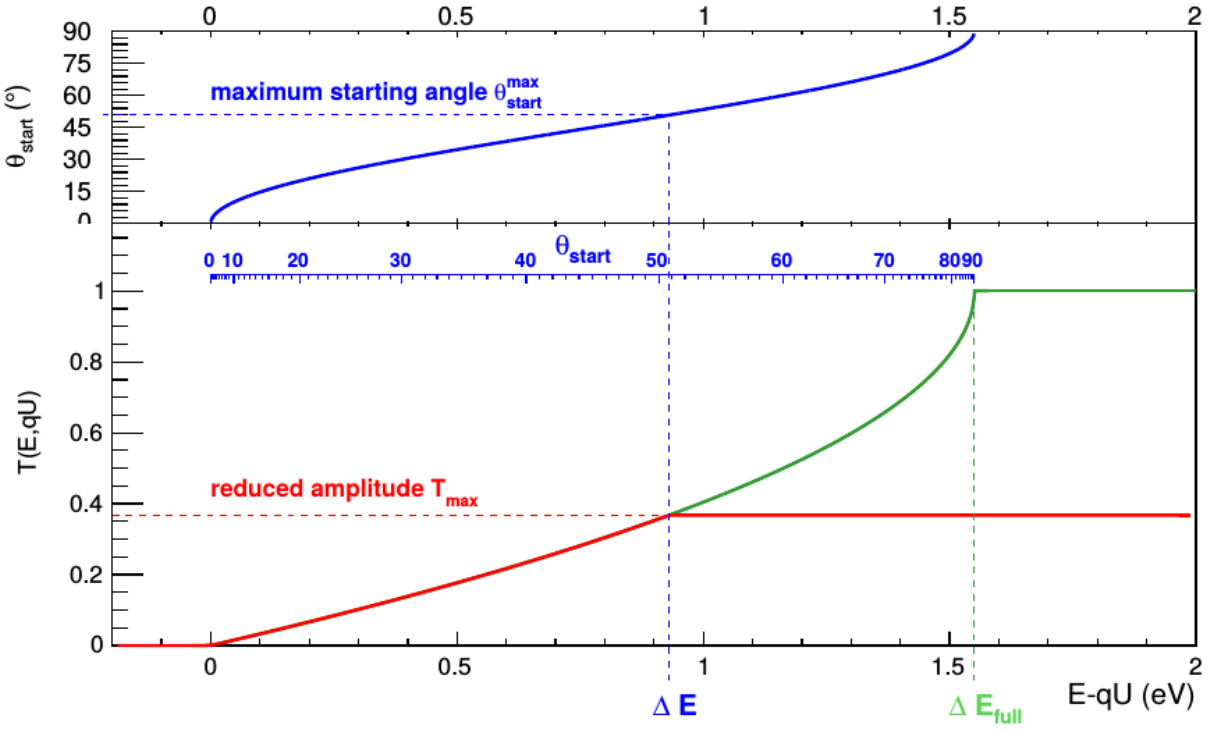

Figure 2.10: Analytically calculated transmission function of a MAC-E filter according to (2.10) at the example of the KATRIN main spectrometer (lower plot) and the electron starting angle θ_{start} for electrons near the spectrum endpoint that corresponds to a given surplus energy. From [Zac15].

this way a systematic uncertainty in the measurement. Another source of systematic uncertainty is scattering of β-electrons on tritium gas which is contained at rather high pressure inside the WGTS: as has been estimated in [Bab+12], only 40% of the electrons leave the source unscattered, and the rest of them experience at least one scattering on their way. Inelastic scattering will result in an energy loss of the electrons and they will have a higher chance to be lost by being reflected in the MAC-E filter. This scattering process is taken into account by a response function $R(E, qU_0)$ which is a convolution of the transmission function $T(E_{start}, qU_0)$ and an energy loss model [Han+17], [KK05]. Then, the electron rate $\dot{N}_{signal}$ detected after the spectrometer is given by

$$\dot{N}_{signal}(qU_0, E_0, m_{\nu_e}) = N_{tot} \int_0^{E_0} \frac{d\dot{N}_\beta}{dE}(E, E_0, m_{\nu_e}^2) R(E, qU_0) dE, \tag{2.12}$$

where N_{tot} is the number of tritium nuclei in the source, E_0 is the tritium endpoint energy and m_{ν_e} is the neutrino mass.

Low-energy electrons created inside the main spectrometer can reach the detector and create a background for the β-spectrum. Therefore, the β-spectrum which will theoretically be detected in the experiment has to be increased by the background rate $\dot{N}_{background}$:

$$\dot{N}_{theory}(qU_0, E_0, m_{\nu_e}, \dot{N}_{signal}, \dot{N}_{background}) = \dot{N}_{signal}(qU_0, E_0, m_{\nu_e}) + \dot{N}_{background}. \tag{2.13}$$

This is the model which is fitted to the rate measured by KATRIN (see fig. 2.11) and it has four free parameters: the neutrino mass m_{ν_e}, the endpoint energy E_0, the signal amplitude N_{tot} and the background rate $\dot{N}_{background}$. As was stated in section 1.4.4, sensitivity to the neutrino mass

is best close to the endpoint. However, to determine the other parameters (signal amplitude and background rate), a part of the measurement time has to be spent above and further below the endpoint. A detailed investigation of the measurement time distribution optimization was done in [Kle14].

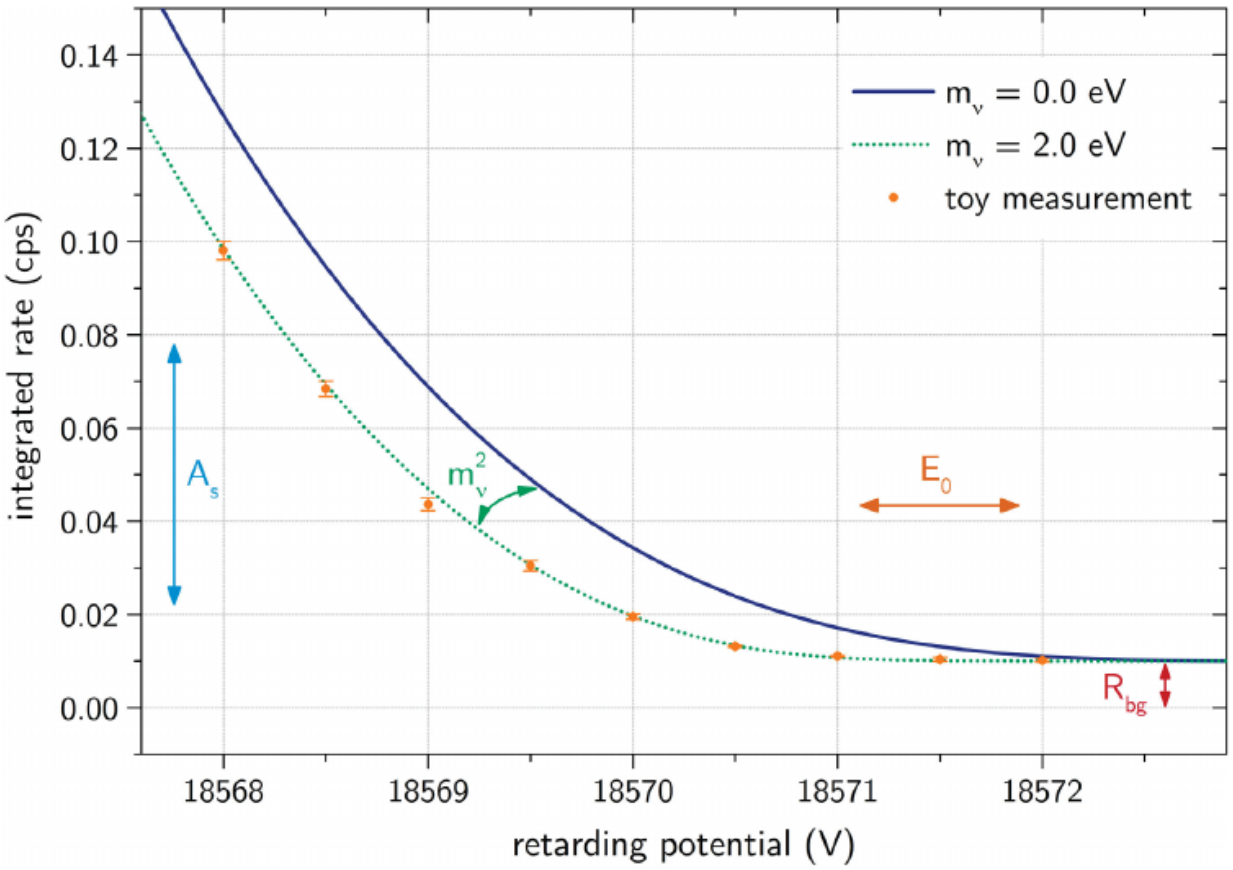

Figure 2.11: Simulation of the integral tritium β-spectrum measurement in KATRIN: theoretical calculations for m_{ν_e}=0 eV and m_{ν_e}=2 eV are shown by the solid blue line and the dotted green line correspondingly. The orange dots represent simulated measurement data in case m_{ν_e}=2 eV (assuming Poisson statistics for signal and background rates). From [Kle14].

2.5.1 Systematic uncertainties

Since the target sensitivity of KATRIN is $m_{\nu_e} \leq 0.2\,\mathrm{eV/c^2}$ (90% C.L.), the overall experimental uncertainty $\sigma_{abs} = \sqrt{\sigma_{sys}^2 + \sigma_{stat}^2}$ should not exceed $0.025\,\mathrm{eV^2}$. By design, the systematic uncertainty is aimed to stay $\sigma_{sys} \leq 0.017\,\mathrm{eV^2}$ [KK05]. The main sources of the systematic uncertainties are:

- Parameters which affect the transmission function, *e.g.* inhomogeneities of the retarding potential and the minimal magnetic field at the analyzing plane lead to a radial dependence of the transmission function. Fluctuations of the high voltage and magnetic fields, which are caused by power supplies of the HV system, solenoids and air coils, also affect the transmission function. In particular, the retarding potential of −18.6 kV has to have stability better than 61 mV (*i.e.* 3 ppm) to fulfill the requirement for each individual systematic effect to give an uncertainty contribution not more than $0.0075\,\mathrm{eV^2}$ to fit the allowed overall systematic uncertainty budget [KK05].

- The tritium column density at the WGTS determines the decay rate and the scattering probability in the source. An optimum of the column density where the maximal rate to generate enough statistics while the scattering is minimal should be used. Instabilities of the column density contribute to the systematic uncertainty as well. There are several tools to monitor the column density: the rear-section electron gun located on the upstream side of the WGTS [Bab14]; a Beta Induced X-Ray Spectroscopy (BIXS) detector to observe X-rays induced by decay electrons hitting the rear-wall; the forward beam monitor (FBM) to measure the "halo" of the β-electron flux tube; a Laser Raman Spectroscopy (LARA) system to control the composition of the inlet gas affecting the final states distribution (FSD) [Bab+12], [Fis14].

- The FSD of the $(HeT)^+$ daughter molecule also influences the measured β-spectrum. The lowest electronic excited state of the molecule has an energy of 24 eV and can be cut out since the high energy resolution of KATRIN allows to measure in the small energy region of 20 eV below the endpoint. The electronic ground state which is populated in about 57% of decays has rotational-vibrational excitations which smear out the spectrum endpoint. Furthermore, for the FSD modelling, the contributions from molecules like TH and TD must be taken into account [OW08], [KK05], [Kle14].

2.5.2 Statistical uncertainties

The design value of the statistical uncertainty in KATRIN is σ_{stat} =0.018 eV^2 achievable in 5 calendar years of operation including calibration and maintenance (or in 3 years of pure measurement time). For this, the background is required to be minimized at a level of 10 mcps. Since in the close vicinity of the endpoint the sensitivity to the neutrino mass is largest but the count rates from β-decay are very small, and at the same time further away from the endpoint the β-decay signal is larger but the influence of the neutrino mass on the spectrum is significantly weaker, the measurement time distribution needs to be optimized to push down the statistical uncertainty as much as possible. The major known background sources in the KATRIN are:

- Processes in the detector such as nuclear decays, minimized by a careful selection of the materials, and incidence of cosmic muons against which a muon veto system is provided;

- Electrons from the spectrometer vessel walls and inner electrodes. They are generated by cosmic particles, from radioactive decays in the stainless steel (*e.g.* of radon isotopes ^{219}Rn, ^{220}Rn, ^{222}Rn) [Wan13], [Gör14], [Frä+11], [Mer+12], [Wan+13] or from regions with high electric fields like sharp edges or boundaries between components due to field emission. All of those are efficiently shielded by the axial symmetric magnetic fields in the spectrometer and by the electrostatic shielding of the inner electrode in the spectrometer.

- Magnetically stored particles. Electrons with transverse energies above 1 eV created in the spectrometer volume can be stored by the magnetic mirror effect (by being reflected by the high magnetic fields at the entrance and the exit of the spectrometer). They can ionize residual gas and create secondaries which will be stored as well. Some of the low-energetic electrons will be able to reach the detector and will have an overlap in energy with signal electrons.

- A recently found background source in the ionization of hydrogen Rydberg states by blackbody radiation in the spectrometer. Since the Rydberg states are neutral and therefore not affected by electromagnetic shielding they can freely propagate into the spectrometer volume and contribute to the observed background [Dre15].

- Particles stored in the Penning traps occurring because of specific configurations of electric and magnetic fields. Such traps can appear in the region of electrodes in the spectrometer and can be prevented by careful electromagnetic design to avoid trapping conditions. However, an unavoidable Penning trap occurs between pre- and main spectrometers when both are operated at electric potential. It can cause severe problems not only by increasing background due to stored electrons, but also by possible discharges which can harm the spectrometer hardware. This inter-spectrometer Penning trap and a countermeasure against its effects are discussed in the chapter 4.

Chapter 3

Ellipsometry at the Condensed Krypton Source

To achieve its sensitivity goal, KATRIN needs an absolute energy calibration, monitoring and precise determination of the transmission function of the spectrometer. For that, it exploits a number of diagnostic tools which are based among others on utilizing ^{83m}Kr. This isotope provides a natural nuclear standard due to the emission of conversion electrons. The electrons have well-defined energies allowing for energy calibration of the spectrometer voltage with a precision of 3 ppm [Are+18a] and have an isotropic angular distribution which can be used for studies of the broadening of the spectrometer transmission function.

One type of the ^{83m}Kr-based source are *implanted* $^{83}Rb/^{83m}Kr$ *sources* [Zbo+13] which are used at the additional monitor spectrometer (a re-used spectrometer from the Mainz experiment) sharing the high voltage with the main spectrometer. These consist of graphite crystals in which ^{83}Rb is implanted. Inside the crystal, ^{83}Rb decays into ^{83m}Kr , which in turn will decay emitting conversion electrons. A disadvantage of this type of source is scattering of electrons inside the material which leads to smearing and energetic shifts of the spectral lines. On the other hand, such a source is relatively easy to handle.

Alternatively, a *gaseous* ^{83m}Kr *source* (GKrS) can be used in KATRIN. For its preparation, a certain amount of gaseous ^{83m}Kr emanated from ^{83}Rb is injected into the WGTS. Therefore, its use requires readjustment of the WGTS section. It can be used to study transport of electrons and the source characteristics. In contrast to the implanted source, scattering in the GKrS is minimal.

Finally, ^{83m}Kr is applied in the form of a *condensed krypton source* (CKrS), which was initially used at the Mainz neutrino experiment [Pic+92b] and was redesigned for use at KATRIN in the theses of B. Ostrick [Ost09] and S. Bauer [Bau14]. At present, the CKrS is installed at the end of the KATRIN CPS before the pre-spectrometer. In such a source, krypton obtained from a Rb emanator is quench-condensed at about 25 K onto an HOPG (Highly Oriented Pyrolytic Graphite) substrate. An advantage of such a source is the absence of scattering inside the source volume as for implanted sources, a feasibility for regular use during intermissions of the tritium β-spectroscopy and a point-likeness which makes possible per-pixel scans of the flux tube in contrast with the GKrS. However, in the CKrS the spectral line parameters (position, width) are dependent on the purity and thickness of condensed krypton films. To control this, ultra-high vacuum conditions are created in the substrate region of the CKrS and the set-up is equipped with a laser ellipsometry set-up to

monitor the film parameters. A novel ellipsometry method was developed in [Bau14] taking into account the special geometry of the KATRIN CKrS. The set-up was installed and commissioned at the CPS in 2017 which has been reported in the thesis of S. Dyba [Dyb18].

In this chapter, an introduction to conversion electrons of ^{83m}Kr is given, followed by an overview of the CKrS set-up and a description of the ellipsometry method. Lastly, the results of the ellipsometry analysis of the condensed krypton films used in the krypton measurement campaigns in 2017 and 2018 are presented and discussed. The measurements described here have been planned and performed by A. Fulst and myself with a lot of discussion and advice from V. Hannen and C. Weinheimer; the ellipsometry analysis was done by myself, while the spectroscopic analysis referenced here is done by A. Fulst and will be discussed in his PhD thesis [Ful19].

3.1 ^{83m}Kr conversion electrons

The phenomenon of internal conversion is that an atomic nucleus in an excited state can de-excite by transferring energy to one of the electrons in the atomic shell which gets emitted as a result. A virtual photon is involved in the process of internal conversion which is competing with γ-radiation. This competition between γ-radiation and internal conversion is characterized by the total coefficient of internal conversion α, which is equal to the ratio of the probabilities of electron emission T_e to the probability of emission of a γ-quantum T_γ:

$$\alpha = \frac{T_\mathrm{e}}{T_\gamma}. \tag{3.1}$$

The kinetic energy of the conversion electron E_kin depends on the atomic binding energy E_b and the energy of the γ-transition E_γ:

$$E_\mathrm{kin} = E_\mathrm{b} - E_\gamma. \tag{3.2}$$

The magnitude of the internal conversion coefficient depends on the orbital of the emitted electron, on the parity of the transition, greatly increases with an increase of its multipolarity and with a decrease of its energy, and increases with larger nuclear charge.

The natural line width of the corresponding electron line is given by the uncertainty relation $\Gamma \cdot \tau = \hbar$ and can be represented as:

$$\Gamma = \frac{\hbar}{\tau_\mathrm{e}} + \frac{\hbar}{\tau_\gamma}, \tag{3.3}$$

where Γ is the full FWHM (width half maximum) of the line and τ_e and τ_γ are lifetimes of the electron hole and the nuclear transition. The line shape then can be expressed by a Lorenz distribution:

$$L(E, E_0, \Gamma, A) = A \cdot \frac{\frac{\Gamma}{2}}{(E - E_0)^2 + (\frac{\Gamma}{2})^2}, \tag{3.4}$$

where A denotes the amplitude of the distribution, E_0 the central energy (position of the peak) and E the electron energy [Zbo11].

^{83m}Kr provides conversion electrons in the energy range from 7 keV to 32 keV including the K-32 line with energy which lies close to the tritium endpoint, and small line width, see fig. 3.1. Its

half-life $T_{\frac{1}{2}}$ is short enough to use it inside the flux tube without a risk of a long-term contamination of the experiment and the half-life of its mother isotope ^{83}Rb (86.2 d) is long enough to provide sufficiently high activity over longer measurement periods.

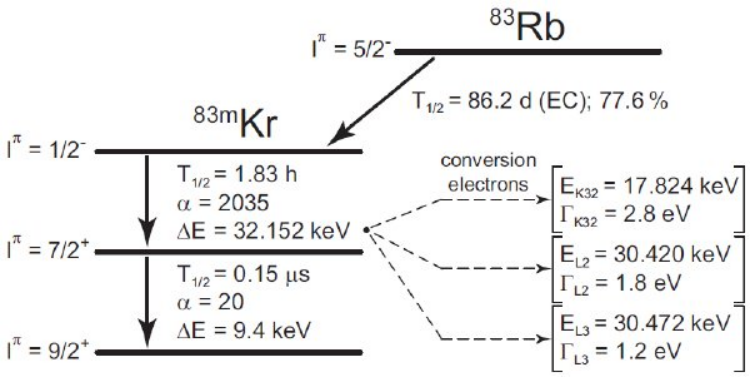

Figure 3.1: Decay diagram of ^{83m}Kr and its mother isotope ^{83}Rb. ^{83}Rb decays via electron capture (EC) with a half-life of 86.2 d into the metastable ^{83m}Kr isomer. This metastable state reaches the ground state via emanation of gammas or conversion electrons. Figure from [Thü07].

^{83}Rb with a half-life 86.2 d generates ^{83m}Kr via electron capture. The metastable state $I^\pi = \frac{1}{2}^-$ is populated with a probability of 77.6% and decays with a half-life of 1.83 h to an intermediate state $I^\pi = \frac{7}{2}^+$. This process is highly converted (conversion coefficient $\alpha = 2035$) and has a transition energy E_{32} =32 151.7(5) eV. After an other converted decay ($\alpha = 20$) with a half-life of 150 ns and a corresponding γ energy E_{32} =9405.8(3) eV the ground state $I^\pi = \frac{9}{2}^+$ is reached. Different conversion lines corresponding to electrons emitted from the K, L, M or N krypton shells are available for energy calibration, see table 3.1.

For a gaseous source, the conversion electron energy measured with a MAC-E filter can be written as [Zbo11]

$$E_{kin}^{gas}(i) = E_\gamma + E_{\mathrm{rec},\gamma} - E_{\mathrm{rec,e}}(i) - E_{\mathrm{bin}}^{\mathrm{vac}}(\mathrm{gas},i) - (\Phi_{\mathrm{spec}} - \Phi_{\mathrm{source}}) - C \tag{3.5}$$

with:

E_γ: energy of the γ

$E_{\mathrm{rec},\gamma}$: recoil energy of the nucleus after γ emission

$E_{\mathrm{rec,e}}(i)$: recoil energy after electron emission from the shell i

$E_{\mathrm{bin}}^{\mathrm{vac}}(\mathrm{gas},i)$: electron binding energy, from the shell i w.r.t. the vacuum level

Φ_{spec}: effective work function of the spectrometer

Φ_{source}: work function of the source

C: correction term for additional effects in a gaseous source

To describe a condensed krypton source, additional terms have to be included: the work function of an HOPG substrate, image-charge effects as a function of distance and terms describing surface effects (*e.g.* influence of residual gases on top of the substrate) [Ost09]. A dedicated model for the

Electron level and notation	**Atom rec. energy** $E_{rec,e}(i)$	**Kinetic energy** $E_{kin}^{gas}(i)$	**Intensity** I [%] **per** ^{83}**Rb decay**	**Lorentzian line width** $\Gamma(i)$ **recomm. [CP01]**	**exp. [Pic+92a]**	**(cond. Kr) [Ost09]**	**Instr. resol.** ΔE
γ transition M1		9405.8(4)	5.86(134)				
$2s_{1/2}$ L_1	0.05	7481.2(9)	70.32	3.75	5.30(4)	3.72(19)	0.4
$2p_{1/2}$ L_2	0.05	7673.8(4)	7.91	1.25	1.84(5)	1.29(14)	0.4
$2p_{3/2}$ L_3	0.05	7726.5(4)	5.07	1.19	1.40(2)	1.58(16)	0.4
$3s_{1/2}$ M_1	0.06	9113.0(5)	11.60	3.5	4.27(5)	3.123(4)	0.5
$3p_{1/2}$ M_2	0.06	9183.5(4)	1.30	1.6	1.99(32)	0.63(39)	0.5
$3p_{3/2}$ M_3	0.06	9191.3(4)	0.98	1.1	1.66(8)	1.1(4)	0.5
$4s_{1/2}$ N_1	0.06	9378.2(4)	1.43	0.4	0.19(4)	0.288(93)	0.5
$4p_{1/2}$ N_2	0.06	9391.1(4)	0.12	0.03[a]	-	0[b]	0.5
$4p_{3/2}$ N_3	0.06	9391.7(4)	0.09	0.03[a]	-	0[b]	0.5
γ transition E3		32151.7(5)	0.0358(45)				
$1s_{1/2}$ K	0.12	17824.3(5)	17.07	2.71	2.83(12)	2.70(6)	0.9
$2s_{1/2}$ L_1	0.20	30266.9(9)	1.13	3.75	-	-	1.6
$2p_{1/2}$ L_2	0.20	30419.9(9)	1.13	1.25	1.84(5)	1.165(69)	1.6
$2p_{3/2}$ L_3	0.21	30472.3(5)	27.42	1.19	1.40(2)	1.108(13)	1.6
$3s_{1/2}$ M_1	0.21	31858.8(6)	0.19	3.5	-	-	1.6
$3p_{1/2}$ M_2	0.21	31929.3(5)	2.99	1.6	1.99(32)	1.230(61)	1.6
$3p_{3/2}$ M_3	0.21	31937.0(5)	4.65	1.1	1.66(8)	1.322(18)	1.6
$3d_{1/2}$ M_4	0.21	32056.5(5)	4.69	0.07	-	-	1.7
$3d_{3/2}$ M_5	0.21	32057.7(5)	6.59	0.072	-	-	1.7
$3s_{1/2}$ N_1	0.21	32124.0(5)	0.02	0.4	0.19(4)	0.4	1.7
$3p_{1/2}$ N_2	0.21	32136.8(5)	0.27	0.03[a]	0.59(4)[c]	0.608(13)[c]	1.7
$3p_{3/2}$ N_3	0.21	32137.5(5)	0.41	0.03[a]			1.7

Table 3.1: Resume of ^{83m}Kr conversion electron lines (from [Dyb18], adaptation from [Bau14]). All values are stated in eV. The energy values of the M1 gamma transition stem from [Vé+06] and of the E3 gamma transition from [Sle13]. The corresponding intensities per rubidium decay are based on [V$\ddot{+}$76], [Wu+57]. The electron kinetic energies are given for gaseous krypton for $\Phi_{\text{spec}} = \Phi_{\text{source}}$ (eq. 3.5) with gamma energies given in the table and the binding energies from [Zbo11]. The electron line intensities per rubidium decay were determined using interpolated internal conversion coefficients listed in [Rö+78a], [Rö+78b]. The line widths are obtained from measurements with the former CKrS at the Mainz MAC-E filter.
a: no recommended values stated in [CP01].
b: natural line width fixed to 0 in the analysis [Bau14].
c: the lines N_2 and $N_3 - 32$ were analyzed as a single line $N_{2/3} - 32$ [Bau14].

actual CKrS in KATRIN is currently being developed as part of the thesis of A. Fulst [Ful19].

In the next section, the CKrS set-up and its working principle are described.

3.2 The CKrS set-up and its working principle

The condensed krypton source of the KATRIN experiment, dedicated to calibration and investigation of spectrometer transmission properties, is a complex set-up which sits on the top of the CPS before the pre-spectrometer. Its central part is the cold HOPG substrate on which ^{83m}Kr is condensed. The gaseous krypton is produced by an external ^{83}Rb generator connected to the substrate region through the valve and a thin capillary.

Fig. 3.2 displays a technical drawing of the CKrS, each part of which is succinctly explained in the next subsections.

The ellipsometry set-up and measurement technique are discussed separately in section 3.3.

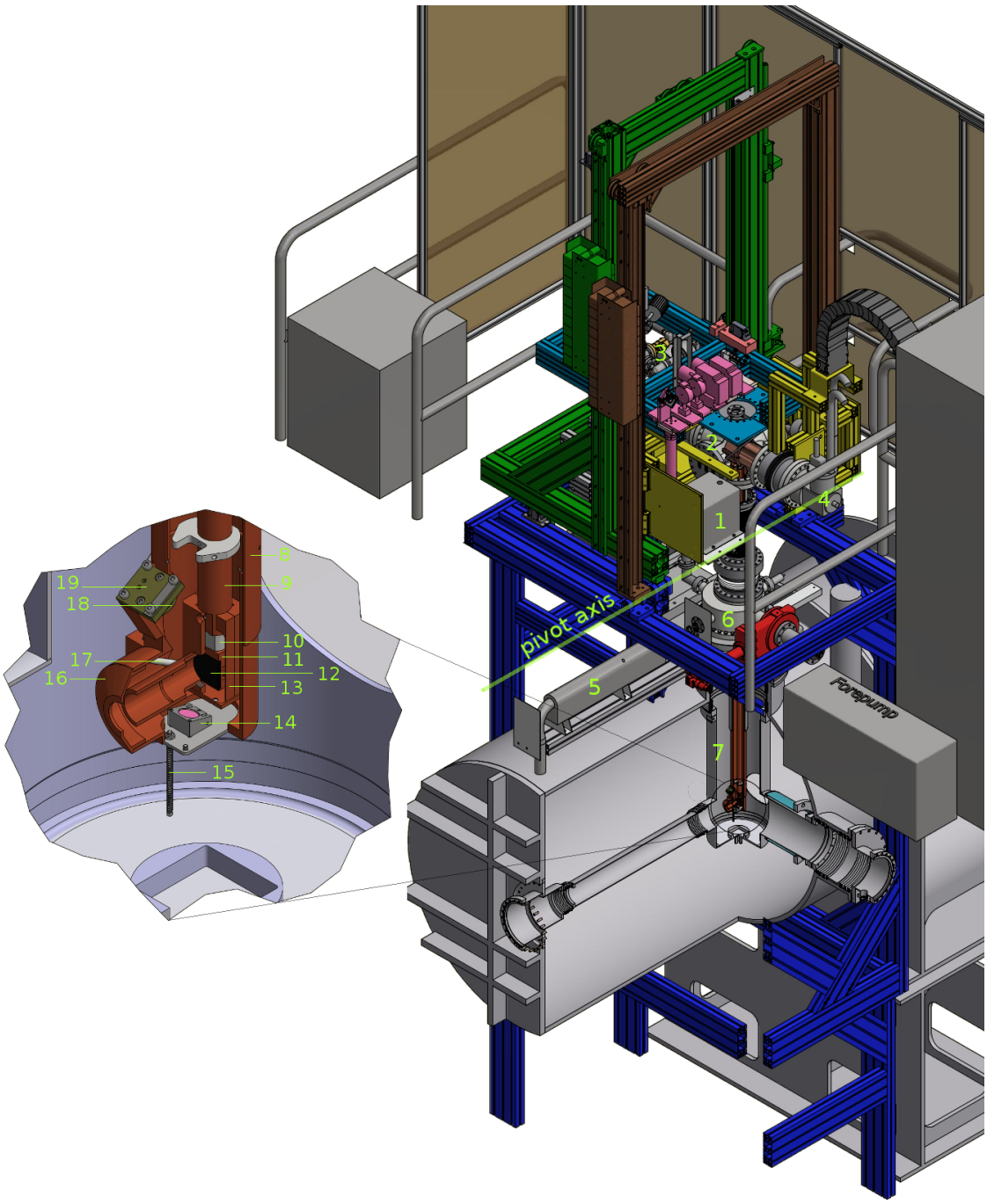

Figure 3.2: Technical drawing of the CKrS installed at the CPS. Different components are either color-coded or denoted by numbers for better differentiation. The system is hold by the mounting stage (blue) based on ground and on the platform inside the TLK. Vertical movement is provided by the carriages (turquoise and yellow) decoupling the vacuum pumps and cryocooler from the ellipsometry optics (pink) and the cold finger with the substrate. Horizontal movement is possible due to the tiltable frames (brown and green) which are at the same time the guiding rails for the carriages. Numbering: (1) - ^{83}Rb generator, (2) - vacuum system, (3) - gas system, (4) - coldhead, (5) - ablation laser, (6) - ablation chamber, (7) - main CKrS vacuum volume, (8) - outer cold shield, (9) - cold finger, (10) - steel spacer, (11) - substrate holder, (12) - HOPG substrate, (13) - inner cold shield, (14) - dielectric mirror, (15) - grounding pin, (16) - shielding lid, (17) - capillary nozzle, (18) - analyzer in a holder, (19) - ellipsometry photodiode backplate.

3.2.1 Holding and moving structure

The whole construction of the CKrS is supported by a scaffold system which combines fixed and movable frames allowing for short-term operations in-between tritium neutrino measurement runs and spatially-resolved investigation of the spectrometer transmission function.

Vertical movement is needed for the source to be able to enter and leave the CPS beamline and is allowed by linear motion of carriages (turquoise and yellow in fig. 3.2) along the guiding rails (green and brown in fig. 3.2), the latter themselves being a tiltable frame providing a possibility for horizontal movement and therefore scanning of the full flux tube. One of the carriages holds the main CKrS vacuum chamber, gas- and cryosystem and is decoupled from the other one, which carries the ellipsometry set-up and the cold finger with the HOPG substrate. This decoupling in combination with bellows connecting the parts reduces vibration transfer to the substrate.

The vertical movement is performed via a hoist driven by an ISEL EC 86L synchronous motor and IMD 40 controller. The set-up is additionally supplied with counterweights to compensate the load on the motor. The angular movement around the pivot axis (indicated in fig. 3.2) which adds the horizontal degree of freedom for the complete scan of the flux tube is guided by an ISEL EC 60 L synchronous motor with an IMD 20 controller.

The set-up is equipped with end-switches (Euchner GLBF05R08-552-M and GLBF04R08-552-M) placed at the edges of the movement range which generate stop-signals for the ISEL controllers to stop the motion when these positions are reached. For safety reasons, there is an additional backup line of end-switches (Euchner NM01WOK-M) to shut down the motor power supply.

The steering of the system and positioning at defined angle and radius with a pixel-wise precision is done via a LabView program, which has an additional integrated safety button for emergency shutdown of the motors. A pressure drop or a safety failure in the TLK infrastructure detected by KATRIN's PCS7 system will cause an automated movement of the source to its parking position.

3.2.2 Vacuum containment

In order to insert the CKrS into the CPS beam tube which has a pressure of about 10^{-10} mbar inside, the system has to have its own enclosure with similar ultra-high vacuum conditions, which also reduces freezing of residual gas along with krypton onto the substrate. A schematic view of the CKrS vacuum system with connections of the pumps to the cryo- and ablation chambers and gas system is shown in fig. 3.3. The upper cryochamber (mentioned in section. 3.2.1) is placed on one of the moving carriages, while the ablation chamber is mounted onto the CF250 full metal valve of the CPS (see fig. 3.2).

The CKrS volume is evacuated by a combination of a forepump (Adixen ACP15) and a turbo-molecular pump (TMP) (Leybold MAG W400 iP). Additionally, a non-evaporable getter pump (SAES MAG W 400 iP) is installed at the ablation chamber for removal of residual hydrogen (the pump has a pumping speed of 240 L/s for hydrogen). The cold finger and the inner cold shield act as additional cryopumps.

The pressure reading is done: a) at the cryochamber by an Oerlicon Leybold Ionivac ITR 90 vacuum gauge placed next to the TMP having a lower measurement threshold of 5×10^{-10} mbar, b) at the ablation chamber by a cold cathode gauge (Pfeiffer MPT-200), which is read out by the KATRIN PCS-7 system to trigger emergence extraction of the source in case of a vacuum failure (as

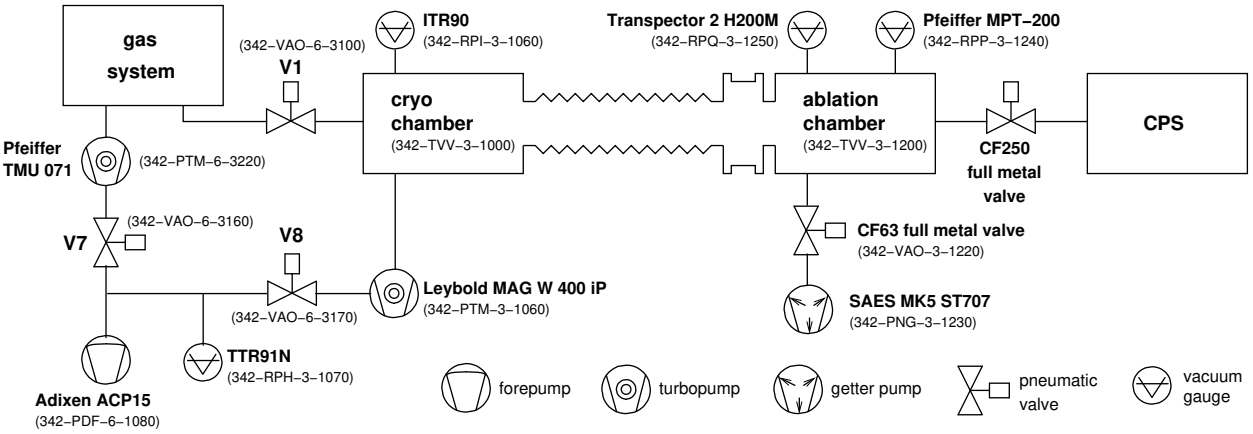

Figure 3.3: Schematic representation of the vacuum system. The system is pumped by a cascaded TMP and a pre-pump, connected via bellows and a getter pump mounted at the side of the ablation chamber.

was already explained in section 3.2.1), and c) at the forevacuum compartment by a Thermotron (Leybold TTR91N).

3.2.3 Gas handling system

The gas system of the CKrS delivers an adjustable flow of stable or radioactive krypton which is led along the cold shield of the CKrS through a heated capillary with a nozzle at its end to direct the gas onto the HOPG substrate. Stable krypton contained in a 0.5 l pressurized bottle on top of the mixing chamber can be used to measure ellipsometry reference curves and for substrate pre-plating, while the radioactive ^{83m}Kr isomer produced by a rubidium generator serves as source of the monoenergetic electrons of the CKrS. For a controllable and reproducible film preparation and pre-plating, the system is operated from the LabView software which allows for an automated inlet and condensation of gas.

The gas system (see fig. 3.4) consists of the central mixing chamber with 5 valves and two pressure gauges (Oerlicon ITR90 and Leybold Ceravac CTR91). The mixing chamber is connected to the TMP through the valves V5 and V4 (the latter is connected to it via an aperture to avoid an overload on the pump) and from there to the forepump through the valve V7. Through the V3 valve, the mixing chamber is connected to the bottle with stable krypton, which has a manual pressure regulator. The connection between the V1 valve at the CKrS inlet and the mixing chamber is done through the precision valve V9 which can be operated with different opening width (by applying different voltages from 0 V (completely opened) to 20 V (completely closed)) and times to adjust the amount of gaseous krypton let from the mixing chamber to the substrate. An inflow through the valve V6 from the rubidium generator providing ^{83m}Kr in gaseous form is located between valves V1 and V9. An additional valve V2 is needed for a fast evacuation of the pipings in the region of the source. Closing of V2 and V9 and opening of V6 and V1 valves ensure that only ^{83m}Kr can flow towards the substrate.

From the V1 valve the krypton gas flow is directed via a stainless steel ⌀3 mm capillary which goes along the copper outer cold shield and ending with a nozzle to the HOPG substrate. To not allow krypton to freeze onto the capillary walls, the capillary is kept above ∼130 K by a weak

thermal coupling and an additional heating wire.

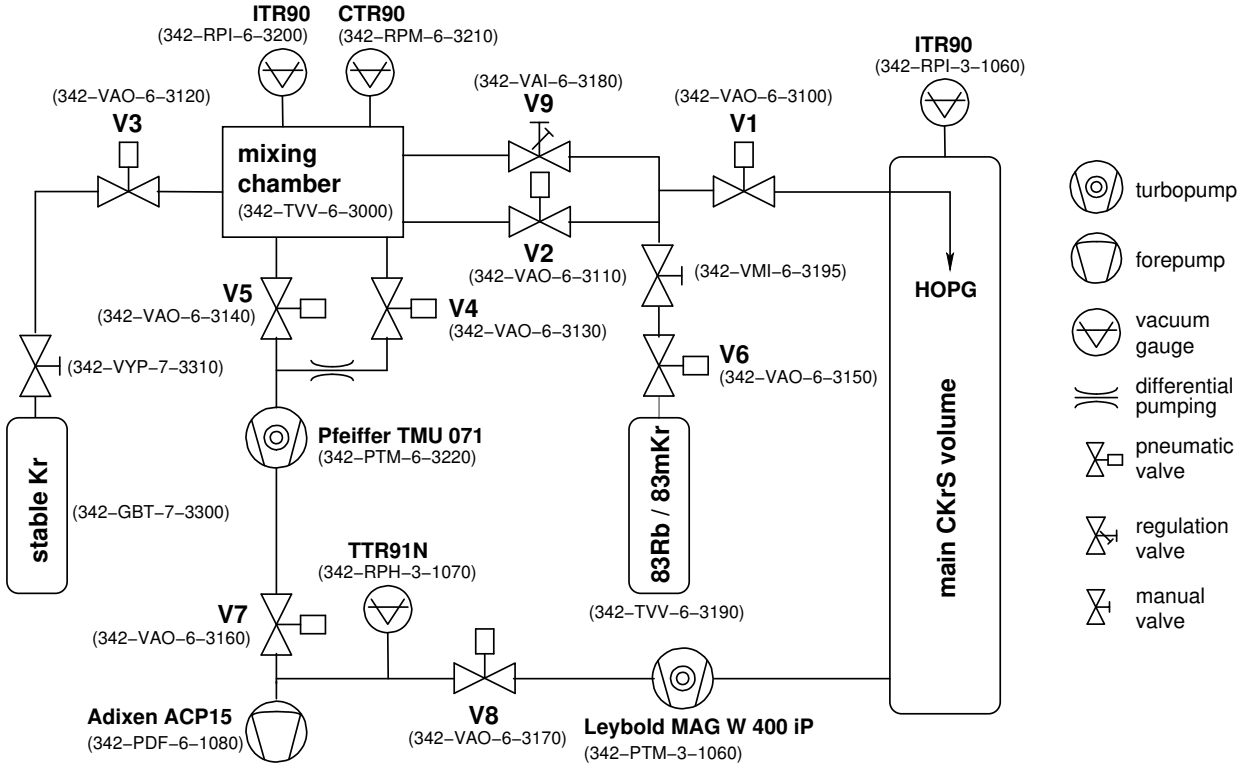

Figure 3.4: Schematic overview of the gas system. A stable krypton bottle is connected to a mixing chamber which allows to regulate an inflow of the gas to the substrate by regulating pressure in the mixing chamber. The ^{83m}Kr is supplied from the rubidium generator. Cascaded TMP and pre-pump allow to evacuate the system and pump out residual gases.

3.2.4 Cryosystem

To cool down the HOPG substrate to $\lesssim$30 K for krypton freezing, a two-staged cold head (Gifford McMahon Type RDK 408D by Sumitomo Heavy Industries Ltd.) is used. The first stage with a power of 34 W at 40 K is connected to the outer cold shield of the CKrS. The second stage with 1 W at 4 K is connected to the inner cold finger which supports and cools down the substrate fixed on a copper holder. The cold head is connected to the cold finger and outer cold shield with copper braids for a good thermal conductivity and to reduce vibration transfer from the cold head (to not disturb ellipsometry measurements). The temperature reading is done by eight Cernox (CX1050) sensors from Lakeshore: two at the copper holder of the substrate, two at different positions along the capillary, one on the nozzle, one at the outer and one at the inner cold shield and one at the dielectric mirror of the ellipsometry system.

3.2.5 HOPG substrate

The central part of the CKrS is the substrate on which gaseous krypton is condensed. As has been already mentioned in the previous sections, it is made of highly oriented pyrolytic graphite (HOPG) which has several advantages in such an application.

HOPG crystals have a laminate polycrystalline structure and form atomically smooth and stable

surfaces when cleaved. Layers of the graphite consist of carbon atoms arranged in a honeycomb pattern (see fig. 3.5) with an inter-atomic distance of 1.42 Å (such a 2D atomic plane is called graphene), are parallel to each other with a 3.35 Å spacing and are interconnected by Van der Waals forces, so the cleavage can easily be done by an adhesive tape which is used at the CKrS for the substrate preparation before the installation.

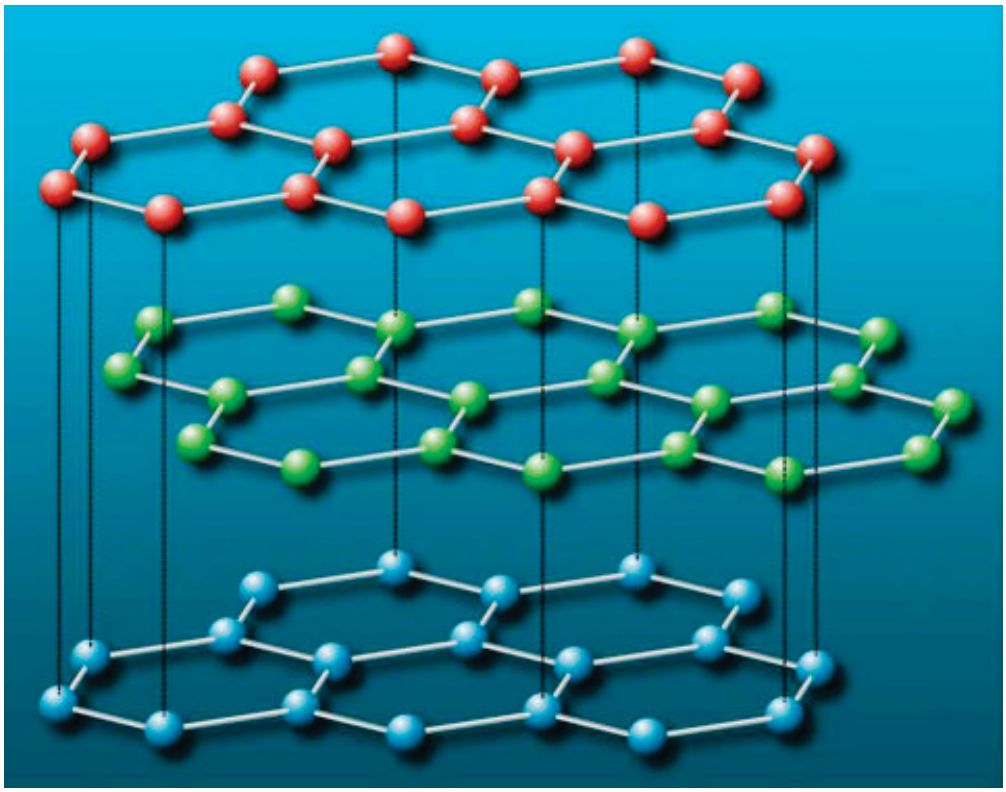

Figure 3.5: Schematic representation of the structure of the HOPG. The crystal consists of graphene layers (carbon atoms building hexagonal structure with a 1.42 Å side) with a mutual distance of 3.35 Å (from [Ost09]).

Being a layered polycrystal, HOPG resemble a mosaic of microscopic single-crystal grains slightly disoriented w.r.t. each other with non-zero angles w.r.t. the surface of the polycrystal. To describe the quality of an HOPG sample, the term "mosaic spread" is used. This characteristic is determined by measuring the FWHM of rocking curve [1] (of a Cu-K_α radiation peak). The highest quality HOPG crystals have a mosaic spread of ($0.4\,^\circ \pm 0.1\,^\circ$). This is the case for the 2 cm×2 cm substrate from Optigraph, model AGraphZ (ZyA/flat) used at the CKrS.

Another advantage of the HOPG for use as the substrate for the CKrS is its temperature-dependent anisotropy of thermal conductivity. Heating of an HOPG crystal to >100 K leads to heat conduction being mainly in-plane, with a negligible transversal component, which allows an effective cleaning of the substrate with laser ablation when the substrate is heated. The ablation system is discussed in subsection 3.2.6.

The substrate is mounted on a copper part to which it is attached via electrically conductive epoxy (Polytec EC101) allowing to apply an electric potential offset. The copper housing also

[1] The disorientation of graphene sheets is responsible for the broadening of the diffraction peak, measuring of which gives the rocking curve.

holds two temperature sensors and two 5 W Zener diodes (I15N3 by Surmetic) powered by a Tenma 72-2535 power supply for heating. To avoid harmful heat transfer from the substrate to the cold head, the copper holder is attached to the cold finger through a stainless steel spacer. Above the spacer, the inner cold shield is attached to the cold finger as a cold trap to reduce the flow of residual gas to the substrate.

The inner cold shield, as well as some parts of the ellipsometry set-up, are contained in the outer cold shield. As can be seen in fig. 3.2, a dielectric mirror, built into a stainless steel holder, is situated under the inner cold shield. Above the substrate, a section with a PEEK casing for the analyzer and the photodiode is provided (with a correct predefined orientation). The hole on the front of the outer cold shield is closed by a copper lid to shield the inner cold shield from the radiation of the warmer parts of the KATRIN. The lid has a $\varnothing 2$ cm opening in front of the substrate.

3.2.6 Laser ablation set-up

Prior to preparation of a radioactive film, the substrate has to be cleaned from frozen impurities since they would cause an undefined initial shift in line position and make spectroscopic measurement results from different films irreproducible and incomparable.

For that reason, a combination of a substrate heating from behind with two heating diodes (already described in subsection 3.2.5) and a laser ablation system is used. First, the substrate is heated by the diodes to ∼120 K which makes the substrate's conductivity essential in-plane with a suppressed perpendicular component and then is illuminated at a repetition rate of 10 Hz by 5 ns pulses for 180 s with a pulsed frequency-doubled Nd:YAG laser (Quantel Brilliant) which has an energy output $P_{\text{Nd:YAG}}$ =2 W and wavelength λ =532 nm through a diffuser (Thorlabs UVFS Ground Glass Diffuser DGU V10-600) which homogenizes the intensity distribution. A combination of the diffuser with a collimating lens (Thorlabs Plano Convex Lense LA 1027-A) allows to cover the whole surface of the substrate with a sufficiently high energy of $\mathcal{O}(300\,\text{m W cm}^{-2})$ to evaporate frozen gases. This is done when the substrate is retracted from the beam tube to the ablation chamber ("parking position") which has a window looking onto the substrate region.

3.2.7 Post-acceleration of the ^{83m}Kr electrons

The upper vacuum chamber sitting on one of the movable carriages as well as the bellow connecting the vacuum and the ablation chambers are isolated and electrically decoupled from the CPS. This allows to put the cold finger together with HOPG on max. 1 kV elevated electrical potential to allow electrons from the K-32 transition in ^{83m}Kr (with 17.8243 keV [Sle15] energy) to overcome an electrostatic barrier of the spectrometer of ∼18.6 kV. All electronics connected to the vacuum chamber are on the same substrate potential and are placed into an insulated HV-cabinet. The potential is produced by an HV-supply outside the HV-cabinet.

3.3 Ellipsometry system of the CKrS

The CKrS contains an ellipsometry system to monitor the properties of the krypton films frozen onto the HOPG substrate.

3.3.1 Working principle of PSCA ellipsometry and its technical realization at the CKrS

Ellipsometry techniques allow to investigate properties of multi-layer surfaces by analyzing light polarization after reflection. In case of the CKrS a null-ellipsometry type of this method is used. In this variant the light intensity measured by a detector after reflection is kept at a minimum by adjusting optical components through which the light passes.

At the CKrS, this technique is used to get information about thickness and quality of frozen films, since they influence spectral lines due to solid state effects. A basic scheme for a **PCSA** ellipsometry set-up as described in [Bau+13] is shown in fig. 3.6: a circularly polarized light beam passes through a linear **P**olarizer followed by a **C**ompensator (a quarter-wave plate) and then hits the **S**ubstrate nder test. The light reflected from the substrate passes through an **A**nalyzer (which is also a linear polarizer) onto a detector. Commonly, in such a set-up the compensator is fixed while the polarizer and the analyzer are allowed to rotate to search for the minimum of the intensity seen by the detector.

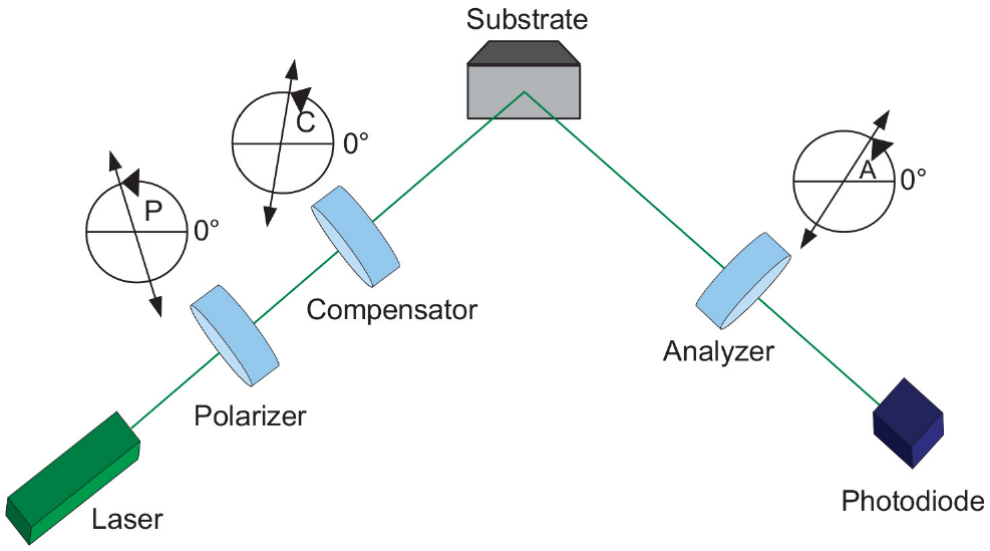

Figure 3.6: Schematic representation of the basic PCSA ellipsometry arrangement. Circularly polarized light from the laser passes through a linear polarizer and a compensator, whose angles define the direction of polarization of the light striking the sample consisting of the substrate and a condensed film. The polarization of the reflected light is analyzed by another linear polarizer (analyzer) and the outcoming intensity is registered by a photodiode detector.

The need to fit the CKrS into the CPS section imposes constrains due to the tight space available in the beam tube, the need to move the substrate and the cryogenic conditions which do not allow to use a remotely operated motor inside the main CKrS vacuum volume. Therefore, the scheme has been modified in such a way the compensator is made rotatable and the analyzer fixed instead. Additionally, the circularly polarized light (prepared by an additional fixed polarizer and a quarter-wave plate) is directed from the laser to the substrate by three dielectric mirrors which conserve the direction of polarization [Pet15]. A technical drawing of the CKrS ellipsometry set-up is shown in fig. 3.7. A light beam from a 543 nm-laser (Thorlab HGP005) is prepared outside the vacuum and then is guided through a window to a dielectric mirror which redirects the light onto

the film-substrate system. The reflected light then goes through the polarization filter (analyzer) and then to the detector (Si-PIN photodiode).

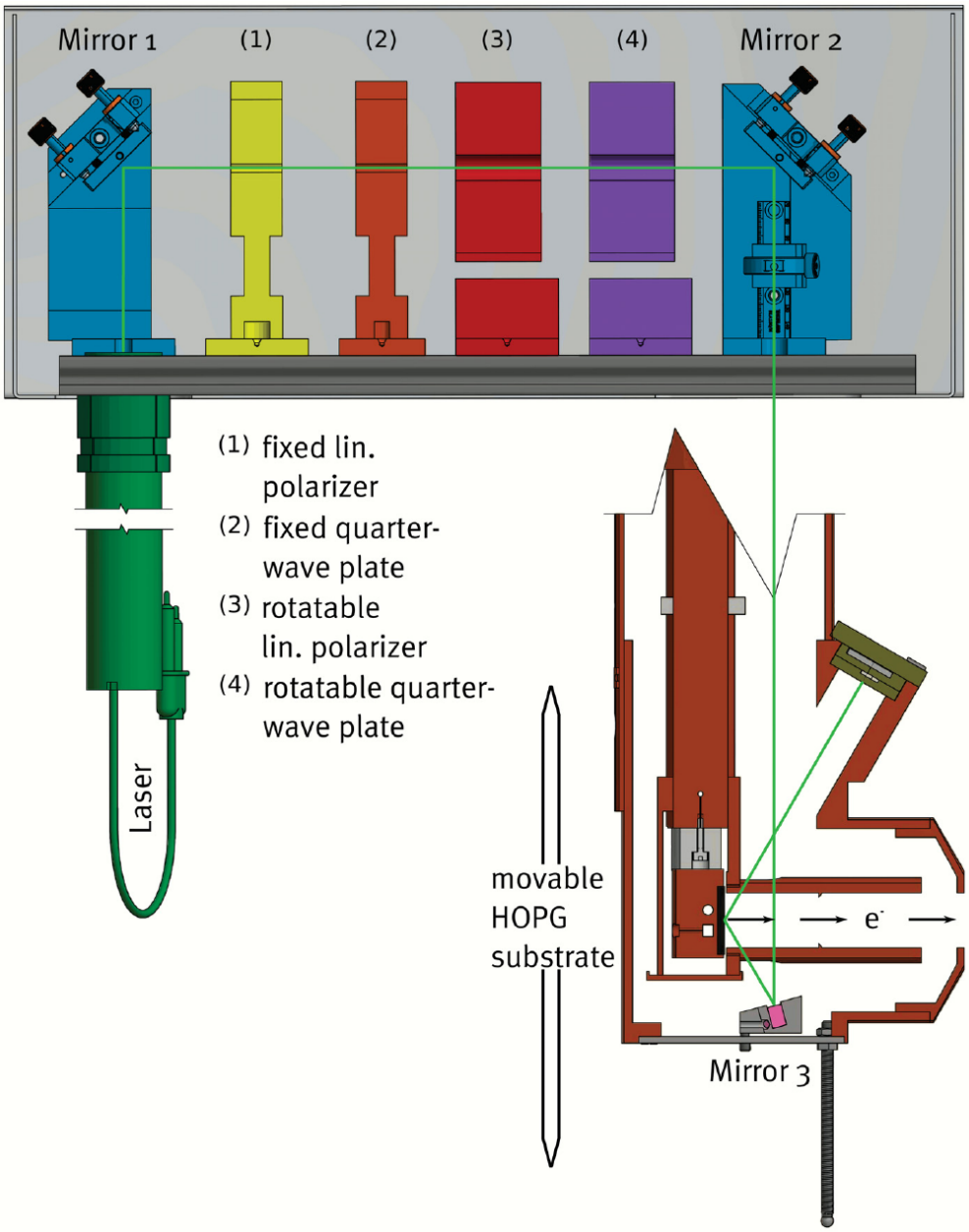

Figure 3.7: Technical drawing of the CKrS ellipsometry set-up. The green light (543 nm) from the laser is reflected from the first mirror and shines through the fixed linear polarizer (1) and a quarter-wave plate (2) which produce circularly polarized light. Then it goes through the rotatable linear polarizer and the rotatable compensator and afterwards is directed by the second mirror through the CKrS vacuum volume. The third mirror (pink) redirects the light towards the HOPG substrate (black), and the reflected beam goes through the fixed analyzer (beige) onto the photodiode (grey) which measures its intensity.

In the next subsection, a mathematical description of the ellipsometry method is given.

3.3.2 Null-ellipsometry

In the following, a mathematical expression of the ellipsometry method used at the CKrS is provided. A more detailed discussion of the standard PCSA variant can be found in [AB77] and the adaptation to the set-up with fixed analyzer have been done in [Bau14].

A polarized electromagnetic wave propagating in z-direction in an isotropic medium can be expressed as

$$\vec{E}(z,t) = E_s \hat{e}_s \cdot e^{i(\omega t - k_\omega z + \varphi_s)} + E_p \hat{e}_p \cdot e^{i(\omega t - k_\omega z + \varphi_p)}, \tag{3.6}$$

where (s) and (p) denote components perpendicular and parallel to the incidence plane respectively, E_s and E_p are the corresponding components of the wave, $\hat{e}_s$ and $\hat{e}_p$ are the basis vectors and φ_s and φ_p are the phases.

In the CKrS, the system under study can be considered as a three-phase (substrate - frozen film - vacuum) optical system. Fig. 3.8 shows schematically the interaction of light with such a structure. Indices 0, 1 and 2 correspond to the different media (ambient, film and substrate) with the refractive indices

$$\begin{aligned} N_0 = n_0 - ik_0 = n_0 = 1&\text{: ambient (vacuum),} \\ N_1 = n_1 - ik_1 = n_1&\text{: film,} \\ N_2 = n_2 - ik_2&\text{: substrate (HOPG),} \end{aligned}$$

where the film is assumed to be non-absorptive and the substrate to be isotropic.

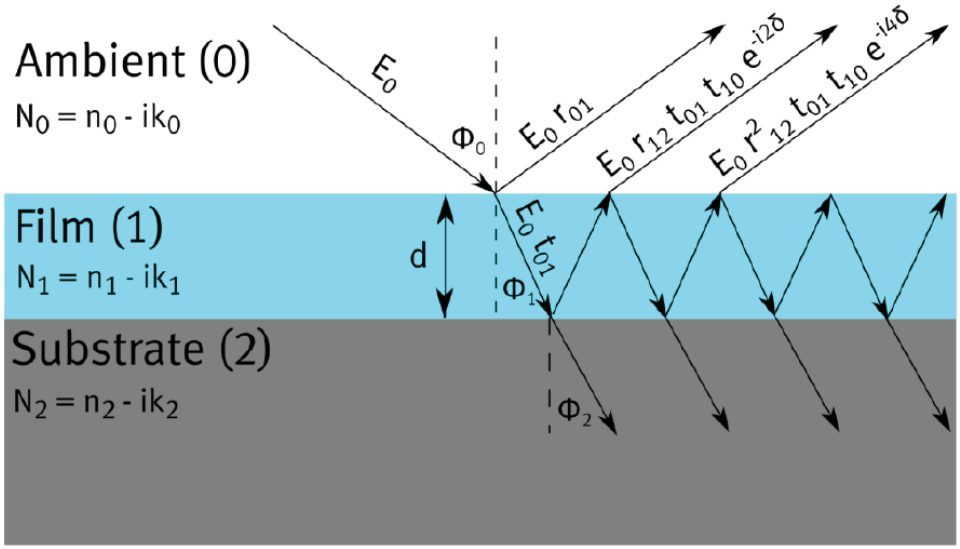

Figure 3.8: Interaction of light with a three-phase system (vacuum + substrate + film of thickness d): the incoming beam undergoes multiple partial reflections and transmissions.

The incidence wave is split on each interface into two new waves: reflected and transmitted, and this results into an infinite number of partial waves with amplitudes E_i decreasing according to a geometrical progression. Moreover, each of the waves has a phase shift with respect to the

precedent one of the same magnitude 2δ. This can be written as

$$E_{i+1} = r_{12} r_{10} E_i e^{-2i\delta}, \tag{3.7}$$

where r_{12} and r_{10} are the Fresnel reflection coefficients for the boundaries of the corresponding media. Then it is possible to obtain that

$$\delta = 2\pi \frac{d}{\lambda} \sqrt{n_1^2 - \sin^2 \Phi_0}, \tag{3.8}$$

where d is the film thickness, λ is the laser wavelength and Φ_0 is the initial incidence angle (see fig. 3.8). The reflected and the transmitted waves appear as a result of interference of the partial waves.

After summation over the members of the geometrical progression one obtains the following expression for the amplitudes of reflection in such a system:

$$R_{p,s} = \frac{r_{01p,s} + r_{12p,s} e^{-2i\delta}}{1 + r_{01p,s} r_{12p,s} e^{-2i\delta}}, \tag{3.9}$$

where $r_{ijp,s}$ are Fresnel coefficients of the corresponding interfaces for p- and s- polarizations:

$$r_{ijp} = \frac{N_j \cos \Phi_i - N_i \cos \Phi_j}{N_j \cos \Phi_i + N_i \cos \Phi_j}, \tag{3.10}$$

$$r_{ijs} = \frac{N_i \cos \Phi_i - N_j \cos \Phi_j}{N_i \cos \Phi_i + N_j \cos \Phi_j}, \tag{3.11}$$

where Φ denotes the angle between the incident ray and the surface normal which can be expressed using Snell's law $N_i \sin \Phi_i = N_j \sin \Phi_j$ as

$$\cos \Phi_1 = \sqrt{1 - \left(\frac{\sin \Phi_0}{n_1} \right)^2}, \tag{3.12}$$

$$\cos \Phi_2 = \sqrt{1 - \left(\frac{\sin \Phi_0}{n_2} \right)^2}. \tag{3.13}$$

For the overall transmitted amplitude an elliptic equation derivation is given in [AB77]. For it, a representation of the measurable angles of the optical components through the elliptic angle Ψ and phase Δ is used and the ratio of the complex reflected amplitudes is

$$\rho_s = \frac{|R_p|}{|R_s|} = \tan \Psi e^{i\Delta} \tag{3.14}$$

with

$$\tan \Psi = \frac{R_p}{R_s} \tag{3.15}$$

and

$$\Delta = \Delta_p - \Delta_s, \tag{3.16}$$

where $|R_{p,s}|$ and $\Delta_{p,s}$ are absolute values and complex phases of the reflection amplitudes.

For an ordinary PCSA arrangement the measured intensity is [AB77]

$$I \propto |R_p \cos A\,[\cos C \cos(P-C) + i \sin C \sin(P-C)] + R_s \sin A\,[\sin C \cos(P-C) + i \cos C \sin(P-C)]\,|^2, \tag{3.17}$$

where P, C and A are the azimuthal angles of the polarizer, compensator and analyzer measured in the counter-clockwise direction against the plane of incidence.

In the null-ellipsometry method a combination of the components' angles is chosen for which the intensity I vanishes ($I \to 0$). In such a case from the equations (3.14) and (3.17) one obtains

$$\rho_s = \frac{|R_p|}{|R_s|} = -\tan A \frac{\tan C - i \tan(P-C)}{1 + i \tan C \tan(P-C)}. \tag{3.18}$$

In the usual PCSA ellipsometry (referred to further as PA-ellipsometry), where the polarizer and the analyzer are rotatable, the compensator is normally set to $C = \pm\frac{\pi}{4}$. Applying the addition theorem $\frac{1-i\tan\theta}{1+i\tan\theta} = e^{-i2\theta}$, one obtains

$$\rho_s = \mp \tan A e^{\mp 2i(P \mp \frac{\pi}{4})} \text{ for } C = \pm\frac{\pi}{4}. \tag{3.19}$$

Use of this variant for the CKrS was discussed in [Ost09], [Weg10], [Spi11].

As has been shown in [Bau+13], a null-ellipsometry variant where the analyzer is fixed and the compensator and the polarizer are rotatable is possible. The position of the intensity minimum is expressed in this case in P and C angles (therefore, this variant will be referred to as PC-ellipsometry). The equation (3.19) is no longer valid in this case, however, ρ_s (as any complex number) can be expressed by two angles $\tilde{P}, \tilde{A} \in [0, \pi[$ (in analogy with the Euler's representation) as

$$\rho_s = \tan \tilde{A} \cdot e^{i2(\tilde{P} + \frac{\pi}{4})} \tag{3.20}$$

so the P and C coordinates can be translated via the relation (3.18) into the corresponding $\tilde{P}$ and $\tilde{A}$ angles (which would be measured in a standard PA-ellipsometry set-up with $C = -\frac{\pi}{4}$ for the same sample) using

$$\tan \tilde{A} \cdot e^{i2(\tilde{P} + \frac{\pi}{4})} = \rho_s = -\tan A \frac{\tan C - i \tan(P-C)}{1 + i \tan C \tan(P-C)}. \tag{3.21}$$

Therefore, the same analysis means as in the case of the PA-ellipsometry can be used to work with data from the actual CKrS ellipsometry set-up.

3.3.3 Measurement and analysis of the ellipsometry data

An on-line minimum search and PC-scanning procedure is integrated into the CKrS LabView software. It performs an approximate minimum position search iteratively and then scans a region around it with a user-defined size (*e.g.* $\pm 5°$) and step size (*e.g.* $1°$). To find accurate coordinates of the minimum, an off-line Minuit fit with a 2D-paraboloid is done:

$$I = K + \frac{[\cos\theta \cdot \Delta P + \sin\theta \cdot \Delta C]^2}{a^2} + \frac{[-\sin\theta \cdot \Delta P + \cos\theta \cdot \Delta C]^2}{b^2}, \tag{3.22}$$

where K is an offset, θ is a rotation angle of the paraboloid, $\Delta P(\Delta C)$ is a difference between a measured polarizer (compensator) angle and a $P(C)$-coordinate of the minimum and a and b are curvature-defining constants. An example of such a scan together with the fit result is shown in fig. 3.9.

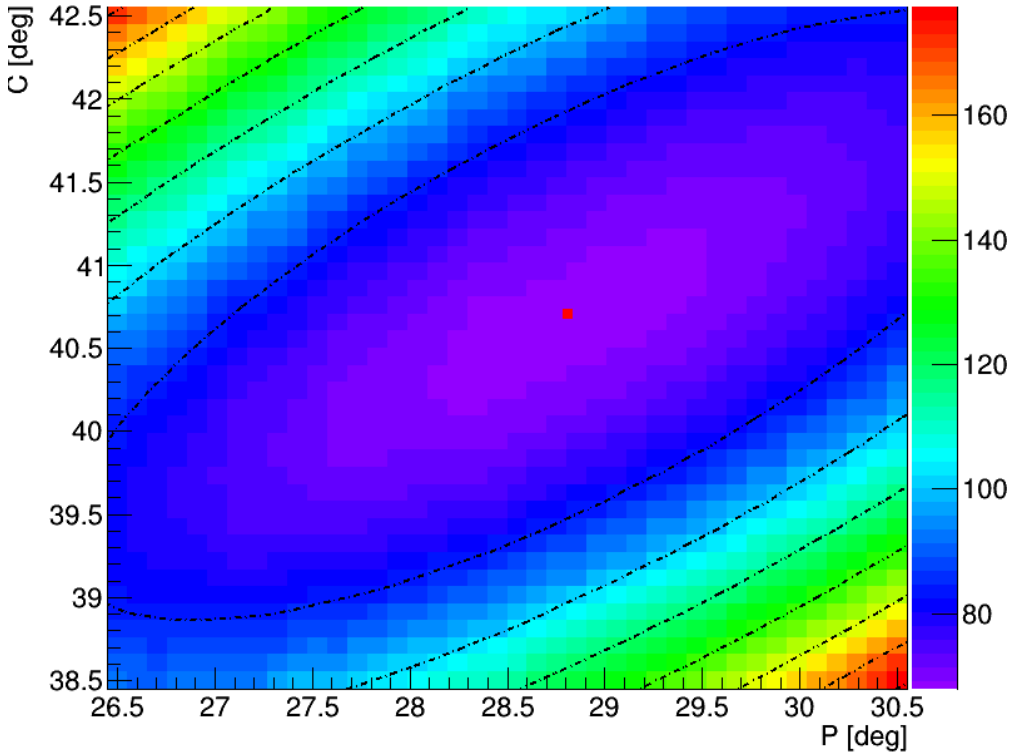

Figure 3.9: Example of a PC-scan around an intensity minimum of the light reflected from a krypton film and a 2D-paraboloid fit (dashed lines). The color scale denotes intensity in arbitrary units and the red dot indicates the minimum determined by the fit.

During measurements, while freezing radioactive krypton, the minimum coordinates are constantly observed. In ideal vacuum conditions, no shift of the null position would be observed since the amount of ^{83m}Kr which we are freezing is too small: for a typical ^{83}Rb activity at the source of $\dot{N}$ =5 MBq, the speed of ^{83m}Kr film growth on the substrate area S =4 cm^2 (assuming a monolayer thickness h to be equal to a krypton crystal constant of 5.59 Å) would be

$$\dot{d} = \dot{N} \cdot \frac{h^3}{S} = 5\text{MBq} \cdot \frac{(5.59\text{Å})^3}{4\text{cm}^2} = 8.7 \cdot 10^{-8} \frac{\text{Å}}{\text{s}}, \tag{3.23}$$

which corresponds to 1 Å (which is on the verge of resolution of the method) in 3193 h if all produced krypton would freeze on the substrate. Therefore, if a shift of the minimum position is observed during measurements (which typically take from a few hours to a few hundred hours) it means that along with ^{83m}Kr some residual gas is condensing.

A krypton reference curve delineated by the minimum position $(\tilde{P} - \tilde{P}_0, \tilde{A} - \tilde{A}_0)$ with film growth is measured by freezing several hundreds of nm of stable krypton. Optical parameters of the film can be obtained by fitting the data with a calculated theoretical curve $(P - P_0, A - A_0)$ by

minimizing the total distance between them[2]:

$$\chi^2 = \sum_i \chi_i^2 = \sum_i \frac{\left[\left(\tilde{P}_i^d - \tilde{P}_0^d\right) - \left(P_i^f - P_0^f\right)\right]^2 + \left[\left(\tilde{A}_i^d - \tilde{A}_0^d\right) - \left(A_i^f - A_0^f\right)\right]^2}{\sigma_{\tilde{P},i}^2 + \sigma_{\tilde{A},i}^2}, \tag{3.24}$$

where "d" index stands for "data" and "f" for "fit". For the fit, the optical parameters of the film and substrate (n_1, n_2, k_2) are varied, as well as the incidence angle Φ_0, the angle of analyzer A and the correction angles of the rotatable polarizer and compensator which emerge due to mutual tilt of the optical components and the offsets of the polarizer and compensator w.r.t. the scales of their holders. For each variation the ratio ρ_S of the two reflection coefficients was calculated (eq. (3.18)) in 1 Å steps. The absorption coefficient k_1 has been fixed to zero, as no absorption of the laser light is expected in the krypton films. For the former CKrS set-up used in [Bau+13] the polarizer and compensator correction angles were measured in [Gre13]. This was not measured for the current CKrS set-up in the frame of this work due to the much more complicated optical set-up, except for the offsets of the scales of the polarizer and the compensator (see Appendix B).

[2]Here, we are using relative coordinates by subtracting from the fitted and measured curves their starting points, (P_0, A_0) and $(\tilde{P}_0, \tilde{A}_0)$ respectively

3.4 Ellipsometry of the CKrS films in krypton measurement phases of 2017 and 2018

The CKrS set-up was built and tested in Münster and transported to Karlsruhe Tritium Laboratory (TLK) where it was installed on top of the CPS in 2017. In the same year it was commissioned [Are+18b]. In the following subsections, ellipsometry measurements and analysis of the condensed krypton films used in the measurements of 2017 and 2018 are presented.

3.4.1 Krypton campaign 2017

The first commissioning measurement with the CKrS *in situ* was conducted in July 2017 [Dyb18]. During the campaign, 3 radioactive films were prepared and used for repeated measurements of spectral lines. As was mentioned in the previous section, a film preparation starts with a cleaning of the substrate with heating and ablation and, after that, the valve to the Rb generator is opened to let radioactive Kr diffuse through the capillary to the cold substrate. Since the diffusion process is relatively slow, it takes about 12 hours until the activity of the condensed ^{83m}Kr saturates [Dyb18] and stable rates of conversion electrons are supplied by the CKrS. Therefore, the first hours from the beginning of the first film preparation must be rejected in the spectroscopy analysis. For the subsequent films in the same measurement phase this stabilization process is not relevant anymore since the capillary is already filled with krypton. Figure 3.10 shows exemplary of the integral spectrum of the K32-$M_{2/3}$ lines taken with the main spectrometer together with the result of a model fit.

In parallel to spectroscopic measurements, ellipsometry data for each of them were taken and are shown in fig. 3.11 (squares - first film, triangles - second film, diamonds - third film). The PC-coordinates of the intensity minima of light reflected by the substrate shift with time, which indicates freezing of residual gas along with the ^{83m}Kr. Each new film starts "earlier" with respect to the direction of the film growth, which indicates that subsequent cleaning procedure removes more and more contaminations from the substrate. For illustrative reasons, fig. 3.12 presents polarizer and compensator coordinates of the intensity minima as a function of time. As can be seen for both coordinates the slope for each new film becomes flatter, which means that the layer growth speed decreases, indicating an improvement of vacuum conditions in the CKrS system with time.

Direct fits of ellipsometry data for the films do not give consistent values of the optical parameters explained in section 3.3.3. The obtained values of film refractive index are consistent neither with krypton values from literature (see table. 3.2), nor with water (which is assumed to be the main component of the freezing residual gas in our system) at this temperature - 1.30 ± 0.02 [WBB98]. This can be explained by the fact that the parts of the measured ellipsometry curves are too small and can be described by a lot of different parameter combinations [Weg10]. Instead, therefore, we compare the ellipsometry data of the radioactive films to the fit of a stable Krypton reference measurement combined with a point from a clean substrate measurement at room temperature (fig. 3.13). The reference measurement was done by first opening the voltage-driven precision valve V9 (see section 3.2.3, fig. 3.4) at 0 V for ∼25 min to insert stable krypton from mixing chamber while continuously taking ellipsometry data and afterwards by using an automated repeated procedure: 1) opening the voltage-driven precision valve V9 at 0 V for 5 min, 2) closing valve V9 and wait 5 min for

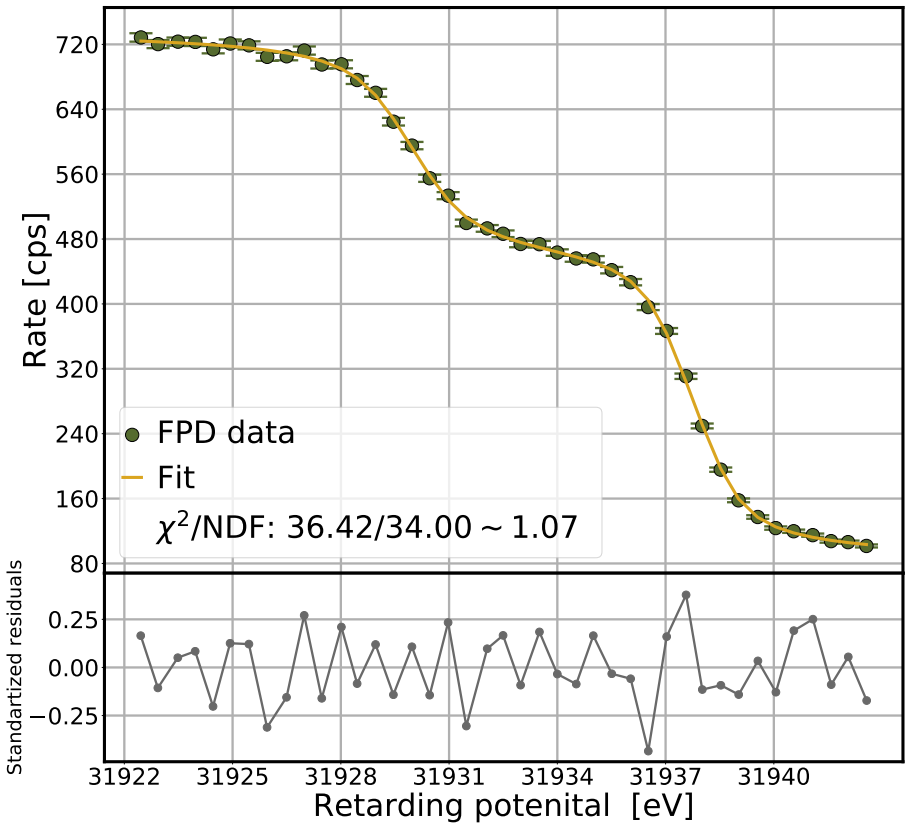

Figure 3.10: An exemplary integral spectrum of $M_{2/3} - 32$ lines measured with CKrS (green dots) and fit (yellow line).

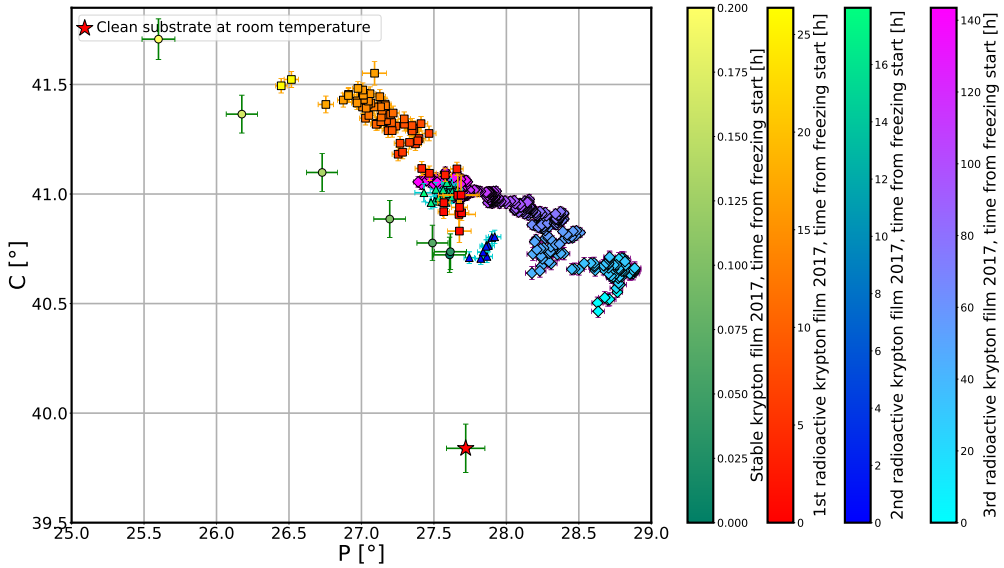

Figure 3.11: Intensity minima position drift for three radioactive films (squares - first film, triangles - second film, diamonds - third film) and the first part of the stable krypton reference measurement (dots) of Krypton 2017 campaign. All errorbars are increased by a factor 10 for the sake of clarity.

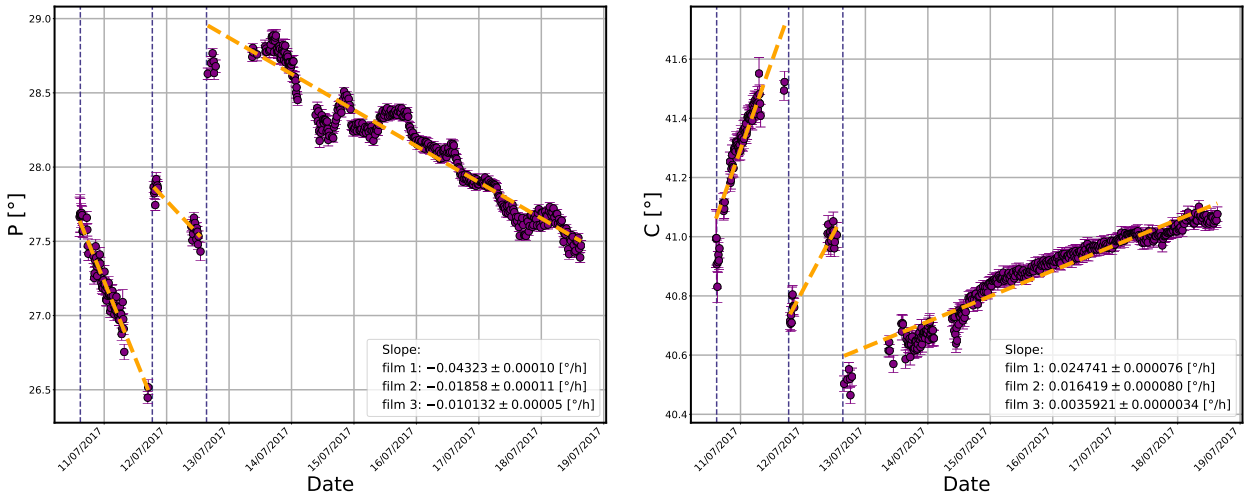

a b

Figure 3.12: Polarizer (a) and compensator (b) coordinates of the intensity minima over time for three films of the Krypton 2017 campaign (vertical dashed lines indicate the time of film preparation). Errorbars are increased by a factor 10 for the sake of clarity.

krypton to freeze on the HOPG and 3) perform an ellipsometry scan. The measurement was done over about 12 h (the complete measurement is seen on fig. 3.13; the first part of the measurement is shown on in fig. 3.11 (dots) together with the data for the radioactive films). The comparison of the ellipsometry data of the radioactive films to the stable krypton reference measurement allows to approximately evaluate the thickness of the frozen layers since the obtained optical parameters of the film and the substrate agree with the literature values and are close to those measured in [Bau+13], see tables 3.2 and 3.3.

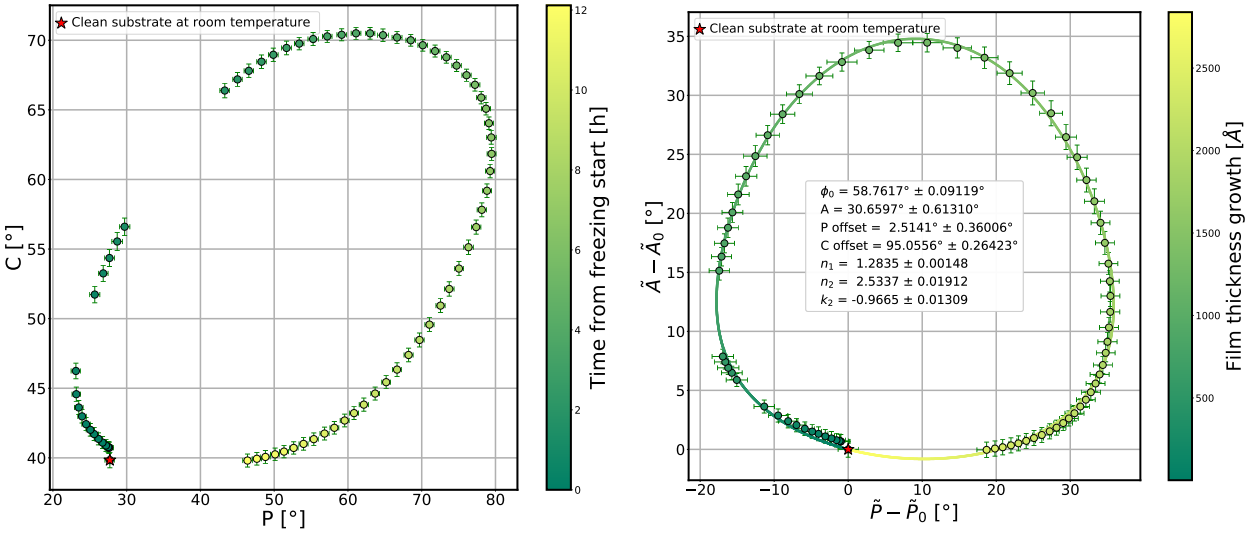

a b

Figure 3.13: (a): Measured ellipsometry minima position in PC-plane during continuous stable krypton freezing in 2017 (errorbars are increased by a factor of 50 for the sake of clarity); (b) corresponding fit and minima positions in $(\tilde{P} - \tilde{P}_0)(\tilde{A} - \tilde{A}_0)$-coordinates (errorbars are increased by a factor 5 for the sake of clarity).

For the condensed films, a linear growth over time is assumed, therefore the obtained dependencies

n_1	Source
1.28	[KA59]
1.282 ± 0.008	[Bau+13]
1.2835 ± 0.0015	this work (stable krypton 2017)

Table 3.2: Comparison of $N_1 = n_1$ values of quench-condensed krypton films from literature and the present work (adaptation from [Bau14]).

n_2	k_2	Source
2.73	1.40	at 633 nm [GRE+69]
2.52	1.94	at 546 nm [JHL07]
2.61	0.57	at 633 nm [TP65]
2.55	0.66	at 633 nm [BKE70]
2.15	0.66	at 541 nm [Erg67]
2.645 ± 0.030	0.964 ± 0.037	at 543.5 nm [Bau+13]
2.533 ± 0.019	0.967 ± 0.013	at 532 nm this work (stable krypton 2017)

Table 3.3: Comparison of n_2 and k_2 values from literature and the present work (adaptation from [Bau14]).

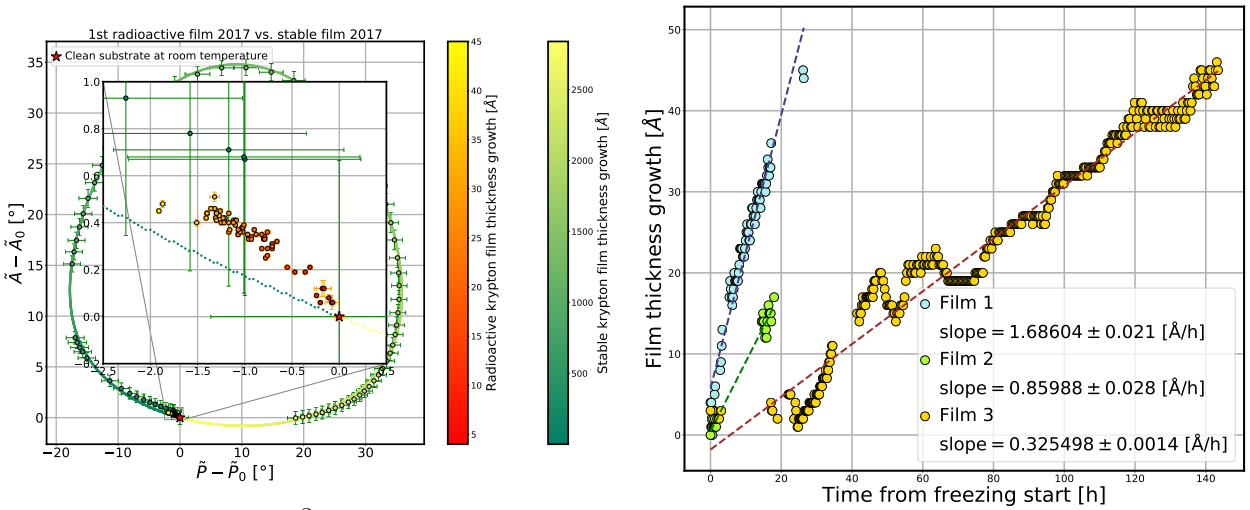

Figure 3.14: (a) - comparison of ellipsometry data of the stable and first radioactive krypton film together with fit curve to stable krypton data of 2017 campaign in in $(\tilde{P} - \tilde{P}_0)(\tilde{A} - \tilde{A}_0)$-coordinates (errorbars of data points are increased by a factor 5 for the sake of clarity); (b) - thickness growth of the three radioactive films over time calculated from the comparison to the fit curve of the stable krypton measurement of 2017.

of the film thicknesses over time are fitted with a linear function which allows to estimate the speed of film growth as seen on fig. 3.14b. To estimate the uncertainty of the film thickness determination with the method, an RSME (root mean square error) for the third film (since this one exhibits the largest deviations wrt. its fit line due to unknown systematic effects) is calculated. This gives a conservative estimation for the uncertainty of about ±2.4Å.

The fact of the freezing residual gas and growing condensed film reflects itself in spectroscopy measurements as well. In fig. 3.15 the measured K32-M_3 krypton line position for all three films is presented. As can be seen, the line position moves to lower energies over time. This drift is attributed to the so called image-charge effect: when a krypton atom decays on the conducting surface of the HOPG, the krypton ion which is left behind induces a mirror charge of an opposite sign in the HOPG. This mirror charge makes a bound system with the ion and decreases the

Coulomb potential which the electron has to overcome. As the film grows, the distance between the ion and the image charge increases and the energy of the bound system decreases, and therefore the electron energy decreases, asymptotically approaching the natural line position. Comparing the data for second and third film one sees that the third film starts with a larger line shift which is in agreement with the observation in the ellipsometry data that the substrate becomes cleaner. A detailed discussion of spectroscopic analysis and image-charge model will be given in [Ful19].

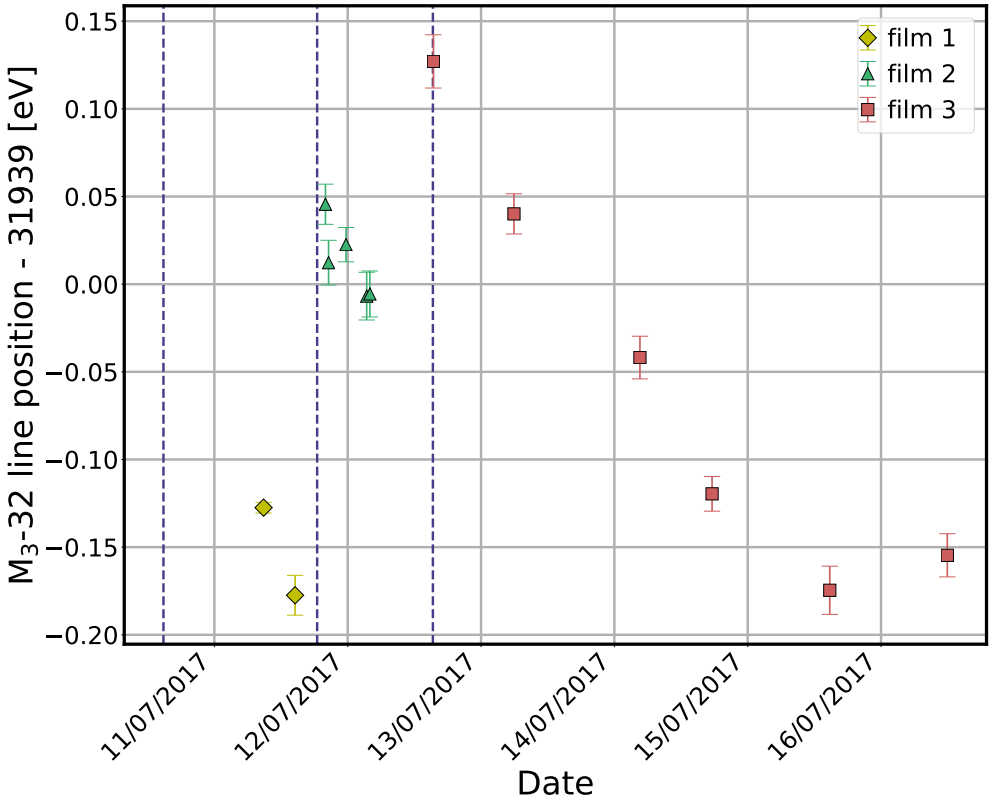

Figure 3.15: Energetic drift of the $M_{2/3} - 32$ line for three radioactive films measured in 2017; dashed lines indicate the time of film preparation. (Adapted from [Ful19]).

3.4.2 Krypton campaign 2018

Since the line position drift observed during the measurement campaign in 2017 complicates the analysis of the transmission function and calibration data, two ways to stabilize the line position were applied during the next CKrS measurement phase in the summer 2018. First, the vacuum system of CKrS was thoroughly baked out to reduce the amount of residual gas in the system, with the aim to decrease the film growth speed due to its deposition. Secondly, an idea to pre-plate the substrate with a layer of stable krypton to reduce the line position shift induced by the image-charge effect right from the beginning was tested.

As in the previous phase, an ellipsometry reference measurement with stable krypton freezing was taken[3]. The measurement was done using an automated repeated procedure for freezing stable krypton: 1) Opening the voltage-driven precision valve V9 (see section 3.2.3, fig. 3.4) for 2 min 20 s to insert stable krypton from the mixing chamber, 2) closing valve V9 and wait 10 min for krypton to freeze on the HOPG and 3) perform an ellipsometry scan[4]. After the measurement was done, it was found out that the automatic operation of the valve V9 did not work properly all the time due to problems in the software (which were fixed afterwards): sometimes the valve stayed opened all the time until the next scan cycle. This caused bigger steps in the curve which can be seen in fig. 3.16. It can be seen that the curve is not closed but spirals inwards instead, which is due to a small non-zero imaginary part of the refractive index of the film k_1 [Weg10]. The fitted value of the film refractive index in this case is lower ($n_1 = 1.265$) than even those measured for quench-condensed krypton films in the other works (see table 3.2) and, according to Clausius-Mosotti relation

$$\frac{N_1^2 - 1}{N_1^2 + 2} = \frac{n_1^2 - 1}{n_1^2 + 2} = \frac{4\pi}{3}\alpha_{\mathrm{pol}}\frac{N_A}{M}\rho_{\mathrm{kr}} \tag{3.25}$$

gives the density of the film $\rho_{\mathrm{kr}} = 2.236$ which is 6% lower than measured in [Bau+13] which can be due to a higher film porosity due to a too fast krypton deposition in this case. This makes the data not suitable for analysis of the radioactive films. Fig. 3.16 shows a comparison of the data to the stable krypton measurement of 2017: the existing data points lie close to each other except for the group of points in the upper part of the plot which stem from the second turn of the ellipsometry curve at very high film thicknesses. Therefore, for the analysis of the radioactive films data the fit of the 2017 stable krypton data was used.

Unfortunately, it was not possible to take ellipsometry data for the radioactive films continuously during the 2018 campaign: the ellipsometry signal was disappearing after some time when the CKrS was positioned inside the beamline. The reason for that appeared to be a bad contact at the photodiode detector which opened up at the lower temperatures inside the CPS and may have been caused by the bake-out. The temperature difference of the diode between the CKrS vacuum chamber and the CPS is about 35 K. Since it was only possible to exchange the photodiode after the measurement phase was complete, as that requires opening of the vacuum system, the problem persisted for all the measurements and the ellipsometry monitoring was only possible when the CKrS was positioned outside the flux tube.

[3] after the actual measurement campaign.

[4] An opening of the V9 valve at a certain voltage here is not equivalent to that in 2017 measurements, since the valve opening has been readjusted manually in-between the measurement phases.

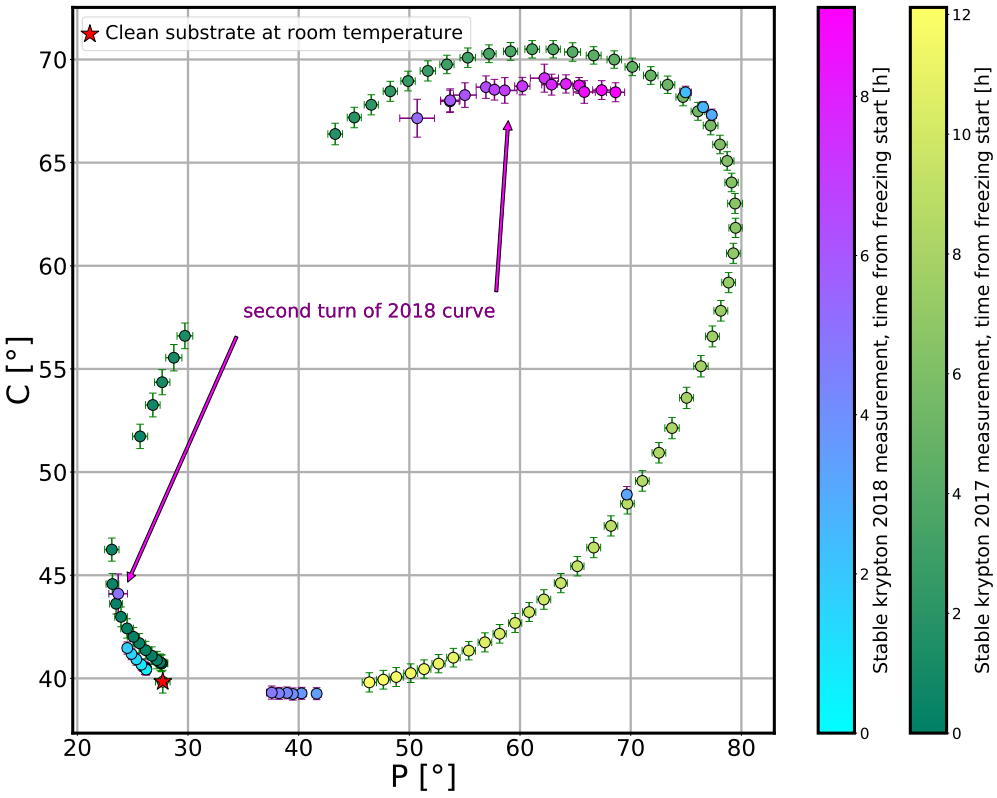

Figure 3.16: Comparison of ellipsometry data for stable krypton measurements in 2017 and 2018. All errorbars are increased by the factor of 50 for the sake of clarity.

During the campaign it was first tested how reduction of the amount of residual gas by the system bake-out affected stability of the films. For this, a film without pre-plating (freezing radioactive krypton directly onto the substrate) was prepared[5] and measured. Fig 3.17 shows the polarizer and compensator ellipsometry minimum coordinates as function of time for the first film (no ellipsometry data are provided for the second film due to the photodiode issue). A slower drift is expected due to improvement of vacuum conditions, however, the slope of the 2018 film turned out to be smaller than that of the first film of 2017 but between the second and third film of 2017.

As can be seen in fig. 3.21 (left two films) the line position drift did not improve much and is on the same order as in 2017. Moreover, the offset of the second film start is about the same as for the first film end which may point to an inefficient cleaning of the substrate. Since the amount of residual gas in the system after bake-out was still large enough to result in an intolerable drift of the line position (the change in the minimum position of ∼350 meV in 85 h of measurements for both films in total), pre-plating of the substrate with a layer of stable krypton was tested next.

An objective of this experiment, apart from investigating whether pre-plating improves the line stability, was to find a preparation procedure for films with stable krypton pre-plating and to test its reproducibility. Ellipsometry data for all of the pre-plated films discussed below is shown in fig.3.19.

For the first film, a 8 V opening of the precision valve V9 for 5 min have been tried out; the corresponding ellipsometry data are shown in fig. 3.19 (squares). As can be seen in fig. 3.20 (green dots) this caused a film growth of about ∼10 nm. However, the observed drift in the line position for this film (fig. 3.21, rombs) was intolerably high: about 100 meV in 40 h.

[5] the capillary has been filled with radioactive krypton in advance for this measurement.

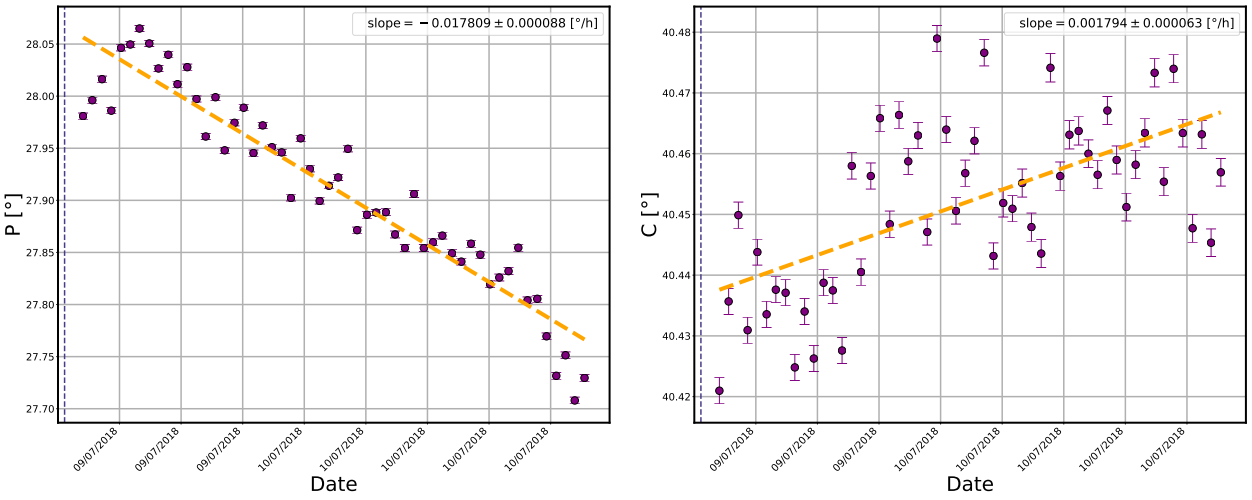

a b

Figure 3.17: Polarizer (a) and compensator (b) coordinates of the ellipsometry intensity minimum over time for the first film without pre-plating of the Krypton 2018 campaign (vertical dashed lines indicate the time of film preparation start).

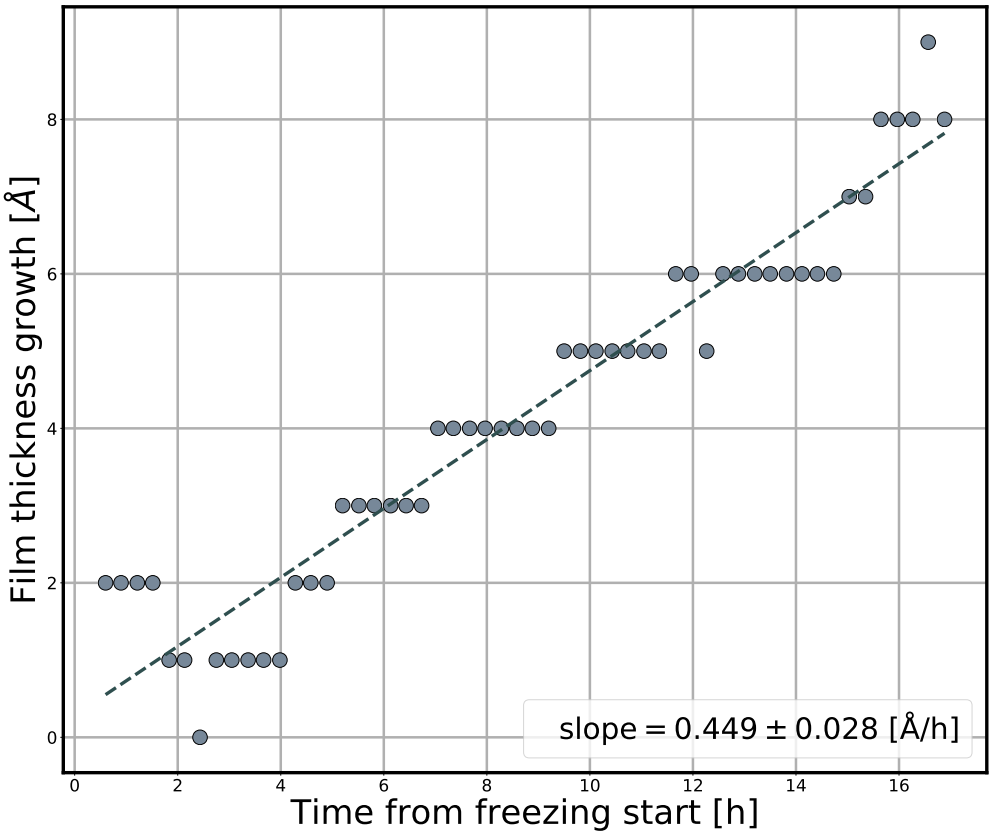

Figure 3.18: Thicknesses of the first radioactive film without pre-plating over time calculated from comparison to the stable krypton fit curve.

The film was subsequently removed and a preparation of a thinner film has been tried. For this the precision valve V9 has been opened at an 8 V setting for 1 min; however, no change in ellipsometry data has been observed. Therefore the opening time has been prolonged to 2 min 20 s which allowed to condense a thin layer of about 1 nm, see fig. 3.19 (triangles) and fig. 3.20 (blue

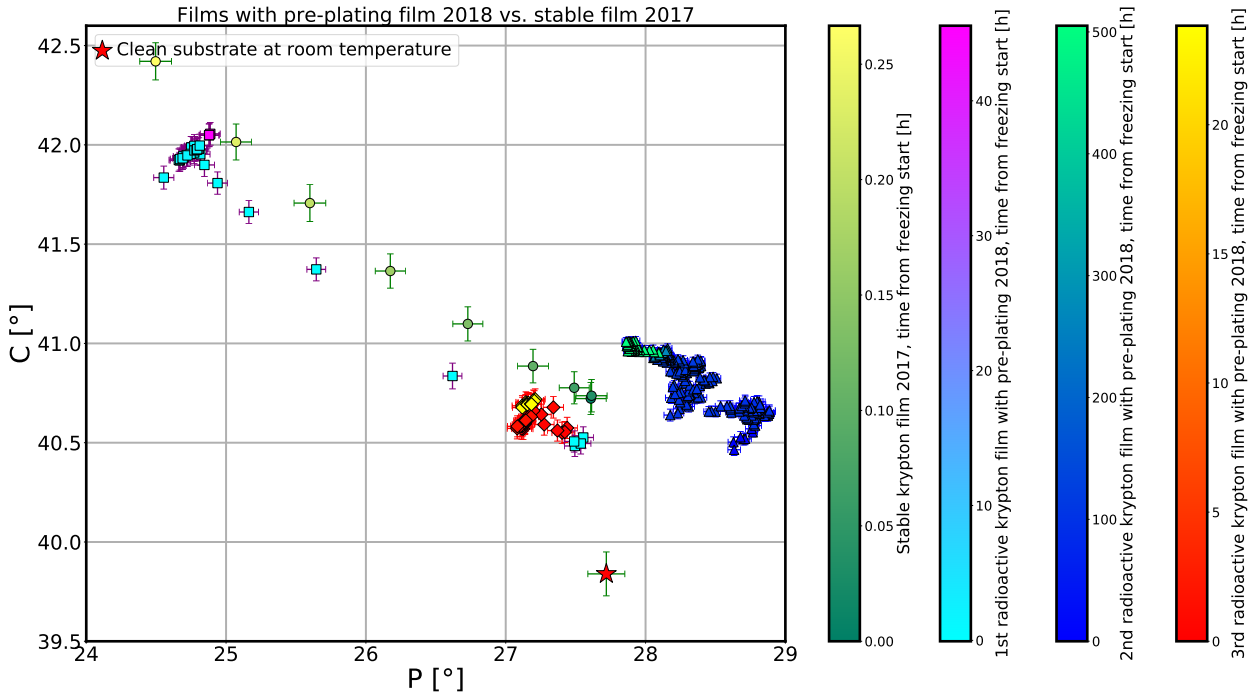

Figure 3.19: Intensity minima position drift for three radioactive films with pre-plating of Krypton 2018 campaign (squares - first film, triangles - second film, diamonds - third film) and the first part of the stable krypton reference measurement (dots) of Krypton 2017 campaign. All errorbars are increased by the factor of 10 for the sake of clarity.

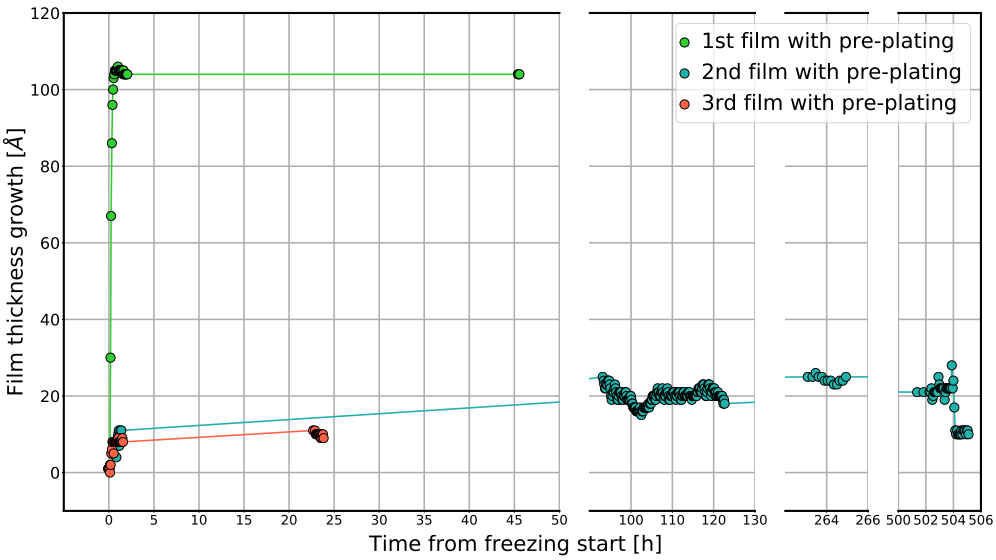

Figure 3.20: Thicknesses of radioactive films with pre-plating over time calculated from comparison to the stable krypton fit curve.

dots).

As can be seen in fig. 3.21 (circles), this allowed to achieve a stability of 30 meV over about 100 h sufficient for calibration measurements. After first measurements with this film, the CKrS was retracted from the CPS for a measurement break. For this film, a comparison of the ellipsometry and spectroscopy data is shown separately in fig. 3.22. A stable line position has been achieved before and after the measurement break. A slight drop in thickness seen in ellipsometry data and

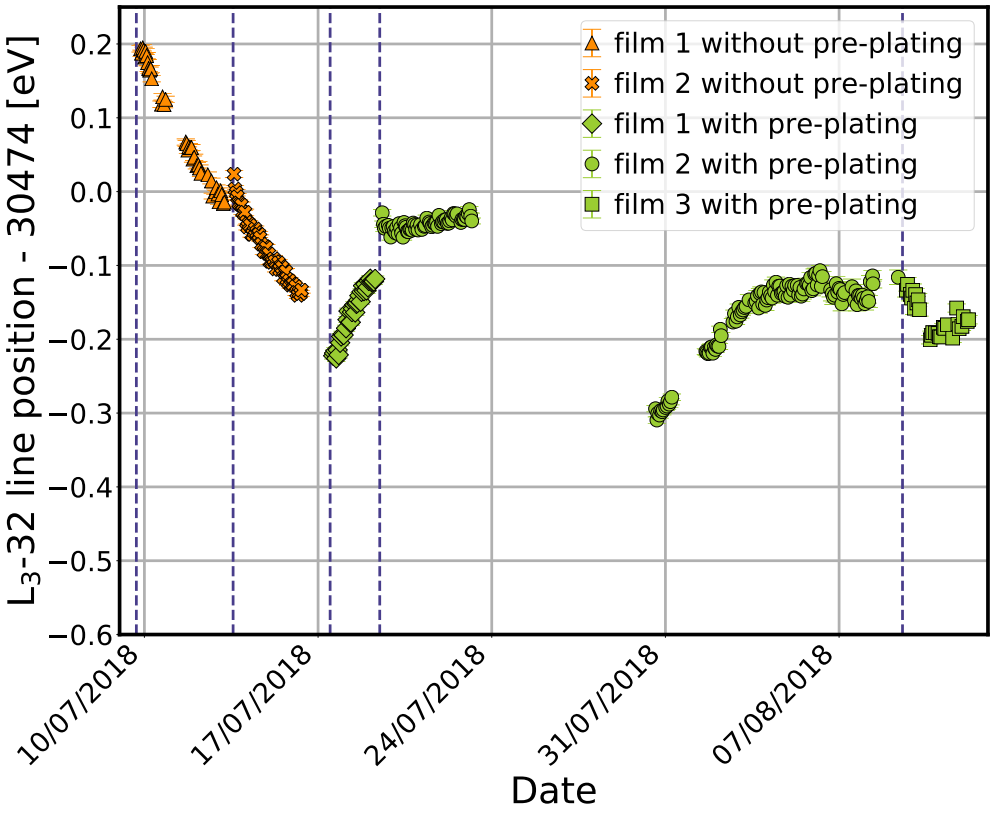

Figure 3.21: Position drift of L_3-32 line for two radioactive films without (orange dots) and three ones with (green dots) pre-plating of 2018 (vertical dashed lines indicate the time of film preparation). (Adaptation from [Ful19].)

corresponding line shift after extraction of the source from the flux tube may be due to the warmer environment above the CPS and, as consequence, evaporation of part of the film[6].

To check whether such a film can be reproduced for future measurements, the substrate has undergone the cleaning procedure again and the same preparation procedure (8 V valve V9 opening for 2 min 20 s) has been applied. As can be seen in fig. 3.20 (red dots), the build-up of the pre-plating layer could be reproduced. However, the *PC*-data (fig.3.19, rombs) as well as the line position (fig. 3.21, squares) indicate, that the layer was frozen on top of the part of the old film because the cleaning did not work effectively. This has not been an issue during the measurements in 2017 and may be connected to a misalignment of the ablation laser due to its temporary removal for the bake-out before the 2018 campaign. For the future measurements, the film ablation procedure has to be investigated to ensure proper cleaning of the substrate.

[6]The diretion of the line position drift after the source was re-inserted before stabilization, as well as for the first film with pre-plating, is at the moment not well understood and will be investigated elsewhere [Ful19]

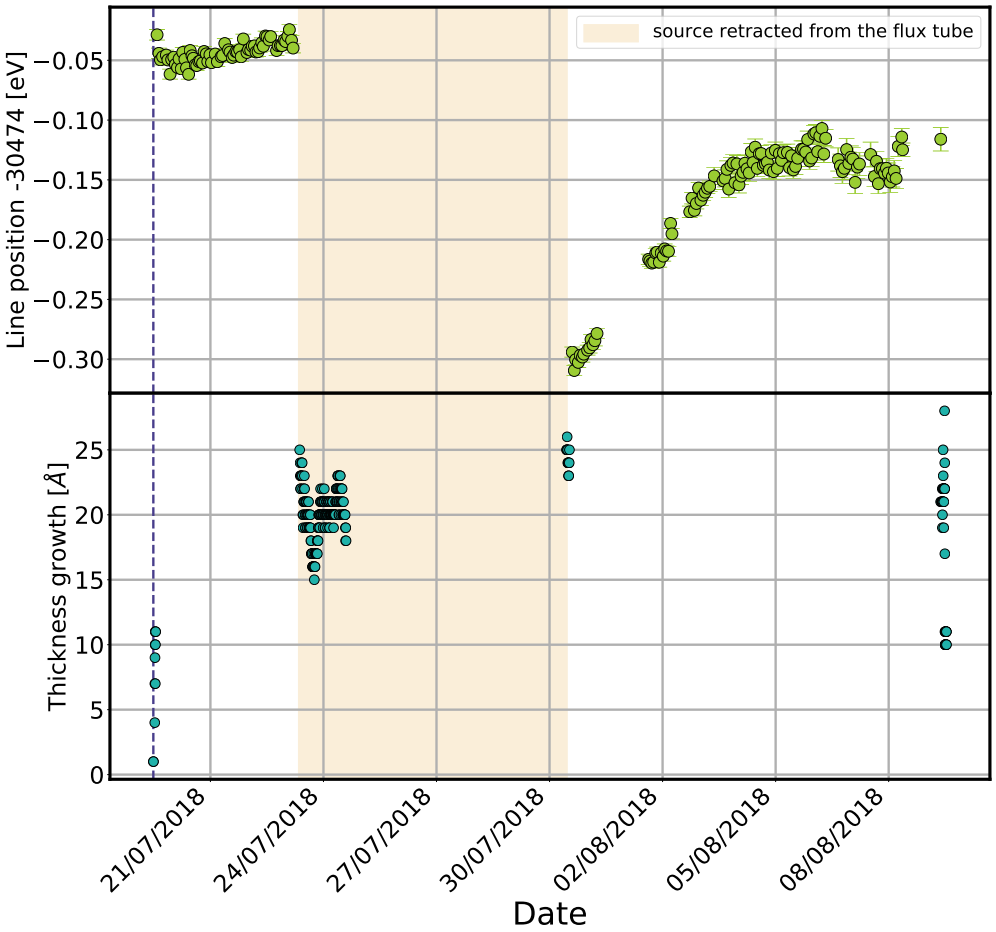

Figure 3.22: Energetic drift of L_3-32 line (green dots, adapted from [Ful19]) and film thickness (blue dots) for the second radioactive film with pre-plating of 2018 .

Chapter 4

Suppression of the inter-spectrometer Penning trap background

As has been stated in the section 2.5.2, to reach the proposed sensitivity in KATRIN, the experimental background must be kept low, with a total rate less than 10 mcps. One of the serious background sources in the experiment is a Penning trap between pre- and main spectrometers, which is discussed in this chapter.

The content of this chapter is almost a verbatim quotation of a major part of arxiv:1911.09633 e-print [Ake+19b] of which I am the main and corresponding author and which I submitted for publication to European Physics Journal C (EPJ C). The measurements presented here were planned, performed and discussed by F. Fränkle, L. Kippenbrock, P. C.-O. Ranitzsch and myself. The data analysis and interpretation of the results of the tests of the Penning trap behavior at different conditions presented here are done by myself; simulations and spectral analysis of the Penning trap background have been performed by L. Kippenbrock and are described in his PhD thesis [Kip19]. The work has been enriched significantly through additional discussions with C. Weinheimer, F. Glück, D. Parno and V. Hannen from the KATRIN collaboration. Technical and electrical design of the electron catchers described in this chapter has been done by H.-W. Ortjohann and R. Berendes (University of Münster) correspondingly.

4.1 Inter-spectrometer Penning trap problem and counteraction

β-electrons inside the main-spectrometer can produce secondary electrons via a chain of processes, which are discussed below. Those low-energy electrons can then be accelerated towards the detector by the electric potential of the main spectrometer to energies around 18.6 keV and hence cannot be distinguished from signal electrons in the endpoint region, raising the overall background level. Therefore, the pre-spectrometer is used to reduce the flux of the β-electrons into the main spectrometer. However, the combination of the retarding potentials of $U_{PS} = -18.3\,\mathrm{kV}$ at the pre-spectrometer and $U_{MS} \approx -18.6\,\mathrm{kV}$ at the main spectrometer and a magnetic field of up to 4.5 T produced by their common superconducting magnet forms a Penning trap for negatively charged particles (see fig. 4.1). An electron passing through this region can lose energy due to processes of elastic and inelastic scattering on rest gas molecules and by synchrotron radiation and become trapped. Several physical processes are connected to the presence of stored electrons in the

inter-spectrometer region:

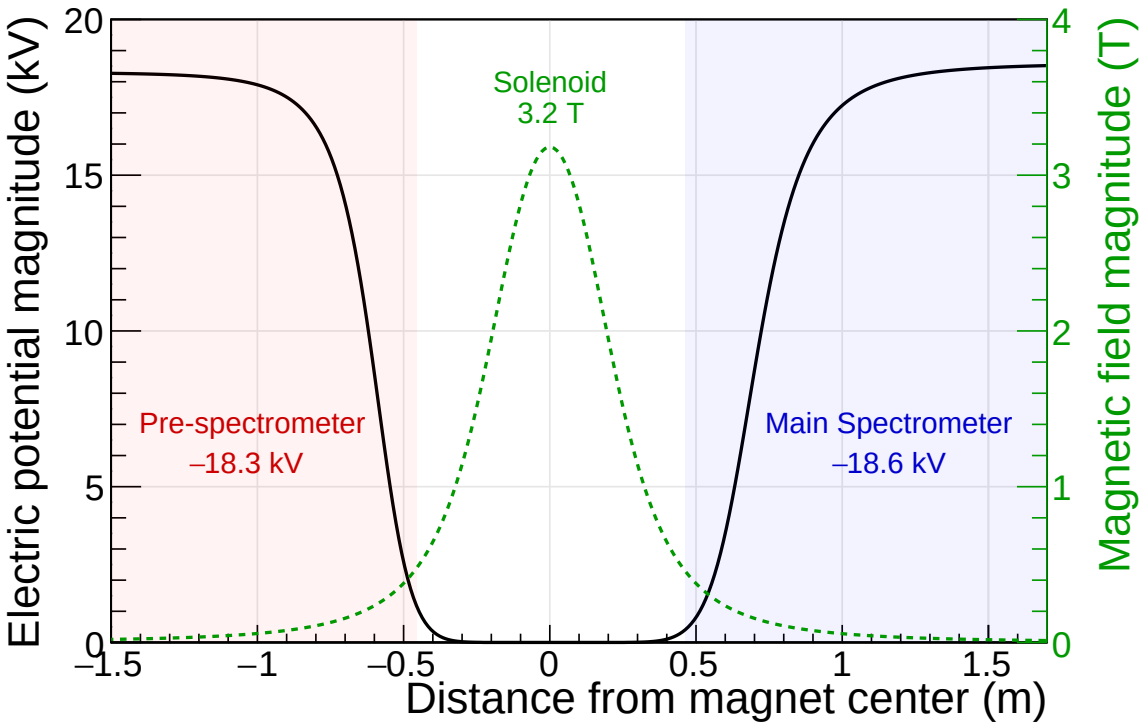

Figure 4.1: Distribution of electric and magnetic fields in the region of the inter-spectrometer Penning trap (from [Ake+19b]).

(a) Electrons stored in the Penning trap lose transverse kinetic energy due to synchrotron radiation. The energy loss

$$E_\perp(t) = E_{\perp 0} \cdot e^{-\Gamma t} \tag{4.1}$$

is characterized by the attenuation factor [KK05]

$$\Gamma = \frac{1}{\tau_{Sy}} = \frac{\dot{E}_\perp}{E_\perp} \approx 0.4 s^{-1} \left(\frac{B}{1\mathrm{T}}\right)^2, \tag{4.2}$$

where B is magnetic field at the electron trajectory and τ_{Sy} is synchrotron cooling time. The exact losses depend on the magnetic field which is not constant throughout the trap volume and the electron's polar angle to the magnetic field lines ϑ. Also, the cooling process through the synchrotron radiation can be enhanced by elastic scattering of the electrons on the residual gas molecules as part of the kinetic energy can be reshuffled into the transverse component thus allowing it to be radiated away.

(b) Due to inelastic scattering with residual gas molecules, additional electrons are created and trapped. There is a significant chance for a trapped primary electron to perform an ionization at the high electric potential at either end of the trap shortly before its return point, because

the maximum of the ionization cross-section $\sigma_e(E)$ $\approx 10^{-20}\,\mathrm{m}^2$ of H_2[1] by electron impact corresponds to electron kinetic energies around 70 eV [Yoo+08a]. In this case a secondary electron, which is trapped as well, can gain enough energy to perform further ionizations itself. The mean time between ionizations at a pressure of $p = 4 \times 10^{-11}$ mbar (or the corresponding particle density of $n(H_2) = 9.7 \times 10^{11}\,\mathrm{m}^{-3}$) and 300 K temperature is estimated for an electron of velocity v using the maximum cross section at $E = 70$ eV as

$$\tau_{\mathrm{ion}} = \frac{1}{\dot{N}_e^{\mathrm{ion}}} = \frac{1}{nv\sigma_e^{\mathrm{ion}}} = \sqrt{\frac{m_e}{2E}}\frac{1}{n\sigma_e^{\mathrm{ion}}} \approx 20\,\mathrm{s}, \tag{4.3}$$

where $\dot{N}_e^{ion}$ is the rate of ionization collisions of a single electron and m_e is the mass of the electron. This can lead to an avalanche process, creating more and more charged particles: according to detailed electron tracking calculations, using electron inelastic and elastic differential scatterings with H_2 molecules (including angular changes) and synchrotron radiation in 4.5 T magnetic field, 1 initial stored electron with $E_0 = 18$ keV starting energy produces $N_{e-i} = 10^8$ ionizations, and this multiplication number is very sensitive to the electron energy: with 10 keV, 5 keV and 1 keV, it is only 40000, 1000 and 20, respectively [Glu08]. With 1×10^{-11} mbar residual gas pressure, the electron cooling time is of the order of 1 h. High numbers of electrons can build up a space charge affecting even signal electrons flying through the Penning trap region.

(c) The ions, created along with the secondary electrons, are not trapped inside the inter-spectrometer Penning trap and can leave towards the spectrometers. There, in the low magnetic field, they move non-adiabatically until they hit the spectrometer vessel, having on their way a minor (but still non-zero) probability to produce background electrons due to scattering inside the spectrometers. The ionization collision cross-section of H^+ and H_2^+ of $E = 18$ keV kinetic energy with H_2 molecules is about $\sigma_{ion} = 10^{-20}\,\mathrm{m}^2$, which for the pressure of $p = 4 \times 10^{-11}$ mbar and a mean ion path length of $l = 24$ m gives the ionization probability of $P_{ion} = \sigma_{ion} \cdot n \cdot l = 2.3 \times 10^{-7}$. This means, that each trapped primary electron of $E_0 = 18$ keV starting energy can result in up to $N_{\mathrm{trap}}^{\mathrm{ionization}} \approx N_{e-i} \cdot P_{ion} = 23$ electrons which can reach the detector.

Apart from ionization of the residual gas, the ions can produce electrons by hitting the metallic surface of the spectrometer walls which are, however, efficiently shielded by the approximately axisymmetric magnetic field and by the wire electrode system of the spectrometer. Assuming again 10^8 electron-ion pairs per primary trapped electron and further assuming 10 electrons are knocked out per ion and lower limit for the suppression factor of 10^4 due to the shielding [Alt+19], there could be up to 10^5 electrons reaching the detector per primary trapped electron by this process.

(d) UV-photons can be created from the de-excitation of residual gas molecules after collision with trapped electrons. These photons, not being affected by electric and magnetic fields, can hit metal surfaces and release more electrons, or, in the extreme ultraviolet case, create

[1] In the KATRIN ultra-high vacuum conditions, most of the residual gas consists of H_2 molecules.

secondary electrons by photoionization off residual gas molecules, potentially leading to the similar background rates as due to the ions.

(e) Another recently found source of background electrons, which was overlooked in the past, is highly excited neutral atoms or molecules, *e.g.* Rydberg atoms, which are produced via several different processes and can propagate freely within the spectrometers. There states can be ionized by the interaction with infrared photons from the black body radiation of the spectrometer vessel (or by auto-ionization if more than one electron of the atom is excited). Such highly excited neutral atoms or molecules can, among others, be created by electrons trapped in the Penning trap scattering on residual gas molecules. When they release electrons in the central region of the main spectrometer, those electrons cannot be distinguished from normal signal electrons.

In consequence, electrons accumulating in the Penning trap between pre- and main spectrometers can lead to elevated background rates much larger than tolerable at the KATRIN experiment, as well as to an exponentially growing avalanche or discharge which may present a danger for the spectrometer and detector section of KATRIN. Not only the former effect is strongly dependent on pressure (as shown in the discussion above), but also the latter: the formative time t_f of a Penning discharge is inversely proportional to the pressure p of the residual gas inside the Penning trap: $t_f \propto 1/p$ [IVA73]. Therefore, the residual pressure in the spectrometers, along with their electric potentials, is a crucial parameter for the inter-spectrometer Penning trap problem.

Since this Penning trap cannot be avoided in a tandem MAC-E-Filter set-up and the filling of the trap by electrons is very difficult to avoid completely, a method to eject stored electrons from the Penning trap before they can ionize residual gas molecules is required. Several ejection processes have been investigated already in the past to achieve an ejection time faster than the ionization time:

$$\tau_{\text{eject}} < \tau_{\text{ion}} \tag{4.4}$$

In the early simulation studies it was shown [Ess04] that electrons stored in the KATRIN inter-spectrometer Penning trap will indeed lead to a cascade of secondary electrons producing a significant amount of background. A possibility to eject stored electrons via $E \times B$ drift by applying a transversal electric field was investigated as well, but this method would require very high electric fields, which would potentially lead to discharge problems. Therefore, a mechanical ejection method was developed and tested [Yoo+08b], [Val09] using the spectrometer of the former Mainz Neutrino Mass Experiment. The investigation showed that a wire sweeping through the Penning trap is able to remove stored electrons and to successfully stop the build-up of background processes. The wire movement was controlled by an electric current through the wire, which subsequently moved in the magnetic field due to the Lorentz force. The ability of the slowly sweeping wire to catch all trapped, but fast moving electrons, is due to the magnetron motion of the trapped electrons which caused them to collide with the wire within a very short time frame (see section 4.2 below). The fact that the magnetron drift is really sufficient to safely remove the electrons stored in the Penning trap even under the conditions at KATRIN was investigated in detail in a test experiment at the KATRIN pre-spectrometer [Hil11]. Here, the principle of the electron catcher in the form of a thin

pin was successfully demonstrated for the first time.

Apart from accumulation and multiplication of electrons, there are possible antagonistic processes inside the inter-spectrometer Penning trap. Additionally to the elastic scattering on residual gas particles mentioned above, stored electrons will have Coulomb interactions with other electrons and with the plasma which can promote larger angular changes and thus stronger synchrotron radiation. Another possible loss mechanism is due to time-dependent non-axisymmetric electric fields of plasma instability, which can result in electrons leaving the trap in radial direction. Also, since each of the spectrometers is an electrostatic and magnetic bottle trap for low-energy positive ions, there is a small overlap of the clouds of electrons and ions (stored inside the inter-spectrometer region and the spectrometers, correspondingly), which can give an additional weak electron-ion recombination contribution. While the rate of elastic scattering on residual gas is directly proportional to its pressure, $\dot{N}_e^{\text{elastic}} = nv\sigma_e^{\text{elastic}}$, the electron-electron scattering, plasma instability and recombination processes are pressure independent. Additionally, for electrons with energies above 90 eV the inelastic cross section is higher than the elastic one [Yoo+08b]. Therefore, as is schematically illustrated in fig. 4.2, the electron loss rate will dominate the ionization rate at low pressures, providing a pressure region where the Penning trap can exist without developing discharges. A periodically moving electron catcher will additionally remove stored electrons and therefore increase the pressure region where the system can be operated safely.

In view of these studies, the interception of trapped electrons with a movable electron catcher was chosen as the most suitable and reliable method. Therefore newly developed electron catchers were implemented inside the magnet bore between the two spectrometers. In the following the successful commissioning of the electron catchers is described during which their effectiveness for elimination of the Penning trap activity has been demonstrated.

4.2 Working principle and technical realisation of the electron catchers

The three electron catchers are made from bend Inconel rods 2 mm in diameter installed at three different positions inside the valve connecting pre- and main spectrometers, see fig. 4.3. Each of the catchers is attached with one end to an individual bellows mounted on the valve housing. This movable connection allows the free end of the catcher to be moved from its parking position into the flux tube. While it is moved in, it traverses the flux tube in a radial direction from its edge up to the center. The catchers are tilted in such a way (7.5 ° with respect to the horizontal axis at fig. 4.3 b) that the amount of detector pixels affected when the catcher is inside the flux tube is minimized.

The principle of electron removal with the installed electron catchers is based on the specifics of electron motion inside the Penning trap. In a classical Penning trap [Bla06], electrons are constrained radially by a homogeneous axial magnetic field and axially by a quadrupole electric field. In a homogeneous magnetic field, an electron moves in a circular motion, called cyclotron motion, around the magnetic field lines with a corresponding cyclotron frequency:

$$\omega_c = \frac{q}{m} B. \tag{4.5}$$

Due to the additional electric field in the Penning trap and due to inhomogeneities of the

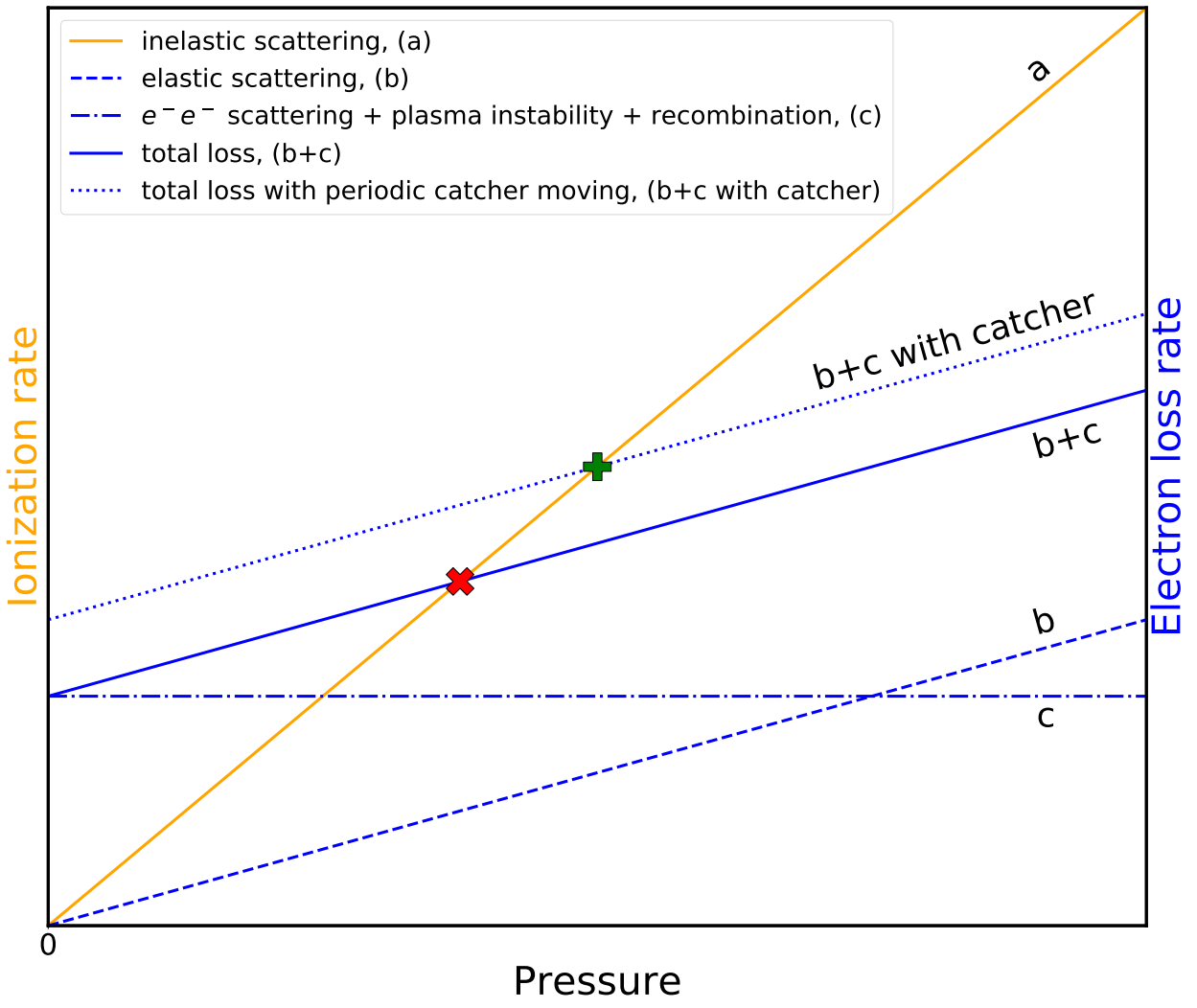

Figure 4.2: A schematic illustration of the ionization rate due to electron inelastic scattering (solid orange line) and the electron loss rate (solid blue line) due to elastic scattering (dashed blue line) and Coulomb interaction together with recombination (dash-dotted blue line). In the pressure region to the left from the crossing point of these two processes (red cross) the electron loss is dominating, which prevents the Penning trap from igniting. A periodic movement of an electron catcher will increase the total electron loss rate shifting the corresponding line upwards (dotted blue line) and shifting the cross point to higher pressures (green plus).

magnetic fields, stored electrons undergo a more complex motion, which can be represented as a superposition of three different components:

- the axial oscillation along the trap axis, independent from the magnetic field, with the frequency

$$\omega_z = \sqrt{\frac{q}{m}\frac{U}{d^2}}, \tag{4.6}$$

where U is called the "trap depth", as particles with an energy lower than qU will not be able to escape the trap. The parameter d describes the trap dimensions, and in the case of a classical Penning trap with hyperbolic electrodes it is

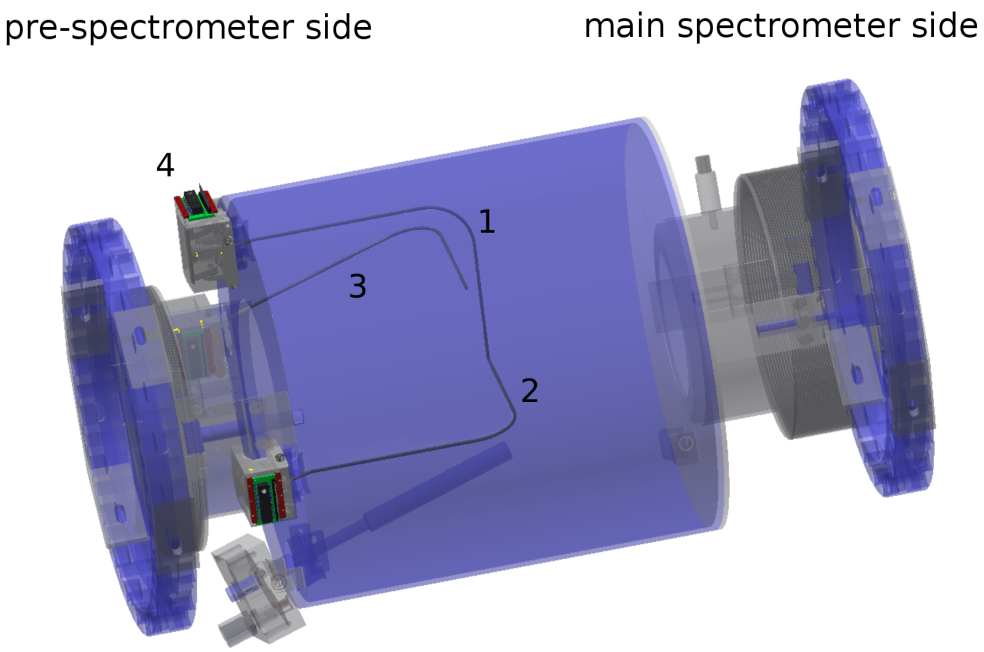

a

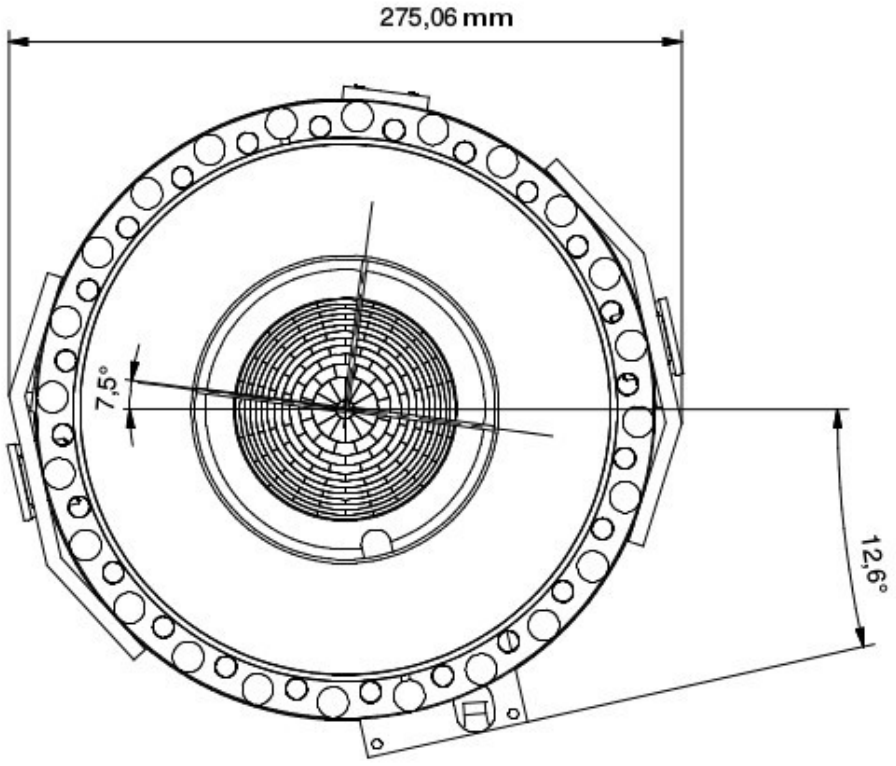

b

Figure 4.3: a: The beam region between the pre- and main spectrometers inside the superconducting spectrometer solenoid. (1), (2), (3) - the electron catchers; (4) - a catcher's controller; b: Technical drawing of the electron catchers against the FPD.

$$d^2 = \frac{1}{2}\left(z_0^2 + \frac{r_0^2}{2}\right), \tag{4.7}$$

where $2z_0$ is the distance between electrodes and r_0 is the trap radius.

- the "modified" cyclotron motion with a frequency slightly different from (4.5) and strongly dependent on the trap depth and dimensions:

$$\omega_+ = \frac{\omega_c}{2} + \sqrt{\frac{\omega_c^2}{4} - \frac{\omega_z^2}{2}} \approx \omega_c - \frac{U}{2d^2B}. \tag{4.8}$$

- the magnetron drift around the trap axis (formula given for a homogeneous magnetic field)

$$\omega_- = \frac{\omega_c}{2} - \sqrt{\frac{\omega_c^2}{4} - \frac{\omega_z^2}{2}} \approx \frac{U}{2d^2B}. \tag{4.9}$$

In the case of the inter-spectrometer Penning trap, which has a length of roughly $2z_0 \approx$1.5 m (see fig. 4.1), a depth of about $U = -18$ kV and a trap radius of $r_0 =$3.6 cm at the center of the solenoid (due to confining of the transported magnetic flux of $\phi =$133.7 Tcm^2 [KK05] by the magnetic field of 3.2 T), corresponding to a dimension parameter of $d \approx$1.1 m (according to (4.7)), the frequencies of the stored electrons are roughly $\omega_z \approx 5 \times 10^7\,\mathrm{s}^{-1}$, $\omega_+ \approx 8 \times 10^{11}\,\mathrm{s}^{-1}$, $\omega_- \approx 2 \times 10^3\,\mathrm{s}^{-1}$. Due to the magnetron motion which is slow with respect to the axial and cyclotron components but still fast compared to the sub-second-scale mechanical movement of the catcher, an electron stored somewhere inside the trap will eventually reach the electron catcher. Faster axial motion will lead to "gaps" along the circumference of the electron's magnetron motion, but the size of the gaps is much smaller than the diameter of the electron catchers preventing the trapped electron from escaping (see fig. 4.4). The catchers are designed such that when one of them is inserted into the flux tube its free end reaches the center of the flux tube. This guarantees that all stored electrons will in the end be removed by hitting a catcher inserted into the flux tube. Since, as has been discussed above, at 10^{-11} mbar pressure the time interval between ionizations in the Penning trap is of the order of tens of seconds and the electron cooling time is of the order of 1 h, which is much larger compared to the sub-ms scale of the magnetron motion, the catcher is able to stop the electron multiplication process and effectively suppress the corresponding background.

A schematic illustration of the combined set-up used to operate a single electron catcher is shown in fig. 4.5. The system is working in a triggering mode: a TTL signal is created by a pulse generator Agilent 33220A and is converted at the signal processing stage to a 24 V signal. As long as the signal stays at this level the valve to the pneumatic muscle is closed, the muscle is relaxed and the catcher remains outside the flux tube. When the signal drops to 0.0 V the valve is opened, the muscle contracts and the catcher moves into the flux tube. While the catcher is in the beam position, a photo-barrier inside the catcher's controller creates a current that is sent to the signal processing stage where it is converted to a TTL signal. The rising edge of the signal (or its trailing edge in the opposite case when the catcher is moving out of the flux tube) is detected, read out and synchronized with the ORCA data stream. The pulse generator controlled by ORCA allows to adjust the movement patterns ("in" and "out" times) and to operate it in different modes: a) automatic with regular adjustable intervals during which the catchers are inside the flux tube, b)

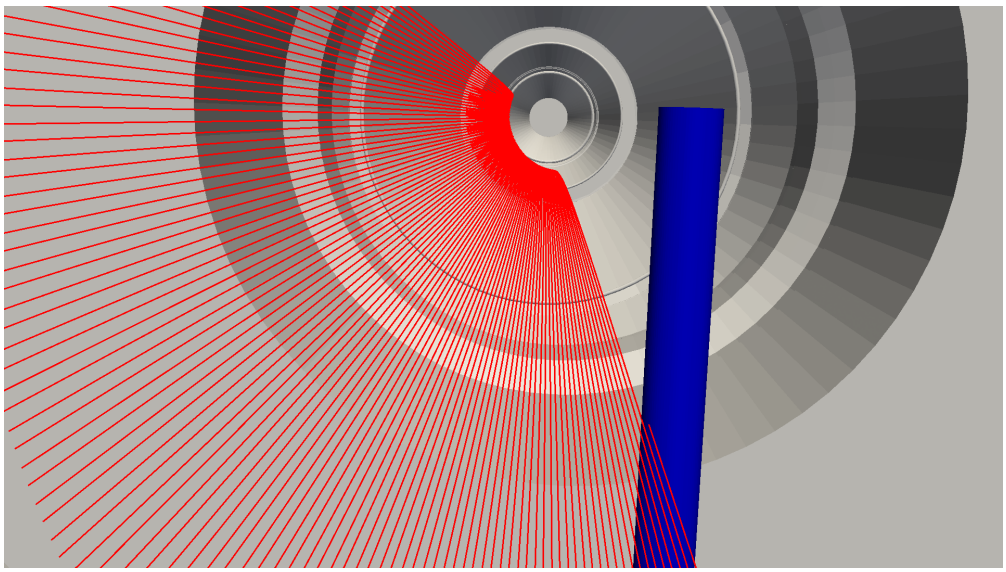

Figure 4.4: Simulated track of a trapped electron (red) up to the point where it hits the electron catcher (blue) (looking down the beamline). From [Ake+19b].

triggering when the detected electron rate at the FPD surpasses a user-defined threshold and c) manual.

The mechanical design of the electron catchers is shown in fig. 4.6. The catcher is attached to a bellow fixed inside a hinge to allow for tilting around one axis. This joint is contained within a housing and a spring attached to one of the walls holds the hinge in the parking position. On the other side, the hinge is connected via a bowden cable to a pneumatic muscle which when contracting pulls the hinge and moves the catcher into the flux tube. The pressurized air actuating the muscle is supplied through a pneumatic valve from a compressed air supply. The contraction speed of a pneumatic muscle and therefore the electron catcher sweeping speed (one-way movement in sub-s scale) can be regulated by manually adjusting a flow control valve. The photoelectric sensor of each electron catcher contains an infrared LED and a photodiode. When the catcher is moved into the flux tube, the LED light is reflected from the hinge and strikes the photodiode. All this instrumentation was developed and tested to be fully compatible with the multi-T magnetic field.

Movability is an important feature of the electron catcher system since a permanently inserted pin would shadow some of the FPD pixels (see fig. 4.7). Therefore the possibility to quickly move the electron catchers through the beamline and back into a parking position outside of the flux tube prevents unnecessary losses in statistics.

In the following, the investigations of the inter-spectrometer Penning trap behavior and the efficiency with which the electron catchers empty the trap are reported.

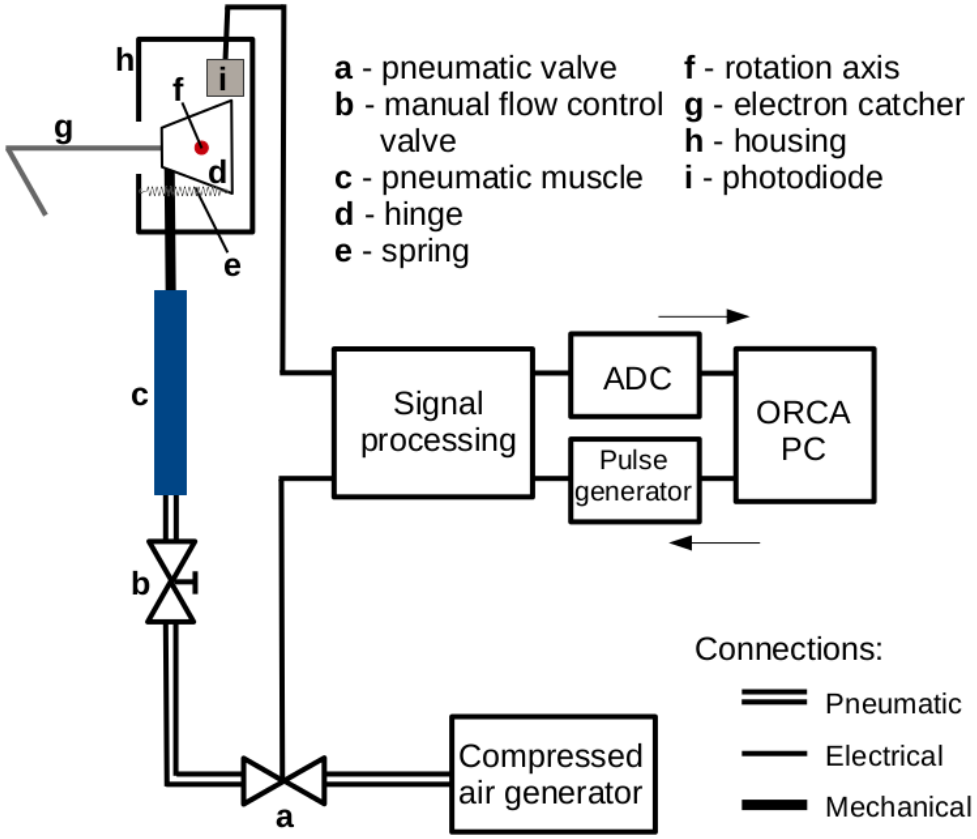

Figure 4.5: Schematic diagram of the electron catcher operation. The arrows show the direction of the data flow. To remove the catcher from the flux tube: 1) the pulse generator is first activated by ORCA and creates a TTL signal, 2) the signal proceeds to the signal processing stage and is transformed to a 24 V signal which closes the pneumatic valve (a) to the compressed air supply, 3) the pneumatic muscle (c) connected to the hinge (d), hold by the spring (e), is relaxed. When the signal drops to 0 V, the valve re-opens, the muscle is contracted pulling the hinge and rotating it around the axis (f) and moving the electron catcher (g) back into the flux tube. The speed of the muscle contraction and consequently of the catcher's movement can be regulated by the manual flow control valve (b). In this configuration, infrared light from an LED installed inside the photoelectric housing (h) is reflected from the hinge onto the photodiode (i). The photodiode signal enters the signal processing stage and is converted to a TTL signal. The signal increase (or decrease in the case the catcher is removed from the flux tube) is read out by the DAQ system.

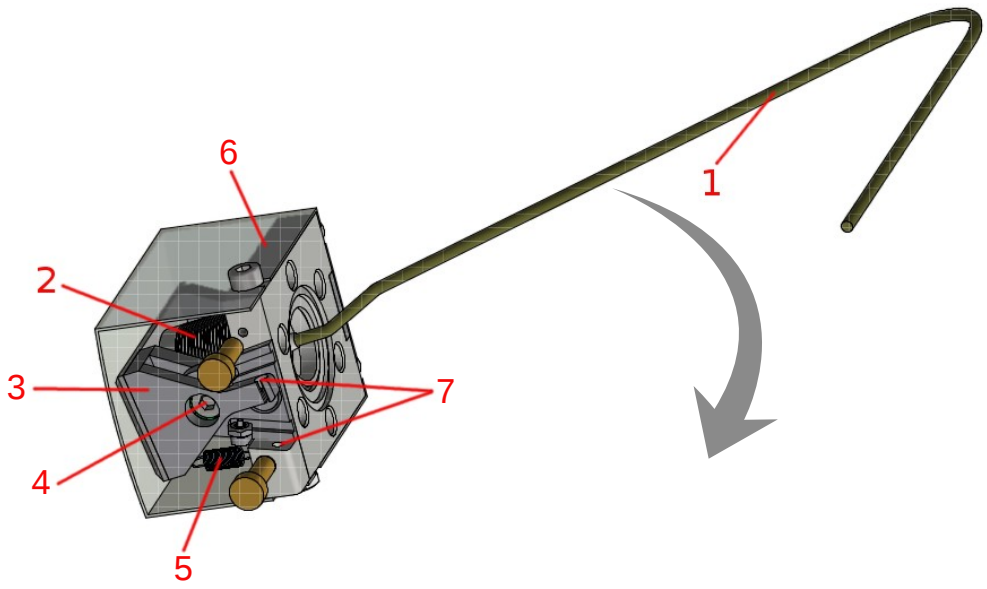

Figure 4.6: Technical drawing of an electron catcher: (1) - electron catcher, (2) - bellow, (3) - hinge, (4) - rotation axis, (5) -spring, (6) - photosensor housing, (7) - pneumatic muscle cable slots. The grey arrow shows the direction of the wiper when moving inside the flux tube.

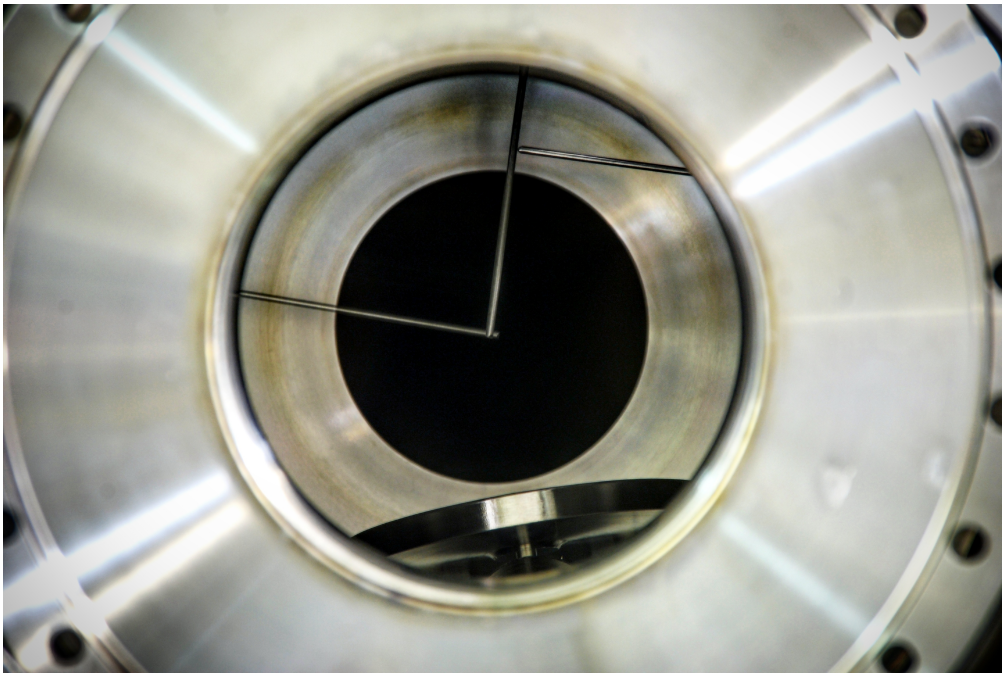

a

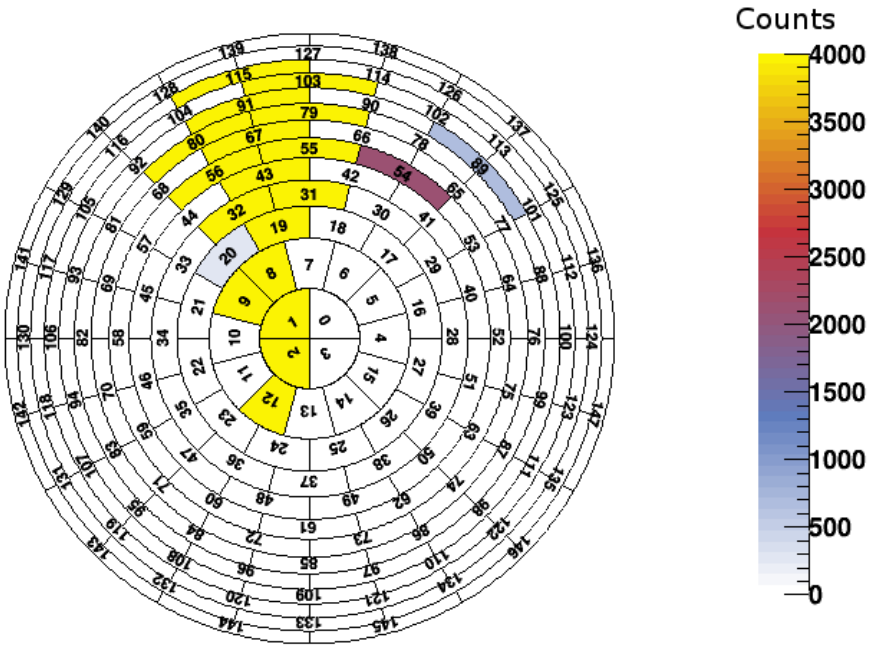

b

Figure 4.7: a) Catchers installed inside the valve between the spectrometers (looking down the beamline). The left and the upper catchers are inserted into the flux tube, the right catcher is retracted; b) Pixels affected by the shadow from one of the electron catchers on the FPD map. The total electron count from a photoelectron source was measured with only the upper electron catcher from fig. a inserted into the flux tube and was then subtracted from the one measured with all three catchers retracted for the same amount of time (10 min), which results in a higher count on the shadowed pixels.

4.3 Measurements and results

In this section, results of the inter-spectrometer Penning trap and the electron catchers tests under various pressure conditions and spectrometer settings are discussed.

4.3.1 Background measurements before bake-out

During the first test of the system in 2016 the pressure inside the spectrometers was on the order of 10^{-9} mbar. With the electron catchers retracted from the flux tube, the main spectrometer operated at -18.6 kV and magnetic fields at pre- and main spectrometers set to 20% of the maximum value of 4.5 T, *i.e.* 0.9 T, Penning discharges were appearing within 5 min from the beginning of a measurement already at a pre-spectrometer voltage of -2.6 kV. With the magnets set to 80% of the maximum field strength this threshold value was even lower: -2.0 kV, consistent with the fact that higher magnetic fields create stronger trapping conditions. Frequent and intensive rate bursts were observed unless being stopped by an electron catcher. Fig. 4.8 shows a test where one of the electron catchers was moved into the flux tube in a regular pattern with 30 s breaks during which a background spike developed a couple of times. The electron catchers were tested in different operational modes. A periodically moving electron catcher demonstrated an ability to quench appearing discharges, however, could not prevent their reappearance, as can be seen in fig. 4.8. A stationary catcher inserted into the flux tube made it possible to reach -18.4 kV at the pre-spectrometer without getting rate bursts (see fig. 4.9). However, such a method is disadvantageous during data-taking for neutrino mass measurement, since a non-negligible part of the statistics would be lost due to pixels shadowed by the catcher.

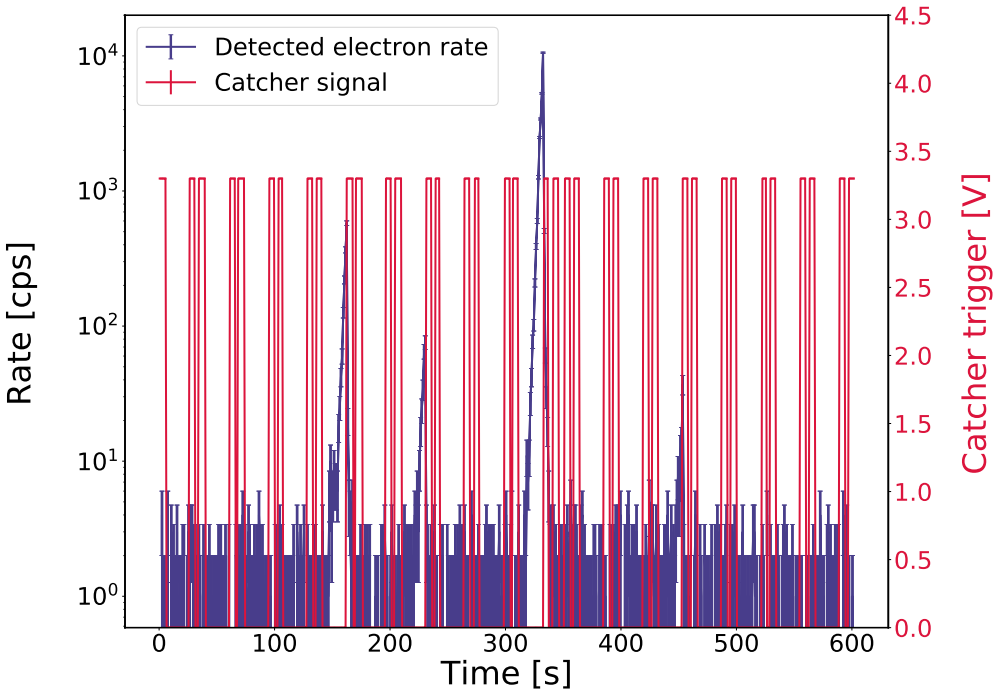

Figure 4.8: FPD background electron rate with 10^{-9} mbar pressure, 80% magnetic fields, $U_{PS} = -2.0\,\text{kV}$, $U_{MS} = -18.6\,\text{kV}$ and an electron catcher in a mode where the catcher was moving in a repeated pattern of 4 s inside, 4 s outside, 4 s inside and 30 s outside the flux tube, unless a safety script was triggered by an FPD rate higher than 10 kcps causing the catcher to move twice for 4 s with 4 s in between.

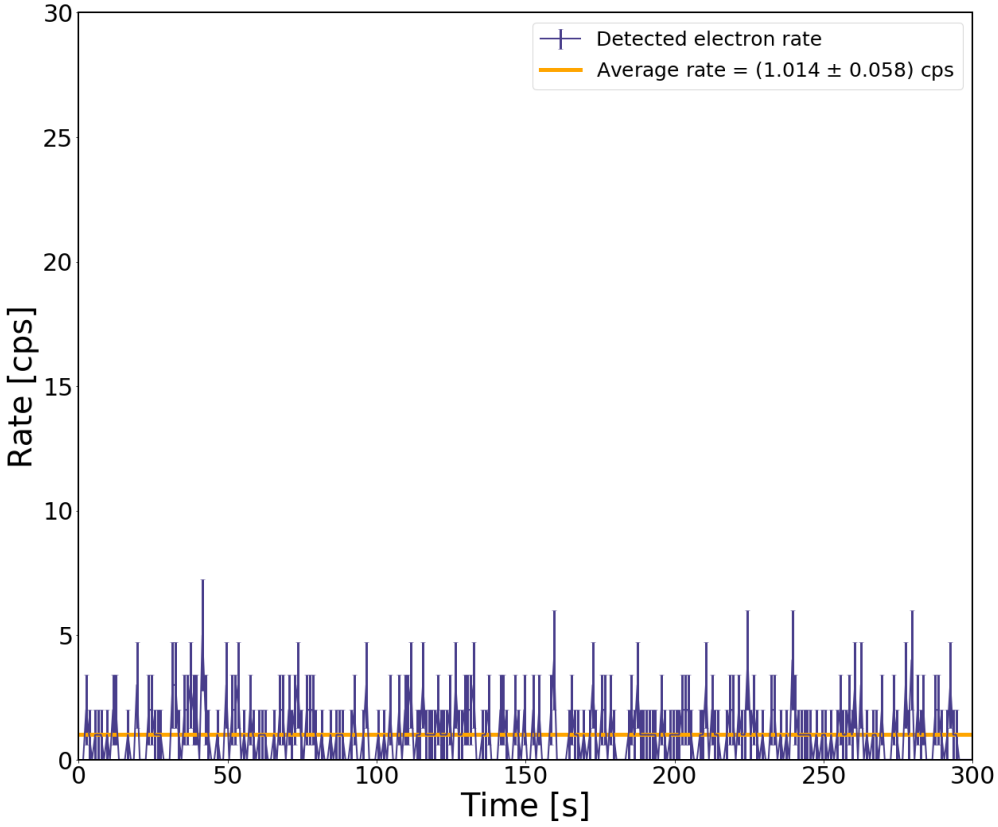

Figure 4.9: FPD electron rate with $\sim 2 \times 10^{-9}$ mbar pressure, $U_{PS} = -18.4\,\mathrm{kV}$, $U_{MS} = -18.6\,\mathrm{kV}$ and an electron catcher statically inserted into the flux tube. The magnetic field between the spectrometers were set to 15% and all other magnetic fields of the pre- and main spectrometers were scaled to 20% of the maximum values. No rate bursts were observed with this configuration.

4.3.2 Background measurements at different pressures after bake-out

Before the following measurement phase in 2017 the system was baked out and tests were conducted at different pressures. The pressure in the system was changed by inserting a small amount of argon gas through one of the pump ports in the main spectrometer. Two sets of measurements at residual gas pressures of $\sim 1.2 \times 10^{-11}$ mbar and $\sim 4.7 \times 10^{-10}$ mbar (the value is corrected for argon) have been performed to determine the background rate with the magnets set to 70% of the maximum field strength, the main spectrometer constantly on $U_{MS} = -18.6$ kV and U_{PS} being increased stepwise up to -18.4 kV (see fig. 4.10). As can be seen, the system is very sensitive to the pressure: while the rate stays at a constant low level for 1.2×10^{-11} mbar, a dramatic rate increase is observed with ~ 80 times higher pressure as we increase the pre-spectrometer voltage to more negative values than -14.4 kV.

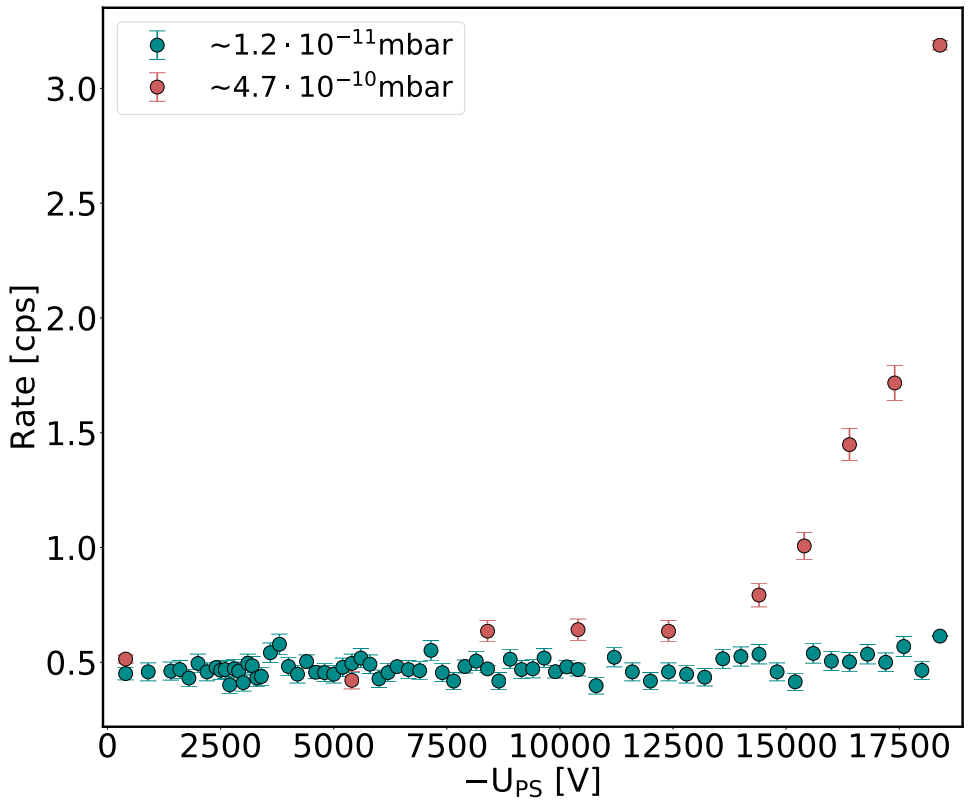

Figure 4.10: Measurements with two different pressure settings and variable applied PS electric potential, while $U_{MS} = -18.6$ kV stays constant. The magnetic field of the pre- and main spectrometers were scaled to 70% of the maximum value except for the main spectrometer LFCS scaled to 42% of the maximum value of 9 G (*i.e.* 3.8 G). A strong increase of the background rate induced by the Penning trap manifests itself for the higher pressure (red dots) for PS voltages more negative than $-14\,400$ V, while for the lower pressure (blue dots) the rate stays essentially unchanged for the whole range of PS voltages. For the measurement with the increased pressure, the indicated pressure value is corrected for argon.

During the same measurement phase, the catcher was tested in its safeguard operation mode at elevated pressures: the ORCA software was triggering movement of the electron catcher for a 20 s interval when the FPD rate reached 10 kcps. In fig. 4.11 we show the rate trend for pressure falling from $\sim 1.3 \times 10^{-9}$ mbar (to which it has been increased by inserting small amounts of argon

gas through one of the MS pump ports), when regular discharges were observed though effectively stopped by the electron catcher, to $\sim 7 \times 10^{-10}$ mbar, when the discharges disappear completely (pressure values are corrected for argon).

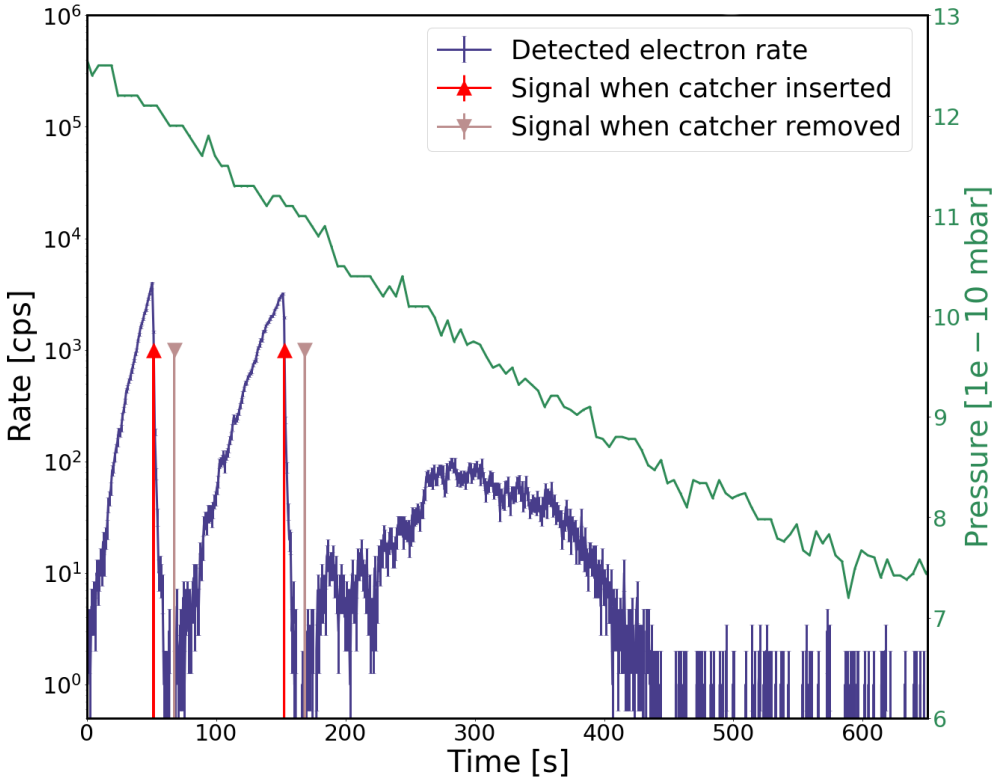

Figure 4.11: Measurement with decreasing pressure and the electron catcher running in the safeguard operation mode ($U_{PS} = -18.4\,\text{kV}$, $U_{MS} = -15.1\,\text{kV}$). The magnetic field of the pre- and main spectrometers were scaled to 70% of the maximum values except for the main spectrometer LFCS scaled to 42% of the maximum value of 9 G (*i.e.* 3.8 G). The electron catcher succesfully quenches discharges which disappear below $\sim 8 \times 10^{-10}$ mbar. Pressure has been initially increased by adding argon gas through an MS pump port. Pressure values are corrected for argon.

4.3.3 Background measurements at nominal pressure and spectrometer settings

The bake-out of the spectrometers allowed to reach the nominal spectrometer pressure of $\sim 10^{-11}$ mbar. The electric and magnetic field settings at the spectrometers planned for use during the neutrino mass measurements are $-18.3\,\mathrm{kV}$ at the pre-spectrometer, $-18.6\,\mathrm{kV}$ at the main spectrometer and 70% magnetic fields. These settings were used in a long-term background measurement at the end of 2017 to test the system behavior. No discharges or rate spikes were observed during two weeks of data-taking (see fig.4.12). For those measurements the pressure gauge at the pre-spectrometer was switched off since it proved to be an additional source of background. The electron catcher system was operated in safeguard mode during the measurements, but was not triggered.

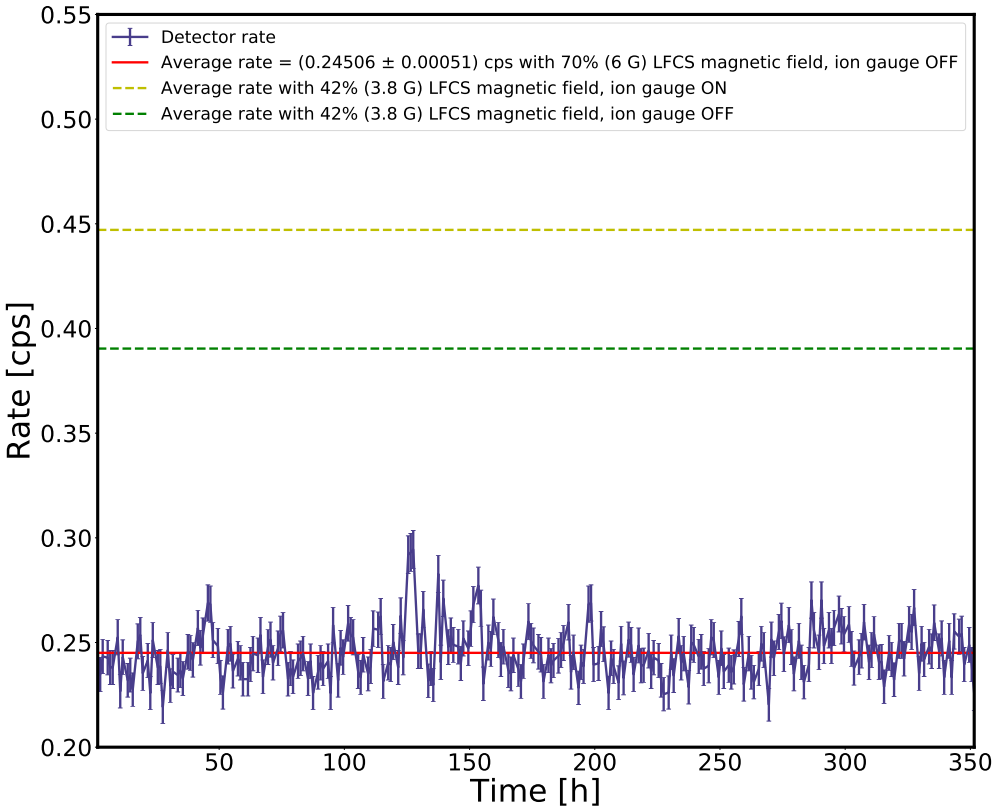

Figure 4.12: Background rate of a long-term measurement with nominal electric ($U_{PS} = -18.3\,\mathrm{kV}$, $U_{MS} = -18.6\,\mathrm{kV}$) and magnetic field settings (70% of the maximum values) and a pressure of $\sim 10^{-11}$ mbar, compared to average rates from measurements with lower magnetic fields of the LFCS (3.8 G, *i.e.* 42% of the maximum value) and the ion gauge off and on (the latter corresponding to the case in fig. 4.10). For all three measurements here, two pixel rings (pixels 4-10 and 136-147, see fig. 4.7b) which were damaged by a Penning discharge during one of the tests before the long-term measurement are excluded.

Chapter 5

Conclusions and outlook

The absolute neutrino mass scale is one of the most important open issues in neutrino and particle physics and its abnormal smallness is an indication of BSM physics. At the largest scales, neutrinos are involved in the formation of the visible structure of the Universe, affecting the formation and distribution of galaxies. There are various methods to approach this parameter, one of which is a direct measurement from the kinematics of beta decay. The experimental method is based on the work of V.M. Lobashev and P.E. Spivak, who in 1983 proposed a new type of electrostatic spectrometer using the effect of magnetic adiabatic collimation (MAC-E filter). Facilities including such a spectrometer were created at Troitsk with a windowless gaseous source of tritium and at the University of Mainz with a condensed tritium source. The groups independently determined an upper limit of about 2 eV for the observed neutrino mass. But the exact value remains an unresolved question to the present day.

Their successor, the KATRIN experiment, aims to improve the sensitivity to the neutrino mass by a factor of 10, to 0.2 eV at 90% C.L.. Its apparatus has a 70 m long beamline which has on one end a luminous windowless gaseous tritium source (with $\approx 1 \times 10^{11}$ Bq activity) and on the other end a pixelized focal plane detector to count beta electrons remaining after energy filtering. From the source, electrons are guided through the transport section, where tritium molecules are removed via differential and cryogenic pumping, towards two electrostatic spectrometers. The first one, called pre-spectrometer, rejects all but the last 300 eV of the spectrum. The second one, called main spectrometer, has a resolution of 0.93 eV and analyzes the endpoint region, where the background level has to be close to 10 mcps to reach the planned sensitivity.

To achieve such a precision, an absolute energy calibration and precise determination of the transmission functions of pre- and main spectrometer are required. For this purposes KATRIN exploits, among others, monoenergetic conversion electrons from an ^{83m}Kr source condensed onto an HOPG substrate. This so called CKrS and has a sophisticated structure to be able to move and work on top of the cryogenic pumping section. It allows for calibration measurements during breaks from tritium data taking due to its relative operational simplicity compared to the gaseous ^{83m}Kr source which KATRIN is using as another calibration source. The CKrS is a spot-like source and therefore allows a per-pixel determination of the spectrometer transmission function with comparatively high rates. The stability of the CKrS can be monitored by means of a laser ellipsometry system which is a tool allowing to study optical properties of frozen films and determine their thickness growth with a conservatively estimated uncertainty of about 2.4 Å. In this work, ellipsometry studies of krypton

films and comparisons to the spectroscopy data were done to investigate the relation between film thickness and energetic stability of the observed conversion lines.

The source was installed at TLK and has undergone the first commissioning in 2017. During this first measurement campaign, three ^{83m}Kr films were prepared and measured in parallel with ellipsometry monitoring. The measured line position shifts for each film are attributed to image-charge effects in accordance with ellipsometry observations: the line position drifts to lower values as the film thickness grows. Moreover, an improvement of vacuum conditions in the system was observed as a reduction in the thickness growth rate from the first to the third film.

To stabilize line positions for the calibration runs during the 2018 measurement campaign, a thorough bake-out of the source to achieve better vacuum and substrate pre-plating with stable krypton were applied. While bake-out did not bring any improvements, pre-plating with a layer of stable krypton of about 1 nm allowed to achieve a 10 times better stability (30 meV compared to 300 meV over 100 h) with a good reproducibility. A detailed analysis of the spectroscopy data is subject of the PhD thesis of A. Fulst [Ful19]. The CKrS source will be used to calibrate the spectrometer transmission function and high-voltage stability in-between tritium measurement runs throughout the KATRIN data-taking.

Another challenge on the way to achieve the KATRIN sensitivity goal is the inter-spectrometer Penning trap, which is unavoidable in a two-spectrometer set-up. It represents a considerable problem for the experiment since it can contribute to elevated background levels as well as presenting a danger to the spectrometer and detector section hardware due to possible discharges.

The instrumental solution to this problem is to use three movable Inconel rods called electron catchers inside the magnet bore between the spectrometers to remove trapped particles. In this thesis, an investigation of the effectiveness of this solution has been presented. At pressures in the 10^{-9} mbar region two potential modes were tested: a static electron catcher was able to preserve a quiet measurement environment while a moving catcher was able to fully quench discharges occurring in between the electron catcher operation. After the bake-out of the spectrometers, measurements at lower pressures proved a strong dependence of the Penning trap behavior on this parameter.

With the finally achieved ultra-high vacuum of $\sim 10^{-11}$ mbar, no Penning discharges were observed during a final two-weeks measurement. Still an on-demand operation of the electron catcher set-up is required as a safety measure in case a discharge does develop and the electron catchers will be used to remove stored electrons between tritium measurements or during retarding voltage changes.

Appendix A

Ultra-high energy neutrinos and Beyond the Standard Model Physics

Another exciting feature connected to the neutrino particle was discovered recently - an existence of cosmic neutrinos of extremely high (TeV-PeV range) energies. Many cosmic sources are considered as their possible birthplaces. Interestingly, apart from the old physics models, various new physics ones were proposed to explain their generation mechanisms. Some of them, specifically in the connection of the IceCube data, are discussed in this overview.

A.1 The "IceCube puzzle"

Apart from accelerator, reactor, solar and atmospheric neutrinos, mentioned in the introduction, it was clear that there should have been high-energy astrophysical neutrinos reaching us from the far Universe, but they have not been observed until recently. There can be different sources producing such cosmic neutrinos (see fig. A.1) [AH15]:

- Astrophysical objects working as accelerators for protons and other particles of cosmic rays (CR) (*e.g.* pulsars, active galactic nuclei etc.). Interacting with the environing matter, the protons generate hadrons, including charged pions, which emit neutrinos when decay.
- Interaction of high-energy CR with photons of the cosmic microwave background (CMB), which can go in two ways:

$$\gamma + p \to n + \pi^+(\pi^+\pi^-), \quad \gamma + p \to p + \pi^0. \tag{A.1}$$

  Decays of charged pions generate neutrino fluxes:

$$\pi^{+(-)} \to \mu^{+(-)} + \nu_\mu(\bar{\nu}_\mu), \quad \mu^{+(-)} \to e^{+(-)} + \bar{\nu}_\mu + \nu_e(\bar{\nu}_e + \nu_\mu), \tag{A.2}$$

  while decays of neutral pion generate photon fluxes:

$$\pi^0 \to \gamma + \gamma. \tag{A.3}$$

As can be seen from (A.1)-(A.3), an unavoidable effect of the CR interaction with the CMB is a neutrino flux. From the initial mixture of pions a mixture of photons and neutrinos in the proportion $2\gamma + 2\nu_\mu + 2\bar{\nu}_\mu + 2\nu_e + 2\bar{\nu}_e$ is formed and therefore the flavor content ratio of neutrino flux from the source $\nu_e : \nu_\mu : \nu_\tau$ is 1:2:0. After propagating over large distances, this ratio will be changed by neutrino oscillations to $\nu_e : \nu_\mu : \nu_\tau$ as 1:1:1. Moreover, those reactions give rise to theoretical upper bound on the energy of CR from far astrophysical objects, called Greisen-Zatsepin-Kuzmin (or GZK) cutoff [Gre66], [ZK66]: protons and nuclei with energy more than 5×10^{19} eV will interact with photons until their energy will drop below the threshold.

- decay of heavy dark matter particles.

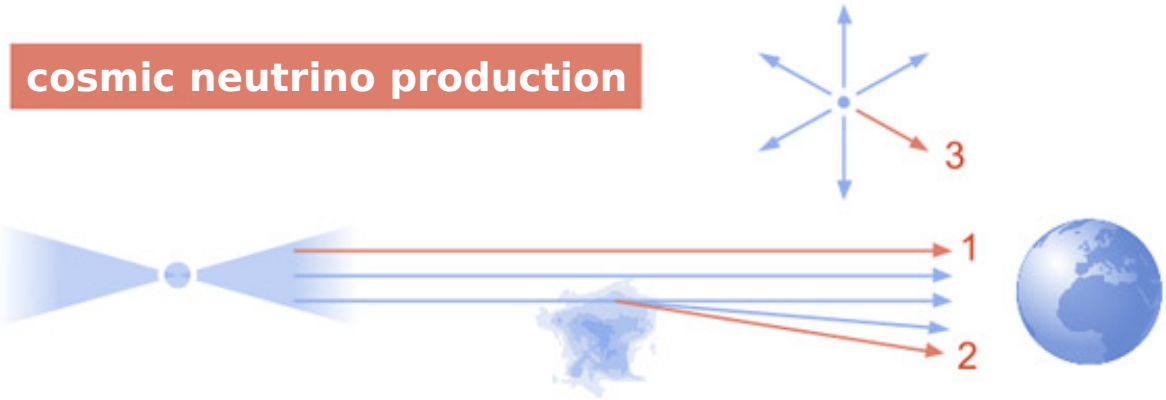

Figure A.1: Three possible sources of high energy astrophysical neutrinos: 1 - they can simply arise and accelerate in a "cosmic accelerator", for example, in a pulsar; 2 - they can be produced in collisions of CR with CMB; 3 - they can occur with the decay of dark matter particles (figure adapted from [Elea]).

The first two points imply, that neutrinos are everywhere where CR are. This fact is particularly important in the light of our present ignorance of the sources of ultra-high energy ($\gtrsim 10^{18}$ eV) cosmic rays (UHECR). As can be seen in fig. A.2, the CR spectrum is following a broken power-law distribution and has two main features, called *knee* at around 4×10^{15} eV and *ankle* at around 5×10^{18} eV. This is because CR of different energies come from different sources [AH15]. CR originating from various sources inside our Galaxy have energies up to about 10^{18} eV. The flux at energies of the order 10^{16} eV is one particle per square meter per year. The most energetic rays come to us from unknown sources outside the Milky Way. The kink in the spectrum of galactic CR shows that the contribution of extragalactic CR changes dramatically when moving from a region of moderate energies 10^{14} eV-10^{16} eV, where it is about 30 times smaller than the contribution of galactic CR, to the region of ultrahigh energies, where it becomes dominant at around 10^{18} eV and extends to 10^{20} eV. The number of CR particles is already very small there: one can expect no more than one particle with an energy of 10^{20} eV per square kilometer per century. Our knowledge of where the transition from galactic to extragalactic CR in the spectrum occurs is imprecise.

Why are particles with ultra-high energies thought to be of extragalactic origin? Because in order to accelerate particles to such energies, very strong magnetic fields of enormous extent are needed. An obvious sign that an object of size D can accelerate particles to energy E is the presence

of a magnetic field B throughout this object such that the gyro-radius of a particle is less than D:

$$\frac{\gamma m v^2}{R} = \frac{\gamma m v^2}{\frac{D}{2}} = qvB \Rightarrow \frac{D}{2} = \frac{\gamma m v}{qB} = \frac{p}{qB} \approx \frac{E}{qB} \text{ for } c = 1, \tag{A.4}$$

which means that not large objects are needed to accelerate a particle to high energies necessarily but objects with large B. For the energies above the ankle, the gyro-radius of a proton in the Galactic magnetic field exceeds the size of the Galaxy. Moreover, if there were at least one compact source of the UHECR in the Milky Way, then there would be a very strong heterogeneity in the directions of arrival, indicating this source. But there is no such heterogeneity observed. The candidate sources include radio galaxies (emitting strong radio emissions), nuclei of active galaxies containing black holes, colliding galaxies. All of them contain gas (plasma) jets moving at tremendous speeds, approaching the speed of light. Such jets play the role of shock waves necessary for the operation of the accelerator. It is however unclear if one of the known objects like this could supply CR with energies above the GZK limit.

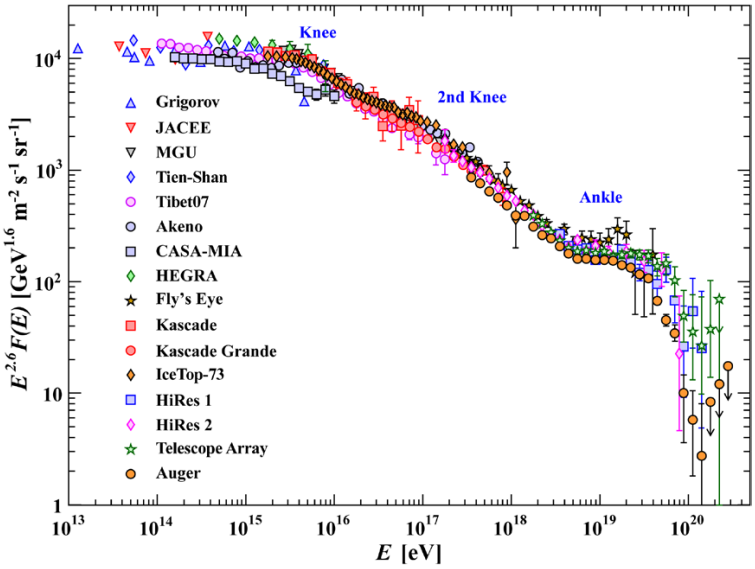

Figure A.2: Experimental data of all-particle CR flux in a wide range of primary particle energy. The spectrum can be described by a power-law with 3 remarkable features: the "knee" at around 4×10^{15} eV, the "2nd knee" at around 4×10^{17} eV and the "ankle" at around 10^{18} eV, discussed in the text. From [Oli14].

Therefore, astrophysical neutrinos are a new and potentially perspective instrument for cosmic observations and investigations of high energy processes in our Universe. In contrast to protons, electrons and other particles, neutrinos are not deflected by electric and magnetic fields and therefore their arrival directions point directly to their source. Also, unlike photons, neutrinos interact very weekly with matter, and therefore allow a spectator to see through thick gas and dust clouds. Unfortunately, the same property make them very hard to detect and requires immense kilometer-scale detector arrays. Another problem, concerning particularly registration of astrophysical neutrinos, is that their amount reaching us is a few orders of magnitude smaller comparing to atmospheric and especially solar neutrinos. However, solar neutrinos have energies of several MeV, and they can be easily cut off by increasing energy threshold. With atmospheric

neutrinos, the situation is more complicated, but the flow of atmospheric neutrinos decreases rapidly with energy. In order to produce a neutrino, a particle (*e.g.* charged poin, kaon or muon) must disintegrate, and as the energy increases, the decay base grows, and it is no longer enough - the particle interacts with matter instead of decay. Therefore, neutrinos with very high energy (more than 10^{14} eV), most likely, flew in from far space. Such a detector array, the IceCube detector, was able to register an astrophysical ultra-high energy neutrino (UHEν) of more than 10^{15} eV energy for the first time in 2013, which raised the so-called "IceCube puzzle", which will be discussed later.

The working substance of IceCube is a cubic kilometer of Antarctic ice at the South Pole (see fig. A.3) which is used as a transparent media for detection of Cherenkov light from particles produced in charged current (CC) interactions of neutrinos. Sensitive photocells in IceCube are organized in the form of strings, which were descended into 2.5 km deep boreholes (ice melted by hot water), where they were frozen into the surrounding ice. IceCube consists of 86 such strings of 60 photomultipliers each, and the strings themselves are located 125 meters away from each other. In addition, in the center of the detector there is a small area with a more dense arrangement of the detectors (so called Deep Core) and the IceTop cosmic ray sensor located above the IceCube [Aar+17]. This sensor makes it possible to distinguish a single cosmic neutrino from a neutrino born in the atmosphere: in the first case, the powerful neutrino signal inside the IceCube occurs alone, and in the second case, the IceTop detects a wide shower of secondary particles coinciding in time (see fig. A.4). The events are broadly classified as tracks, which are associated with CC interactions of muon neutrinos, and cascades, which are produced by CC interactions of electron and tau neutrinos or neutral current (NC) interaction of neutrinos of all flavors [AH15]. The accuracy of the muon direction reconstruction is 0.5°-0.3° depending on the energy. The energy recovery is rather imprecise, since the detector sees only a part of the track, losses for muon due interaction with matter are stochastic, and their dependence on energy is logarithmic. Only the lowest energy limit is reliably determined. Typical events topologies for different neutrino flavors are shown in fig. A.5.

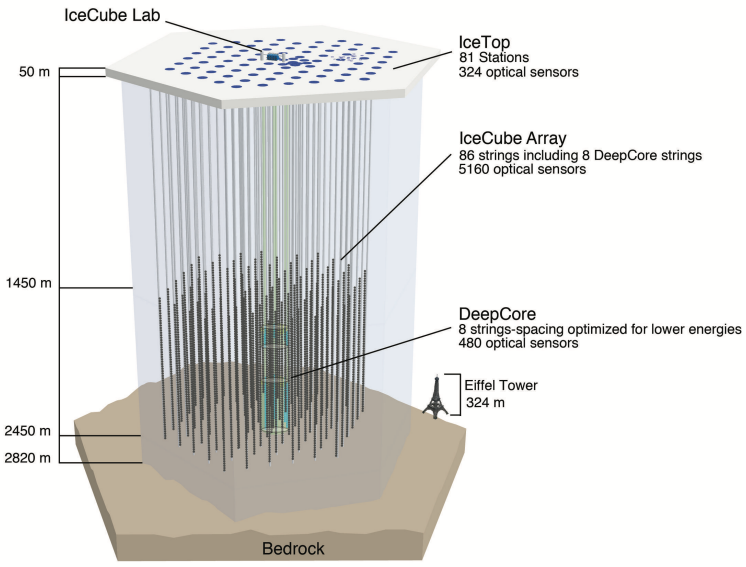

Figure A.3: Schematic view of the IceCube set-up, together with the denser configuration of the optical modules, DeepCore, and the surface CR detector, IceTop. From [Aar+19].

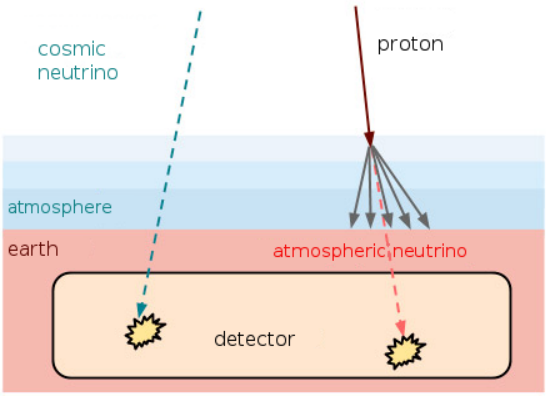

Figure A.4: The two types of high energy neutrinos coming to an underground (under-ice) detector: an astrophysical neutrino (on the left), coming directly from the deep cosmos, and an atmospheric neutrino (on the right), born in the upper parts of the atmosphere in a collision of a high-energy proton and creation of secondary particles, one of which produces the neutrino in a decay (figure adapted from [Eleb]).

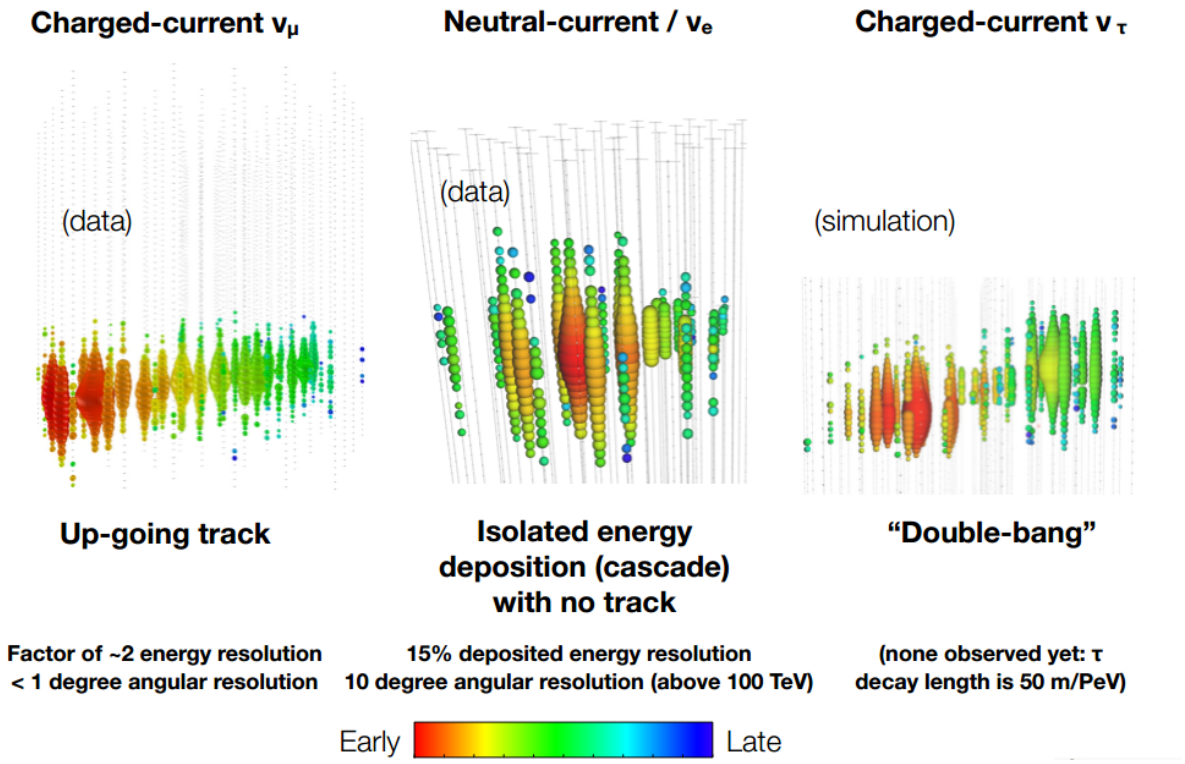

Figure A.5: Exmaples of different types of events at the IceCube detector. Each sensor is showed with a dot whose diameter is proportional to the number of detected photons and the color represents the time sequence. Track signals are left by $\mu^{\pm}$ produced in a CC $\nu_\mu(\bar{\nu}_\mu)$ interaction or air shower, cascades are induced by CC interaction of $\nu_e(\bar{\nu}_e)$ or any NC $\nu(\bar{\nu})$ interaction and "double bang" is a signature of CC $\nu_\tau(\bar{\nu}_\tau)$ interaction. From [Ice].

The first goal of IceCube was to register the highest energy neutrinos that could fit in its detector. In summer 2013, the collaboration reported the first loud result: in the data of the first two years of operation, May 2010 to May 2012, two neutrino events with energies of 1.04×10^{15} eV and 1.14×10^{15} eV were detected [Aar+13]. Atmospheric neutrinos with such energies almost should

not have remained; the probability that these two neutrino events were of atmospheric and not astrophysical origin, was less than a percent (statistical significance 2.8σ), which, however, was not enough for an absolutely reliable report on the discovery of astrophysical neutrinos of these two examples.

Encouraged by the first success, the collaboration decided to go down in energy. The new analysis, published in the end of 2013 [Col13], dealt with neutrinos with energies above 30×10^{12} eV. More precisely, this restriction refers to the energy release recorded by the detector; the neutrino energy itself could have been higher. In the data of the first two years for such neutrinos, 28 were found. According to theoretical calculations, the number of purely atmospheric neutrinos, as well as events caused by deep-penetrating muons of such energies, should have been around 10-15. Thus, a serious indication emerged that the IceCube "sees" true astrophysical neutrinos. The statistical significance of the astrophysical signal has grown to 4σ. According to the criteria of validity adopted in elementary particle physics, this is already close, but still not sufficient to confidently report the discovery. This has been, however, already resolved, and after additional 4 years of measurements (2012-2016) and applying an identical analysis to 6 years of data containing 82 events in the energy range from 60×10^{12} eV to 10×10^{15} eV a purely atmospheric explanation can be excluded at 8σ. Comparison of the measured flux to atmospheric background can be seen in fig. A.6. Directional distribution of the most energetic events is shown in fig. A.7: if taking into account absorption of 1×10^{14} eV neutrinos in the Southern Hemisphere, the distribution of arrival directions of the high-energy neutrinos is isotropic and thus corresponds to expectations from extragalactic sources. [AH18].

On September 22, 2017, IceCube registered a muon from neutron energy of at least 1.8×10^{14} eV (the most likely value is 2.9×10^{14} eV), called IceCube-170922A, which corresponds to blazar TXS 0506 with an accuracy of $\pm 0.5\,^{\circ}$. An indirect confirmation that TXS 0506 is relevant to the case was that this neutrino coincided in time with the flare of this object, observed in high-energy gamma rays by telescopes, aligned with the cosmic neutrino arrival direction within less than $0.1\,^{\circ}$ and a chance coincidence being excluded at $\sim 3\sigma$ level [Aar+18a], [Ans+18]. A stronger evidence came from excavations of archival data of all neutrinos that came from this direction (a circle of a degree size around TXS 0506). Mostly neutrinos of moderate energies up to 10^{13} eV were found there, among which atmospheric ones prevail. But in the end of 2014 - the beginning of 2015, a bunch of above-average energy neutrino came from the investigated region, being together with the neutrino event of 2017 a sufficient evidence to talk about a discovery of neutrino radiation from this object. [Aar+18b]

A.2 Possible Standard Model origins of UHEνs

According to current ideas, main source candidates of high-energy neutrinos within the Standard Model are:

1) Supernova (SN) explosions. For example, in case of type II supernova, $\sim 99\%$ of energy is carried away by MeV-neutrinos within the first second after the core bounce [Zub11], but 10 hours after the collapse it may produce a 1 h-long flash of TeV-energy neutrinos [WL01]. GRB-associated (or engine-driven) SNe are predicted to have a diffuse flux of $\sim 10^{-11}$-10^{-10} GeV cm^{-2} sr^{-1} in the 10^{17} eV-10^{18} eV range [ZM18]. At the same time, the source of neutrinos may include supernova

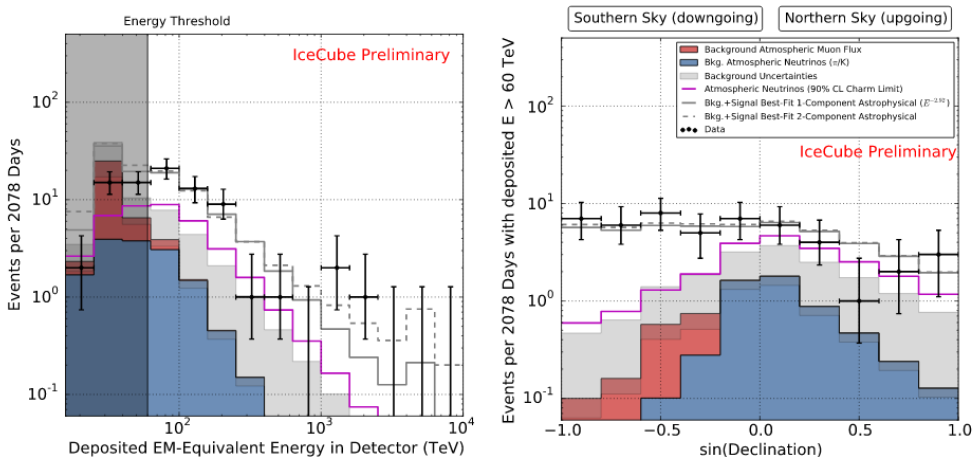

Figure A.6: Left plot displays deposited energy spectrum from 6-years IceCube data. The right plot shows the same data above 6×10^{13} eV in the angular distribution, where it is seen that the rate is flat in the Southern Hemisphere, which is consistent with expectation from isotropic astrophysical flux. From [AH18].

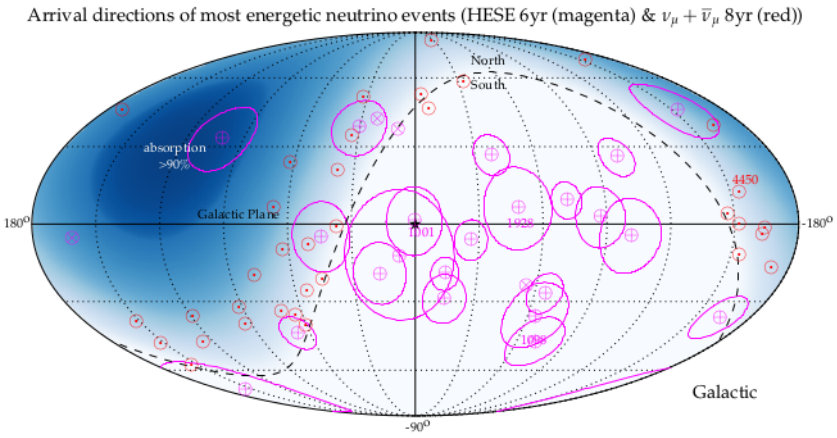

Figure A.7: The distribution of the arrival directions of high-energy neutrinos across the sky in galactic coordinates, where the dashed line indicates the horizon and the star indicates the Galactic Center. The center of the map corresponds to the center of our galaxy, the equator shows the plane of the Galaxy. $\odot$ indicates events with reconstructed muon energy more than 2×10^{14} eV from 8-years data set, $\otimes$ and $\oplus$ (surrounded by thin circles for median angular resolution) indicate correspondingly track and cascade events with deposited energy larger than 10^{14} eV from 6-year HESE (high-energy starting events) analysis. The blue-shaded region indicates the direction where Earth absorption of 10^{14} eV neutrinos becomes significant. From [AH18].

remnants, the gas and dust formations, appearing during the explosion of supernovae [Roy99]. The most well-known ones are Crab, Cassiopeia A, RX J1713.7-3946, SN1987 A, from which γs of up to tens of TeV energies are observed. If origin of those γs is connected to π^0 decays, then along with them charged pions, produced in photo-nuclear interaction, will give a flux of neutrino with $O(10^{13})$eV energies.

2) Various astrophysical objects, such as double systems which consist of two gravitationally bound objects revolving in closed orbits around common center of mass. Among them there are microquasars [TRM05], where one of the participants is a neutron star or a black hole in which

matter is accreted from a partner star (for example, LS 5039). They are sources of jets, in which protons are accelerated and interact with synchrotron γs. During an active stage of a microquazar (about a few hours), photomesonic reactions lead to neutrino fluxes of 10^{12} eV-10^{13} eV energies. Another type of interest for neutrino astrophysics is pulsars [Fan15] (rotating neutron stars with magnetic field) in the system of binary stars. Also, magnetars (neutron stars with extremely high magnetic fields) on their own can be sources of high-energy neutrinos [Dey18]: in magnetospheres of such stars accelerating protons interact with thermal photons and produce 10^{12} eV-2×10^{12} eV energy neutrinos through a Δ-resonance.

3) Gamma-ray bursts (GRBs), the short-term (from milliseconds to hundreds of seconds) and very intense flashes of γ-radiation. Their formation is associated with supernova explosions when a supermassive star collapses, or with a merge of a double object. They are usually followed by an afterglow in longer wavelengths (X-ray, UV, optic, IR and radio). Detectable neutrinos of 10^{14} eV-10^{17} eV energies can be produced in GRB-processes by internal or external shocks via pp or $p\gamma$ interactions [Mur07].

4) Active galactic nuclei (AGNs) of spiral galaxies (10^7-10^9 solar masses). AGNs are powerful sources of radiation in the Universe fed by gravitational energy of a matter falling into a black hole. This matter forms an accretion disk, which shines in the ultraviolet and X-rays. Luminosity of AGNs is less than of GRBs, but they radiate during longer time periods with regular bursts of a few days length [CW99], [Sre+99]. If an AGN is very powerful, it is called quasar. The accretion disks of some quasars shine 10 thousands times brighter than our Galaxy, although such objects are very rare. Quasars are much more common in the young Universe ($z > 1$), the peak of their abundance falls on the first 1-4 billion years of the Universe. Another remarkable and important detail of an AGN are jets of magnetized plasma, flowing perpendicular to the accretion disk, along the axis of rotation of the black hole. They move almost at the speed of light, with the Lorentz factor γ usually of 15-20, sometimes higher than 50. Because of the large γ, everything that the jet particles emit is directed forward in a cone with an opening of γ^{-1}. If the jet is directed onto a spectator, it is called a blazar for the spectator. In an AGN, protons can be accelerated up to 10^{20} eV and their interactions should lead to creation of neutrino and gamma-ray fluxes of 10^{19} eV and 10^{13} eV correspondingly [RM98], [Mur17].

5) The so called "Fermi Bubbles", an extended source of γ-radiation with hundreds of GeV energies on both sides of the Galactic disk, discovered by the FermiLAT gamma telescope. The nature of the Fermi Bubbles is not completely understood. However, their location clearly indicates the connection of the bubbles with the activity of the Galactic Center, where energy is released as a result of the tidal disruption of stars during an accretion on the central black hole. Radiation in Fermi Bubbles can be generated by various processes involving relativistic electrons accelerated by shock waves, which are formed when stellar matter falls on the black hole. In this case, the shock waves should also accelerate the protons and light nuclei that make up the CR. The giant shock fronts of Fermi Bubbles could additionally accelerate protons emitted by supernovae to energies substantially higher than 10^{15} eV. Hadronic and leptonic scenarios can be distinguished via their neutrino emission [LR12].

Also, nonlocalized sources of neutrinos are possible:

1) GZK-neutrinos of ultra-high energy can presumably be born in the interactions of high-energy

protons with relic radiation, *i.e.* in the processes described in the framework of the GZK effect [Ahl15]:

$$p + \gamma \to n + \pi^+, \tag{A.5}$$

$$\pi^+ \to \nu_\mu + \mu^+, \tag{A.6}$$

$$\mu^+ \to e^+ + \nu_e + \bar{\nu}_\mu. \tag{A.7}$$

2) Z-bursts. In addition to relic photons with a temperature of 2.7 K, relic neutrinos should be stored in the Universe which at the moment are theoretically cooled to $T \approx 19$ K. The Z-burst mechanism is the only interaction mechanism with relic neutrinos. Neutrinos of ultra-high energies, emitted by cosmic accelerators, interact with relic neutrinos producing Z-bosons with the following decay of Z-bosons which lead to the appearance of hadronic jets, the latter being sources of neutrinos of smaller (relative to the initial) energies: $\nu_i + \bar{\nu}_i \to Z^0 \to f + \bar{f}$ [FMS99], [Wei99].

A.3 BSM physics and UHEνs

A.3.1 Possible BSM sources of UHEνs

1) One of the first things to think about in the context of possible high-energy neutrino sources is that alternatively to CR interaction with gas and radiation, assumed for the previous sources, neutrinos can be produced via various processes of a heavy dark matter (DM) decay/annihilation. Although DM should be stable over the cosmological timescales (its life-time should be greater than the life-time of the Universe), its rare decays can give rise to observable neutrino fluxes, both as galactic and extragalactic contributions of a comparable size (but different in angular distribution and spectral shape), unlike for the annihilation case, where galactic component usually dominates extragalactic; also, signals from decaying DM should have in general less angular dependence as well as amplification by higher DM densities and redshifts [Mur00].

While the initial flavor content information would be lost due to the flavor redistribution by the oscillations, observed energy spectrum can provide information about the DM decay channel in which neutrino signal was produced. For example, many existing DM models predict a decay into $\gamma\nu(\bar{\nu})$ or $\nu\bar{\nu}$ in the case of a fermion or a scalar particle correspondingly, where a spectrum will contain a monochromatic line and an integral of the red-shifted extragalactic component, whereas in the other possible decay into $(Z^0, h)\nu$ there will be an additional continuous component from neutrinos produced in Z^0 and Higgs boson decay. Decay into other particles (*e.g.* muons, taus etc.) will produce a softer neutrino spectrum. It also can happen via a three-body decay like $e^+e^-\nu(\bar{\nu})$, mediated by a heavy scalar or a heavy boson, and in that case can be distinguished by a characteristic form (see fig. A.8). A comparison of calculations for different DM decay channels to experimental data is shown in fig. A.9: as can be seen, the predicted neutrino flux from DM lies significantly lower than the registered muon neutrino flux, therefore an effective background suppression is needed to distinguish the DM signal. [ITW13]

Galactic anisotropy of neutrino signal from decaying DM would be rather weak since about

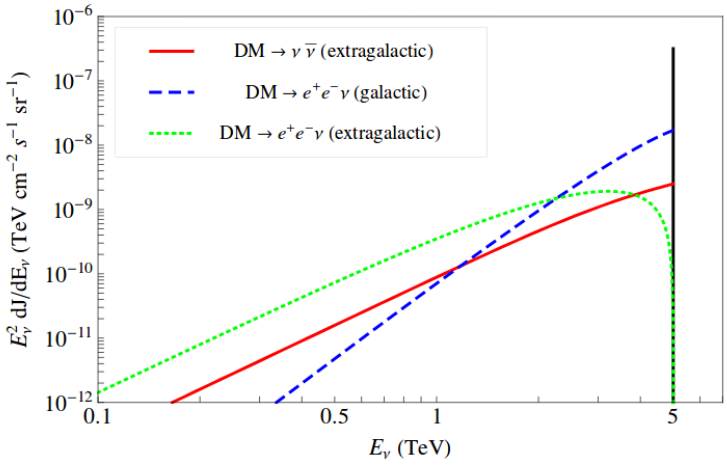

Figure A.8: Neutrino energy spectrum observed at Earth for 2-body and 3-body DM decay of a DM particle of 10^{13} eV mass and lifetime of 10^{26} s. Maximum neutrino energy is a half mass of the decaying DM particle and the solid vertical black line at this position (5×10^{12} eV) represents a two-body decay contribution from the Galactic Halo. The red solid line corresponds to the extragalactic contribution from 2-body decay, the blue dashed line and green dotted line correspond to the galactic and extragalactic contributions from 3-body decay respectively. From [EIP12].

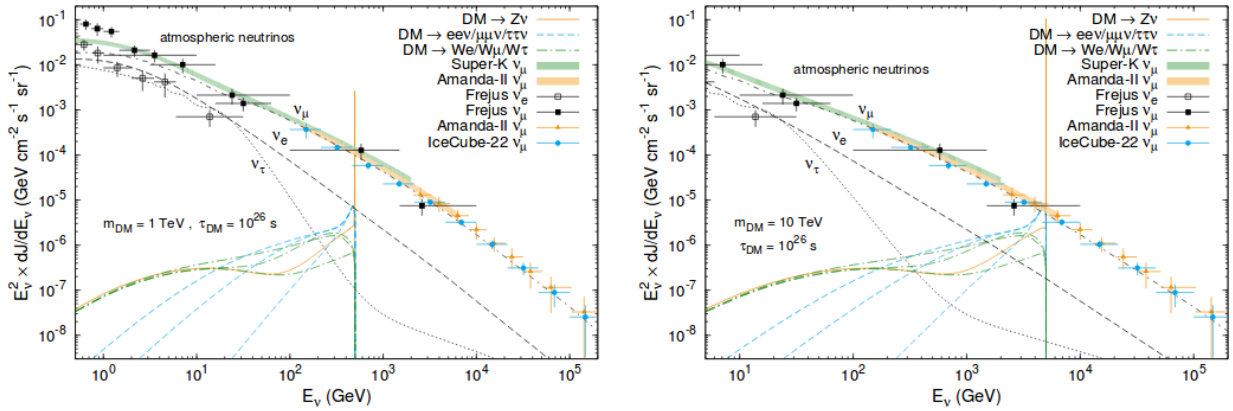

Figure A.9: Neutrino energy spectrum for different DM decay channels for a fermionic DM particle of 10^{12} eV (left) and 10^{13} eV (right) mass and lifetime of 10^{26} s including both the galactic and extragalactic component, together with expectations for the atmospheric background and measured data. From [ITW13].

half of the Galactic neutrino signal will be within 60 ° around the Galactic Center [AH15] (unlike for the annihilating DM, where neutrino signal will be more localized towards the Galactic Center [Aar+15c]), therefore, the Galactic component is not excluded by the present IceCube data (shown in the fig. A.7), if taking into account low statistics and angular resolution of the cascade-dominated samples [AH18], and decaying DM interpretation is preferred by the isotropy of the present data. However, no significant DM excess was identified in the data, and the lower lifetime limit of 10^{28} s for heavy DM particles with mass greater than 10^{13} eV was derived [Icd]. Moreover, as the 10^{14} eV threshold will be surpassed by observed neutrino energies, annihilating WIMP DM as a source of UHE neutrinos would be excluded because such energies lie beyond perturbative unitary bound [RKP15].

Heavy DM particles (with mass in the range between 10^6 GeV and 10^{16} GeV) decay was considered

in the light of γ-ray and the IceCube neutrino data in [KKK18] and it was shown, that the data disfavors hadronic decay channel, but the IceCube neutrino data could be explained without overproduction of γs for the masses less than 5.5×10^7 GeV and between 10^8 GeV and 1.5×10^9 GeV (see fig. A.10).

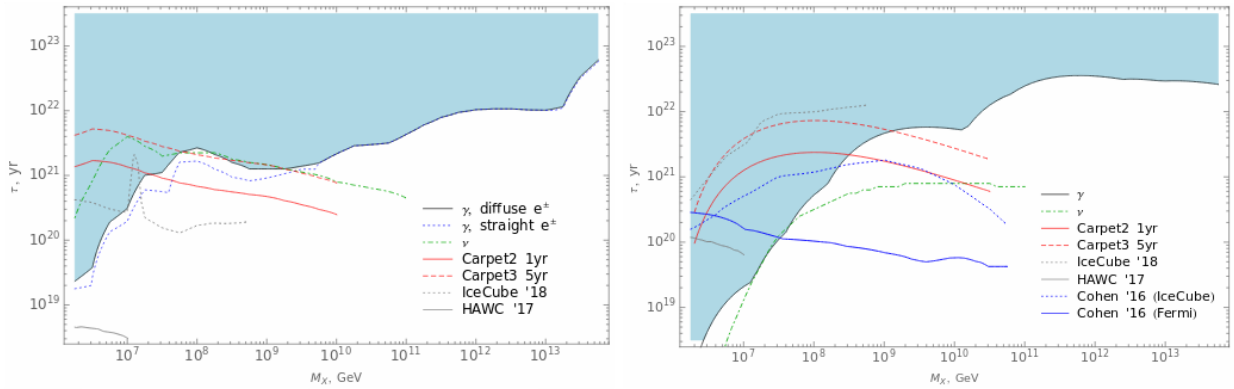

(a) $X \to \nu\bar{\nu}$ (b) $X \to q\bar{q}$

Figure A.10: A comparison of gamma rays and neutrino constraints for leptonic and hadronic decay channel of heavy DM particles. The constraints for hadronic decay is weaker in the case of neutrino signal than in the case of gamma rays almost everywhere on the mass range, and therefore this decay is disfavored as an explanation of the UHEνs events at the IceCube. From [KKK18].

2) Another "nonacceleration" exotic way for neutrinos to be produced could be decays of topological defects (TDs) in the Universe. This scenario assumes an existence of supermassive ($m > 10^{21}$ eV) metastable particles produced at the early stages of the Universe formation (which also could be a part of its DM) as a result of non-thermal symmetry-breaking phase transition. It could be cosmic strings, superconducting strings, magnetic monopoles, monopoles connected to strings, cosmic loops, vortons, bound monopole-antimonopole states, domain walls etc. When TDs are destroyed (by collapse or annihilation), they can produce particles, denoted as X, of the fields that generated those defects from the stored energy which then can decay into other particles that can produce neutrinos in their turn.

The rate of release of X particles with mass M_X from the collapse of topological defects at the Hubble time t is

$$\frac{dN_X(t)}{dt} = \kappa M_X^p t^{-4+p}, \tag{A.8}$$

where κ and p are dimensionless constant which depend on characteristics of the TDs (*e.g.* $p = 1$ for monopole-antimonopole bound state, $p = 0$ for superconducting cosmic string etc.). Example neutrino spectra for different p values were calculated in [BHS92] assuming X decaying into a quark and a lepton each of $M_X/2$ energy with the following hadronization of quarks. Pions formed in this process will result in a neutrino flux, which could be seen in the fig. A.11:

A.3.2 Constraints on relevant BSM scenarios

1) Leptoquarks are superheavy (of the GUT-scale order) color-triplet carrying simultaneously non-zero leptonic and baryonic numbers predicted in many BSM models. They are carrying information

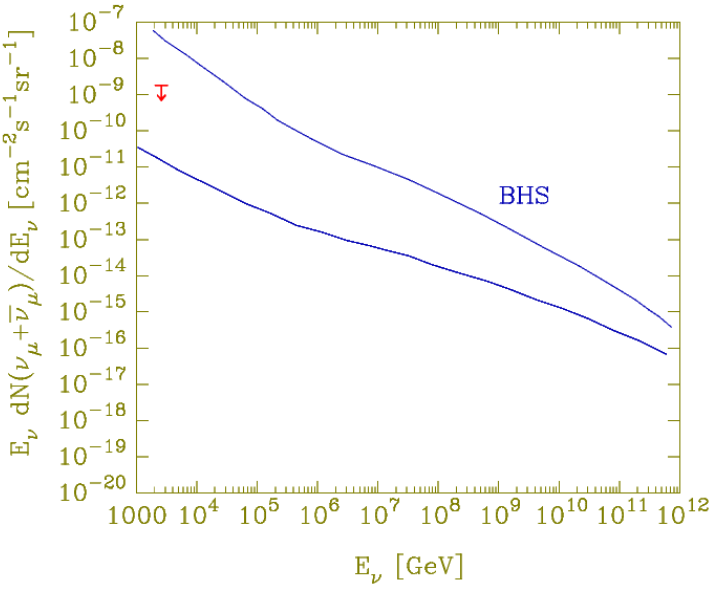

Figure A.11: $\nu_\mu + \bar{\nu}_\mu$ flux at the Earth calculated from a diffuse flux from a decay of TD models. The curves correspond to $p = 1.5$ (upper) and $p = 1.0$ (lower) in eq. (A.8). From [Qui96].

between quarks and leptons. Their existence would explain similarities in quark and lepton sector, in particular, the same number of generations. Moreover, they could also explain challenging for the SM observations of anomalous magnetic moment of muon and LHCb R_{K^*}&R_K data (showing a 2.5σ deviation from the SM) which point to the lepton flavor universality violation.

Leptoquarks could be produced in neutrino-nucleon interactions at IceCube and could also be used to explain the UHE neutrino excess. In the literature, a) S_1 leptoquark scalar singlet (3, 1, -1/3) [BK13], b) leptoquark scalar doublets: $\tilde{R}_2$ leptoquark having the representation (3,2,1/6) and R_2 leptoquark having the representation (3,2,7/6) under the Standard Model gauge group $SU(3)_c \otimes SU(2)_L \otimes U(1)_Y$ [CKN18], [Dey+18] and c) S_3 leptoquark scalar triplet (3, 3, -1/3) [MPS16] were considered to improve the fits of the observed PeV-energy events from the four-years HESE samples at IceCube.

It was shown that the current statistical power of the high-energy events at IceCube was not sufficient to confirm or exclude the leptoquarks. $\sim 10^{12}$ eV leptoquark could explain all three observations simultaneously, but is in a strong tension with other LHC data, *e.g.* monojet and dijet constraints as shown in fig. A.12.

2) R-parity violating (RPV) supersymmetry (SUSY) is a well-motivated BSM scenario since SUSY extensions of the SM provide best candidates for the new physics, and RPV for superpartners' productions and decays allows to avoid the unnatural parameter space at the Higgs sector implied by the present LHC constraints. It also could be related to the observed anomalies in muon magnetic moment, semileptonic B-meson decay and diphoton excess at LHC, LFV Higgs decay, $eejj$ and $e\nu jj$ excesses at CMS, diboson excess at ATLAS. Those effects are yet of 2σ-4σ significance, but if some of them will be confirmed, the LPV SUSY will become a serious candidate for explanation. Since no deviations from the SM were observed in the IceCube data so far, it is possible to use it to derive limits on the RPV SUSY. In fig. A.13 different experimental 1σ bounds on $|\lambda'_{11k}|$ and $|\lambda'_{12k}|$ (λ'_{ijk} RPV are couplings responsible for UHE neutrino interactions with nucleons in

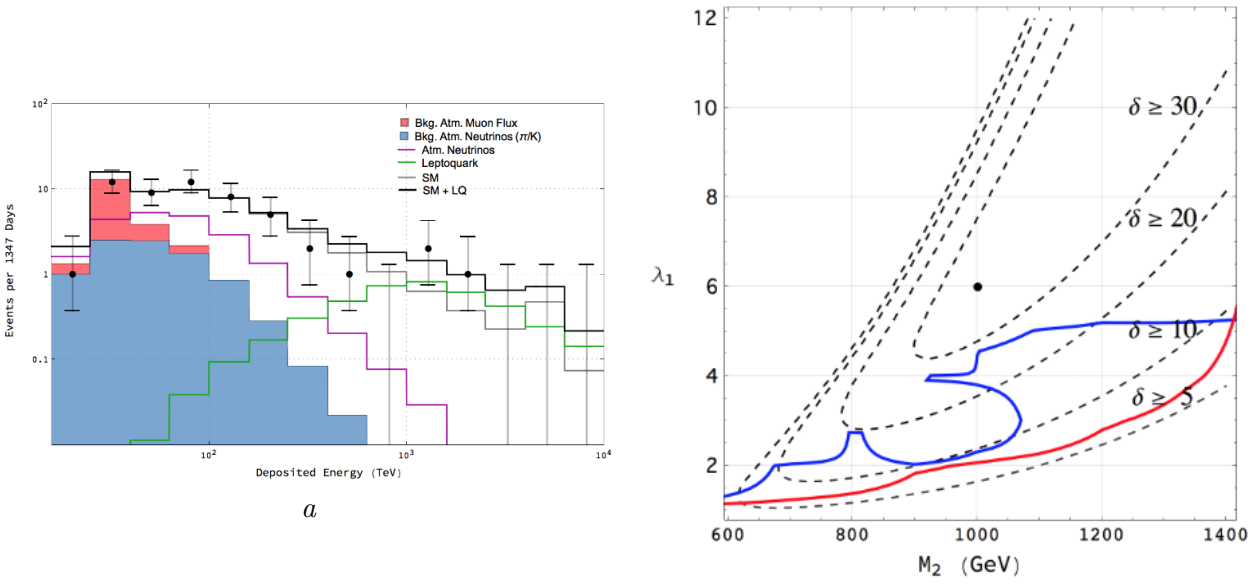

Figure A.12: *a*: Fit to 4-year HESE IceCube data using the leptoquark scalar doublet (3,2,7/6) and SM interactions (black line); *b*: Monojet (red) and Dijet (blue) LHC constraints (the parameter space above the curves is excluded) together with contours of statistic parameter $\delta(\lambda_i^2, M_{\mathrm{LQ}}) = 100 \times \frac{\chi^2_{\mathrm{SM}} - \chi^2_{\mathrm{SM+LQ}}}{\chi^2_{\mathrm{SM}}}$ representing a percentage change in χ^2 (without taking into account bins in which zero events were observed). The point indicates the parameters from the fit at the figure *a*. From [CKN18].

MSSM: $\lambda'_{ijk} L_i Q_i D^c_k$, where $i, j, k = 1, 2, 3$ are generation indices of $SU(2)_L$-doublet ($L_i \ni (\nu_i, e_i)_L$ $Q_i \ni (u_i, d_i)_L$) and $SU(2)_L$-singlet chiral superfields (D^c_i)) are compared to the ones derived from a fit to 4-years IceCube HESE data in [DGR16]. As can be seen, currently the IceCube data gave weaker constraints than the other sources of indirect constrains due to the pure statistics, but a projected limits for 4 times bigger dataset (15 years) is shown as well. Also, additional statistics can be gathered not solely from the IceCube, but from the other km^3 neutrino detectors such as a new KM3NeT project in the Mediterranean Sea or a future IceCube multi-km^3 extension - IceCube-Gen2.

3) Standard Model preserves Lorenz invariance (LI), however, in various UHE BSM theories like string theory, SUSY etc. it can be violated. Recently reported multi-messenger observation of ultra-high energy neutrinos and γs from the source TXS 0506+056 opens a way to test LI by comparing vacuum propagation speed of the neutrino and photons. The constraint on $\Delta v_{\nu\gamma}/c \sim 10^{-11}$ derived from this measurement is much stringent than from the collapse of supernova 1987A $\Delta v_{\nu\gamma}/c \lesssim 3 \times 10^{-9}$. Energy-independent velocity difference meaning violation of Lorentz invariance (LIV) would point towards new physics. Some of the theoretical frameworks suggest that LI is a symmetry holding at low-energy limit, but is violated when going to high energies, considering, for example, linear or quadratic violation. Linear violation $\Delta v \sim -E/M_1$ (for example, in some string-like models of quantum-gravitational fluctuations of space-time, where M_1 depends on parameters like string coupling, density of defects in space-time and their interaction strength with considered particles etc.) results in difference in arrival time $\Delta r = \Delta v \times D$ (D - propagation distance). The IC170922A event combined with the corresponding MAGIC γ-observations results in an estimated

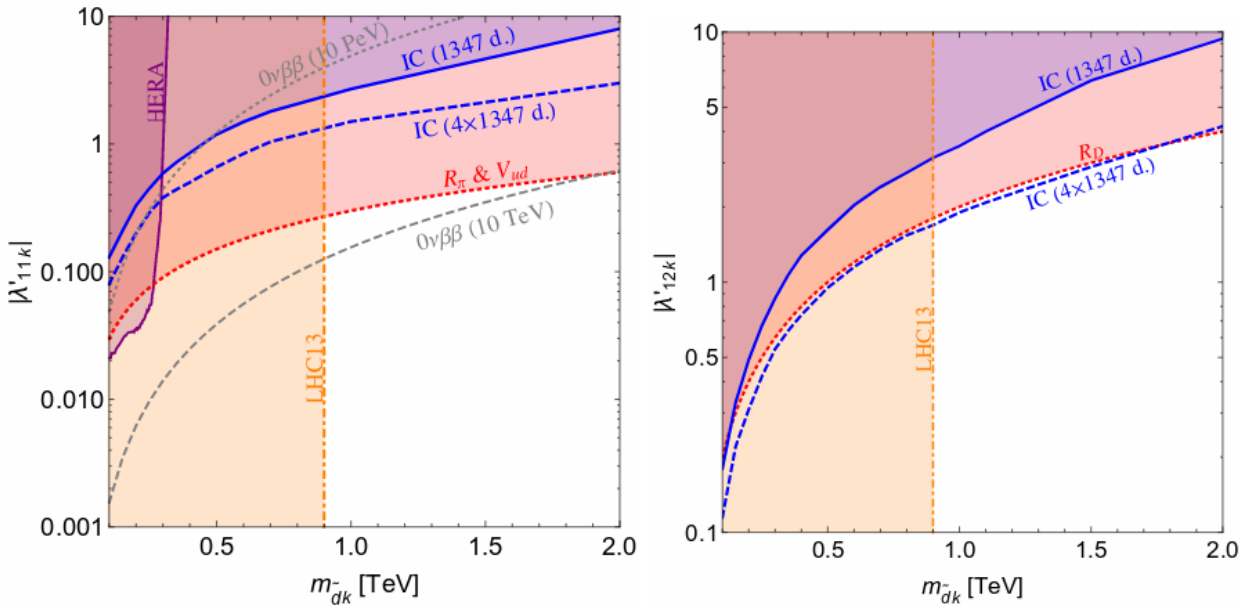

(a) $|\lambda'_{11k}|$ (b) $|\lambda'_{12k}|$

Figure A.13: Experimental bounds on the RPV couplings of electron neutrino to first and second generation of quarks: $|\lambda'_{11k}|$ (a) and $|\lambda'_{12k}|$ (b): the red dashed line for 2σ bounds from lepton universality measured by the ratio $R_\pi = \frac{\mathrm{BR}(\pi^-\to e^-\bar{\nu}_e)}{\mathrm{BR}(\pi^-\to\mu^-\bar{\nu}_\mu)}$, V_{ud} unitarity (a) and lepton universality measured by the ratio $R_D = \frac{\mathrm{BR}(Ke\nu_e)}{\mathrm{BR}(K\mu\nu_\mu)}$ (b), the orange dot-dashed line for 95% C. L. direct limits from scalar LQ search at the 1.3×10^{13} eV LHC, magenta solid line for 95 % C. L. direct limit from HERA e^-p collisions, grey dashed and grey dotted lines for 90 % C. L. $0\nu\beta\beta$ bounds with 10×10^{12} eV and 10×10^{15} eV gaugino masses correspondingly. The solid blue line indicates the 1σ constraints from the best fit to the 4-years IceCube electron neutrino data with the RPV contribution; with a four times higher statistics, the constraint (blue dashed line) gets up to 3 times stronger. From [DGR16].

sensitivity of

$$M_1 \gtrsim \frac{H_0^{-1}}{\Delta t} E \int_0^{z_{src}} \frac{1+z}{\sqrt{\Omega_\Lambda + \Omega_M (1+z)^3}} dz \approx 3\times10^{16}\mathrm{GeV} \tag{A.9}$$

which is exceeds the best current limit from SN1987a data by 6 orders of magnitude, and possible estimated future limits from terrestrial neutrino beam $M_1 \sim 4\times10^8$GeV and supernovae observations $M_1 \sim 2\times10^{13}$GeV.

In differnt models of LI, quadratic violation emerges, $\Delta v \sim -E^2/M_2$. Analogously, the IceCube+MAGIC sensitivity is

$$M_2 \gtrsim \left[\frac{3}{2}\frac{H_0^{-1}}{\Delta t} E^2 \int_0^{z_{src}} \frac{(1+z)^2}{\sqrt{\Omega_\Lambda + \Omega_M (1+z)^3}} dz\right]^{\frac{1}{2}} \approx 3\times10^{11}\mathrm{GeV} \tag{A.10}$$

comparing to $M_2 \sim 4\times10^4$GeV SN1987A sensitivity, and future estimations of $M_2 \sim 10^6$GeV from a galactic supernova and $M_2 \sim 7\times10^5$GeV from terrestrial experiments.

4) A nature of the dark energy (DE), the hypothetical type of energy introduced to explain the

observed Universe expansion, is still unknown. One of the possible candidates for the DE is vacuum: its energy density doesn't change while the Universe expand (being a cosmological constant) which gives a negative vacuum pressure. Another candidate is a new superweak scalar field (sometimes called "quintessence") which pervades the whole Universe. Such a dynamical field could couple to neutrino and by this affect its evolution equation (analogically to the MSW effect changing the oscillation probabilities). In this case, DE component in the Hamiltonian for flavor propagation will not depend on neutrino energy, while the vacuum part is inversely proportional to it, therefore, for UHEνs the effect of DE can be distinguishable with neutrino detectors. This neutrino-DE coupling leads to LIV effects. As was discussed above, IceCube gave stringent constraints on some of the LIV operators, but those are of the higher dimensions than the ones DE necessarily involve and therefore are not critical [KA18]. It shall be noted, however, that if LIV-effects will be detected, it can be still unclear whether they are due to DE or simply some intrinsic LIV in fundamental physics unrelated to DE, while DE predicts a further effect: anisotropy of flavor distribution due to the impact of neutrino propagation direction relative to our velocity wrt. to the CMB rest frame on the oscillation parameters [AKM09]. Theoretical predictions for neutrino-flavor ratios at Earth for different starting ratios at the source are shown in fig. A.14. It can be seen that ratios outside the cyan region of the fig. A.14*a* would mean BSM physics, and, in particular, the lower left region is not possible to reach even with DE-induced mixing if we assume only conventional astrophysical neutrino production (no source for ν_τ is known) and therefore would require both ν_τ-production and DE coupling. Fig. A.15 shows flavor ratios dependence on energy for different values of DE-induced CP-violating phase and maximal DE mixing angles (0.25π). It can be seen that neutrinos and antineutrinos mix differently, and such detectors as IceCube or KM3NeT have an ability to distinguish electron antineutrinos through a Glashow resonance, an so could potentially probe this effect.

A.3.3 A possible source of misinterpretation of UHEν signal as BSM

Different production mechanisms of UHEνs yield naturally different neutrino and antineutrino flavor ratios. For example, in pp collisions the flux ratios for neutrinos and antineutrinos will be the same: $(\mathrm{f}^S_{\nu_e} : \mathrm{f}^S_{\nu_\mu} : \mathrm{f}^S_{\nu_\tau}) \simeq (\mathrm{f}^S_{\bar{\nu}_e} : \mathrm{f}^S_{\bar{\nu}_\mu} : \mathrm{f}^S_{\bar{\nu}_\tau}) \simeq (\frac{1}{6} : \frac{2}{6} : 0)_S$ (or $(\frac{1}{6} : \frac{2}{6} : 0)_S$ when taking into account the difference of the lifetimes of charged pions and muons which results into production of only ν_μ and $\bar{\nu}_\mu$ at the source). This would be similar in the case of p interactions with hard or thermal γ, but in the case of sufficiently soft photon spectra the ratios for ν_μ and $\bar{\nu}_\mu$ will be asymmetric: $(\mathrm{f}^S_{\nu_e} : \mathrm{f}^S_{\nu_\mu} : \mathrm{f}^S_{\nu_\tau}) \simeq (\frac{1}{3} : \frac{1}{3} : 0)_S$ and $(\mathrm{f}^S_{\bar{\nu}_e} : \mathrm{f}^S_{\bar{\nu}_\mu} : \mathrm{f}^S_{\bar{\nu}_\tau}) \simeq (0 : \frac{1}{3} : 0)_S$. Neutrino are oscillating during their propagation to the earth, and for the neutrino and antineutrino fluxes registered at Earth we can expect to be equal if they were equal, but not if they were unequal at the source. Usually, neutrino and antineutrino fluxes are assumed to be equal, and expected regions of flavor ratios at the Earth are shown at fig. A.16. Current IceCube data (yet statistically poor for the moment) seem to point outside of these regions [Aar+15a], [Aar+15b], which under the equal fluxes assumption would require a new physics explanation. Some BSM-scenarios, such as neutrino decay, Pseudo-Dirac neutrino, neutrino self-scattering, were considered in detail with regard of the sensitivity of the foreplanned next-generation neutrino detectors in [SM16].

However, in [NPZF16] it was investigated whether the same signal could be produced by unequal

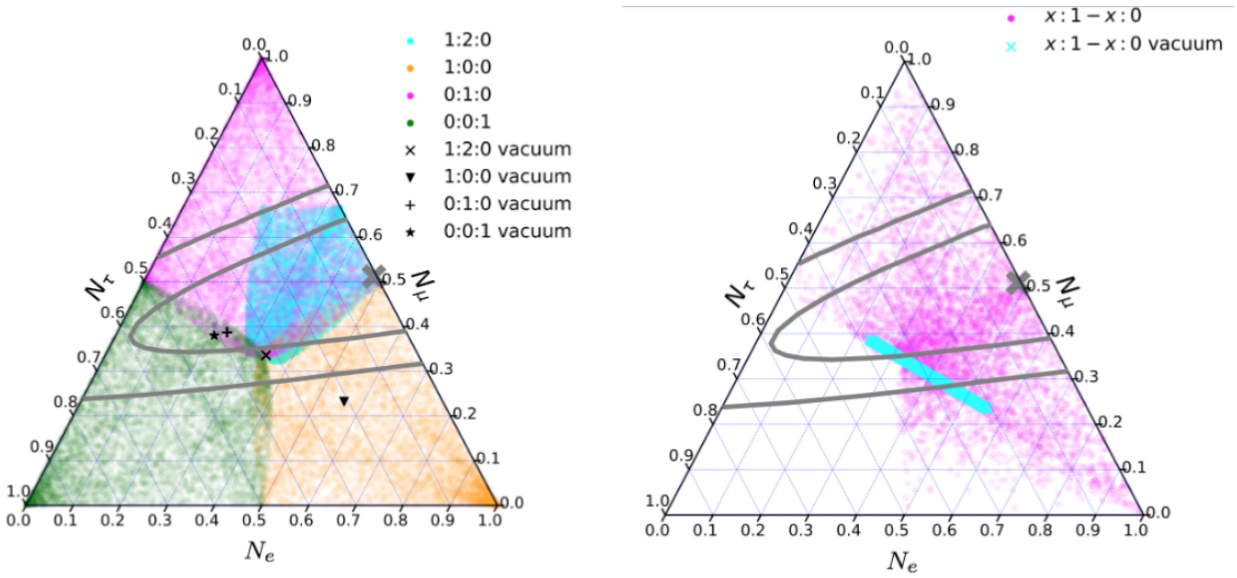

a *b*

Figure A.14: Neutrino flavor ratios at Earth *a*: for different flavor ratios of the three neutrinos at the source and *b*:for different electron and muon ratios (assuming no tau is produced) at the source. A full variation over DE mixing angles is shown with colored regions on *a* and with magenta region on *b*. The black symbols on *a* mark the corresponding expected ratios for the vacuum mixing. The cyan region on *b* corresponds to vacuum oscillations. 60% and 95% confidence region together with the best-fit point for the IceCube data [Aar+15a] are shown as the solid grey lines and the grey cross correspondingly. From [KA18].

neutrino-antineutrino fluxes, thus creating an ambiguity and possible misinterpretation of the experimental results due to wrong flux ratio assumptions, by assuming some flux distribution at the source, derivation of the incoming fluxes at Earth and prediction of an observed number of tracks and cascades at the IceCube detector and fitting the simulated data with a wrong assumption. Fig. A.17 shows allowed regions for combined $(\nu_e + \bar{\nu_e}, \nu_\mu + \bar{\nu_\mu}, \nu_\tau + \bar{\nu_\tau})$ flavor ratios f_{ν_e}, f_{ν_μ}, f_{ν_τ} obtained from a mock-data generated with an assumption of unequal $\nu\bar{\nu}$ fluxes generated via $p\gamma$ scenario, $(\mathrm{f}^S_{\nu_e} : \mathrm{f}^S_{\nu_\mu} : \mathrm{f}^S_{\nu_\tau}) \simeq (\frac{1}{3} : \frac{1}{3} : 0)_S$ and $(\mathrm{f}^S_{\bar{\nu}_e} : \mathrm{f}^S_{\bar{\nu}_\mu} : \mathrm{f}^S_{\bar{\nu}_\tau}) \simeq (0 : \frac{1}{3} : 0)_S$, and propagated to the Earth and fit with an assumption of equal $\nu\bar{\nu}$ fluxes at the Earth. It can be distinctly seen that the best fit point falls outside the standard region shown in yellow for various high energy neutrino production scenarios where ν_τ is not produced at the source and currently allowed 3σ oscillation region from [Ber+15]. Also, fig. A.18 demonstrates a result of the same procedure but assuming different $\nu\bar{\nu}$ flavor distribution at the source: $(\mathrm{f}^S_{\nu_e} : \mathrm{f}^S_{\nu_\mu} : \mathrm{f}^S_{\nu_\tau}) = (0 : 0.3 : 0)_S$ and $(\mathrm{f}^S_{\bar{\nu}_e} : \mathrm{f}^S_{\bar{\nu}_\mu} : \mathrm{f}^S_{\bar{\nu}_\tau}) = (0.3 : 0.4 : 0)_S$, which can be realized by a certain combination of a pion decay with muon damp in *pp* scenario source and neutron decay source. As can be seen, the result $(f^{\oplus F}_{\nu_e} : f^{\oplus F}_{\nu_\mu} : f^{\oplus F}_{\nu_\tau}) = (0.52 : 0.41 : 0.07)$ is compatible with the IceCube fit $((f^{\oplus}_{\nu_e} : f^{\oplus}_{\nu_\mu} : f^{\oplus}_{\nu_\tau}) \simeq (0.5 : 0.5 : 0))$ [Aar+15a], which means that the IceCube observations can be explained within the SM as long as $\nu\bar{\nu}$ fluxes are not constrained to be equal.

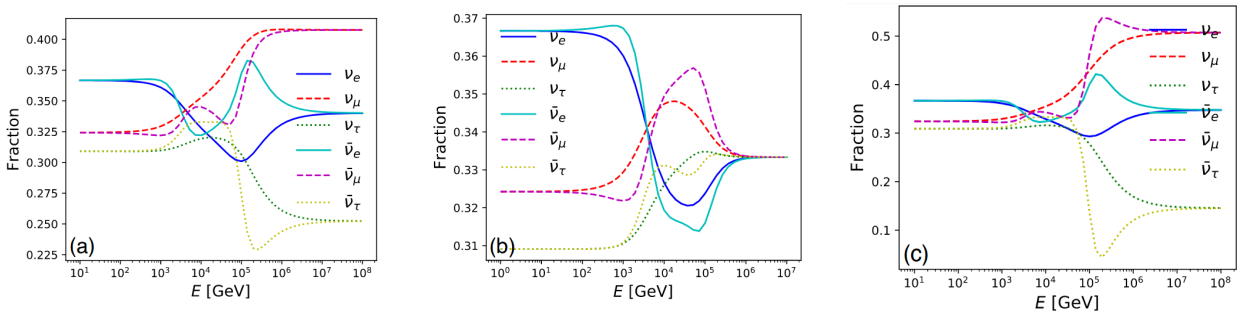

Figure A.15: (Anti)neutrino flavor ratio depending on energy for DE-induced oscillation angles θ_{12}, θ_{13}, θ_{23}=0.25π, the mass differences $m_{eff21} = \frac{1}{2}m_{eff31}$ =10^{-26} GeV and for different DE-induced CP-violating phase: a) 0.25π; b) 0.5π; c) 0. From [KA18].

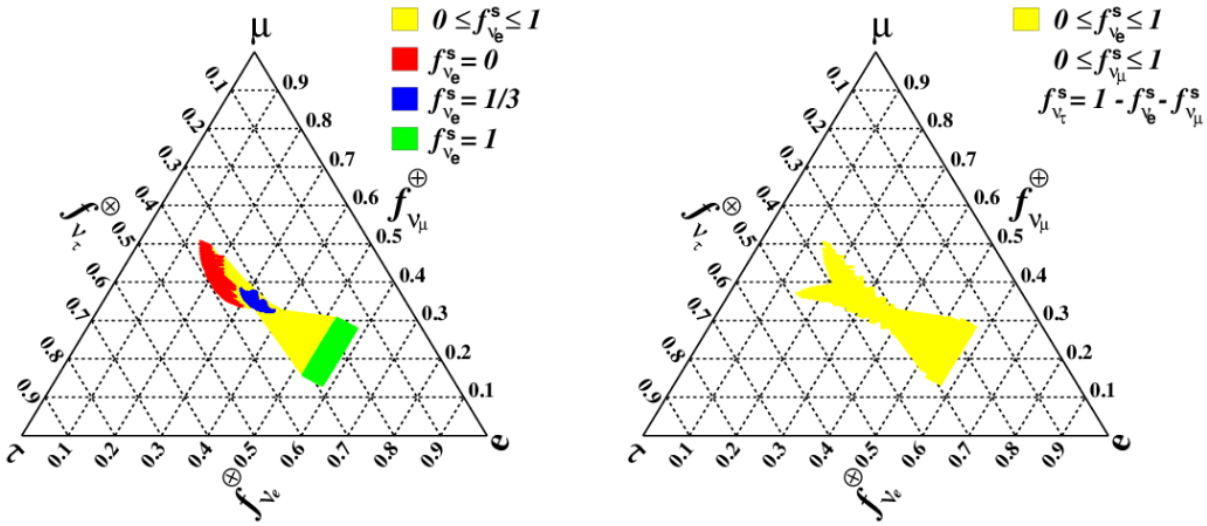

Figure A.16: Currently allowed regions for combined $\nu\bar{\nu}$ fluxes $f^{\oplus}_{\nu_e}$, $f^{\oplus}_{\nu_\mu}$, $f^{\oplus}_{\nu_\tau}$ at Earth for different neutrino production scenarios with various $f^S_{\nu_e}$ and with (left) or without (right) ν_τ being allowed to be produced at the source. From [NPZF16].

A.4 Conclusions

Ultra-high energy neutrinos, which were observed by IceCube and whose origin is still unknown, are a new and perspective tool for astroparticle investigations. Although investigation of this part of neutrino spectrum is complicated by extremely small particle fluxes and, as a consequence, poor experimental statistics, with more years of data taking and more detectors (such as the IceCube successors, IceCube-Gen2 and KM3NeT) accuracy of the current data fits is expected to increase significantly. UHEνs allow to study particle interactions on the scales, which greatly surpass those which can be reached by existing or even planned accelerators. They could help in resolving the mystery the ultra-high energy cosmic rays, one of the main problems of the contemporary particle physics, since they point directly and up to the cores of UHECR sources over cosmological distances with GZK-length precision without being essentially extinguished unlike the other particles and can reveal even optically invisible/non-radiant objects. Probably, their origin is connected to manifestations of beyond the Standard Model physics. In this referative review work, I have payed special attention to various BSM mechanisms which could involve UHEνs that the IceCube is

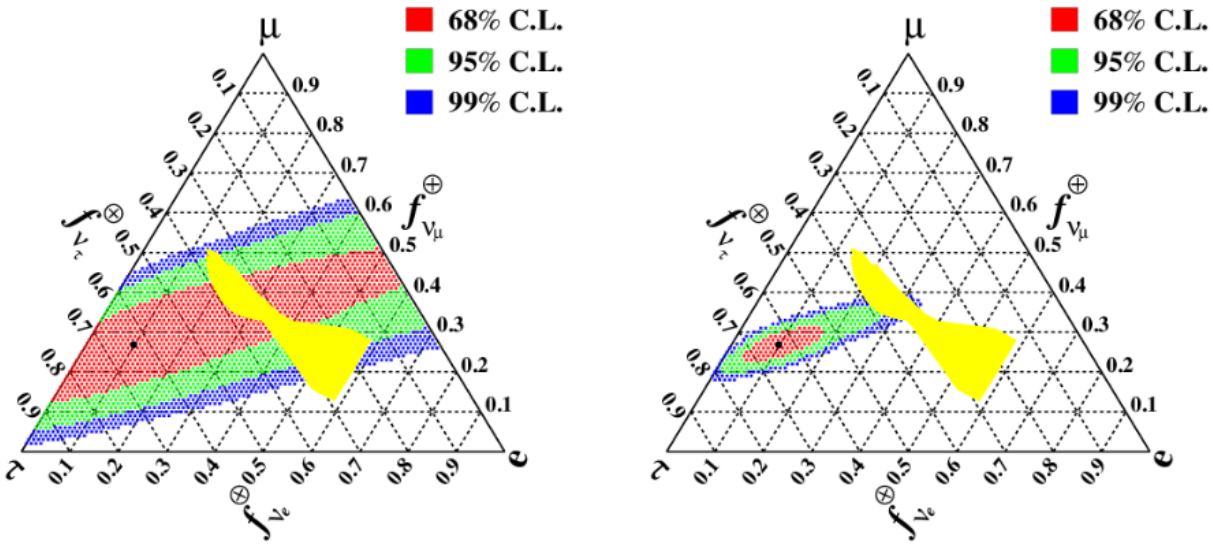

Figure A.17: Best fit with an assumption of equal $\nu\bar{\nu}$ flux at Earth of the simulated data from $p\gamma$ production mechanism with $(\mathrm{f}^S_{\nu_e} : \mathrm{f}^S_{\nu_\mu} : \mathrm{f}^S_{\nu_\tau}) \simeq (\frac{1}{3} : \frac{1}{3} : 0)_S$ and $(\mathrm{f}^S_{\bar{\nu}_e} : \mathrm{f}^S_{\bar{\nu}_\mu} : \mathrm{f}^S_{\bar{\nu}_\tau}) \simeq (0 : \frac{1}{3} : 0)_S$ and oscillation parameters $\sin^2\theta_{12} = 0.31$, $\sin^2\theta_{23} = 0.60$, $\sin^2\theta_{13} = 0.02$, $\delta = 3\pi/2$ denoted with a black dot and 68% (red), 95% (green) and 99% (blue) C. L. for different astrophysical neutrino statistics: 180 (left) and 1800 (right) events. From [NPZF16].

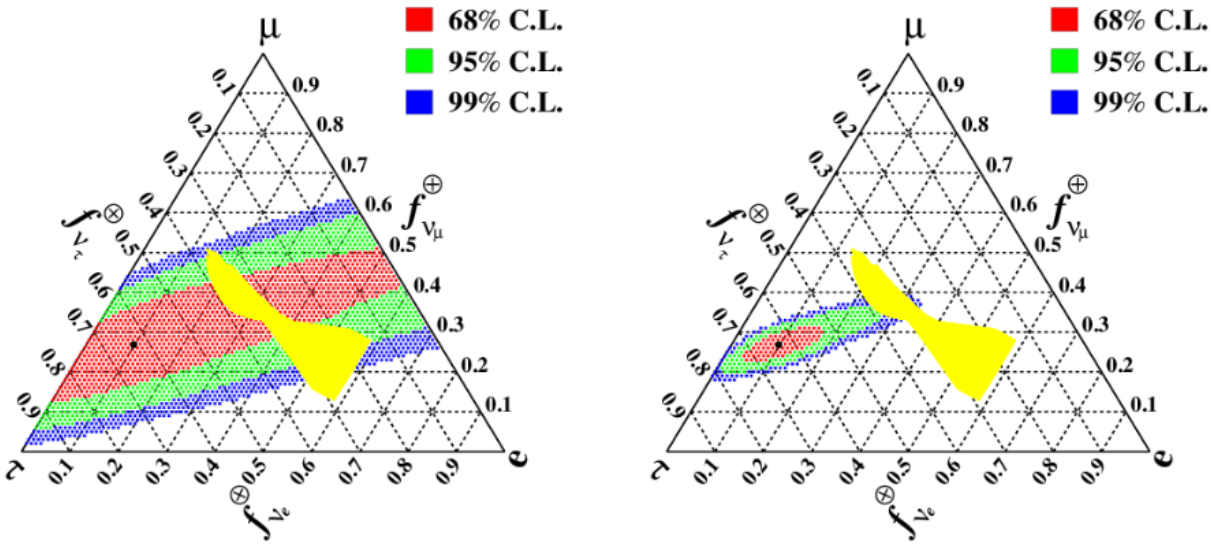

Figure A.18: Best fit with an assumption of equal $\nu\bar{\nu}$ flux at Earth of the simulated data from a combined-source production mechanism with $(\mathrm{f}^S_{\nu_e} : \mathrm{f}^S_{\nu_\mu} : \mathrm{f}^S_{\nu_\tau}) \simeq (0 : 0.3 : 0)_S$ and $(\mathrm{f}^S_{\bar{\nu}_e} : \mathrm{f}^S_{\bar{\nu}_\mu} : \mathrm{f}^S_{\bar{\nu}_\tau}) \simeq (0.3 : 0.4 : 0)_S$ and oscillation parameters $\sin^2\theta_{12} = 0.31$, $\sin^2\theta_{23} = 0.60$, $\sin^2\theta_{13} = 0.02$, $\delta = 3\pi/2$ denoted with a black dot and 68% (red), 95% (green) and 99% (blue) C. L. for different astrophysical neutrino statistics: 180 (left) and 1800 (right) events. From [NPZF16].

detecting. There is hope that in the upcoming years more UHEν data and analysis will shed light on many problems considered here.

Appendix B

Determination of the offests of the rotatable polarizer and compensator of the CKrS ellipsometry set-up

B.1 Polarizer offset

For this measurement, the rotatable polarizer of the ellipsometry set-up, an additional fixed polarizer and a photodiode detector not belonging to the ellipsometry set-up were set (in this order) on the optical rail of the ellipsometry set-up after the ellipsometry quarter-wave plate (after which a circularly-polarized light comes out). The rotatable compensator was removed from the set-up for this measurement.

The measurement was done in two steps: 1) the rotatable polarizer was turned in steps starting from zero position and the intensity after the fixed polarizer was measured by the detector; 2) the fixed polarizer was flipped by 180° around the vertical axis and the procedure was repeated. In both cases the range from 0° to 200° was scanned in 5° steps. From both measurements, angular position of intensity minimum (corresponding to the polarizers having their polarization axes crossed under 90°) was evaluated from fitting data points with Malus's law $I(P) = a\cos^2(P + b) + c$ (where P is the polarizer angle, a, b, c are constants) and finding the local minimum of the fit function. Results are presented on the fig. B.1:

This allows to determine offsets of the polarizers. The fixed polarizer has an offset of ΔP_1 w.r.t. the 0° position on the scale of the rotatable polarizer. To get a minimum of intensity after the fixed polarizer, the axis of the rotatable polarizer, which has an offset of ΔP_2 with respect to the 0° position, has to have 90° w.r.t. the axis of the fixed polarizer, as shown on the fig. B.2. With P^1_{min} and P^2_{min} being measured angles of the rotatable polarizer corresponding to the minimum of intensity for both sides of the fixed polarizer, this leads to the following equations:

$$90^\circ + \Delta P_1 = P^1_{min} + \Delta P_2; \tag{B.1}$$

$$90^\circ - \Delta P_1 = P^2_{min} + \Delta P_2, \tag{B.2}$$

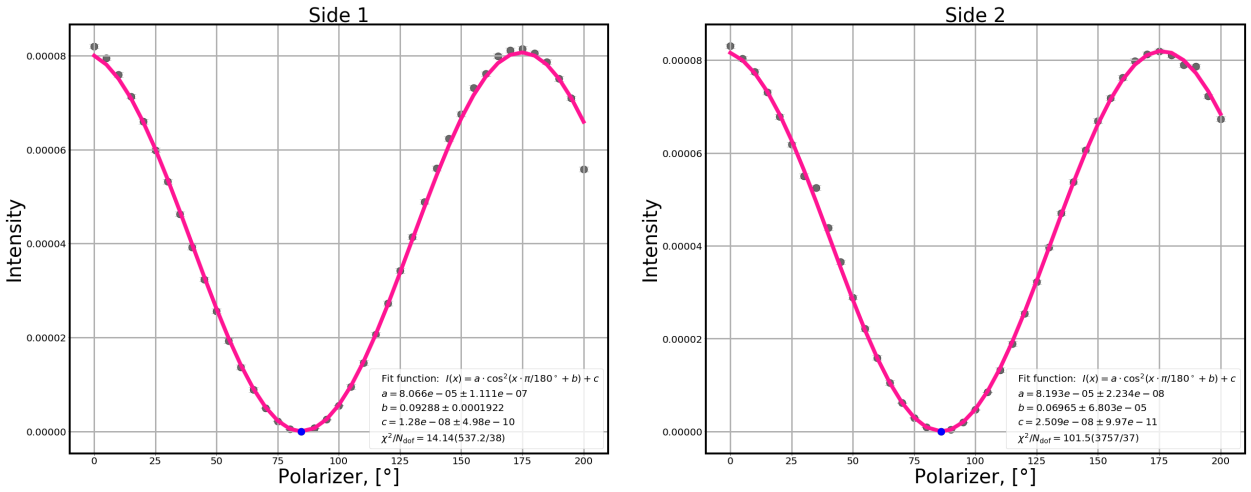

a b

Figure B.1: Measurement of intensity depending on the angle of the rotatable polarizer and fit with Malus's law for one side (a) and the opposite side (b) of the fixed polarizer. Blue dots indicate position of the minimum of the fit function: 84.68° and 86.01° for side 1 and side 2 respectively.

which lead to

$$\Delta P_1 = \frac{P^1_{min} - P^2_{min}}{2} = \frac{84.68^\circ - 86.01^\circ}{2} = 0.665^\circ \tag{B.3}$$

and

$$\Delta P_2 = \frac{180^\circ - 84.68^\circ - 86.01^\circ}{2} = 4.655^\circ. \tag{B.4}$$

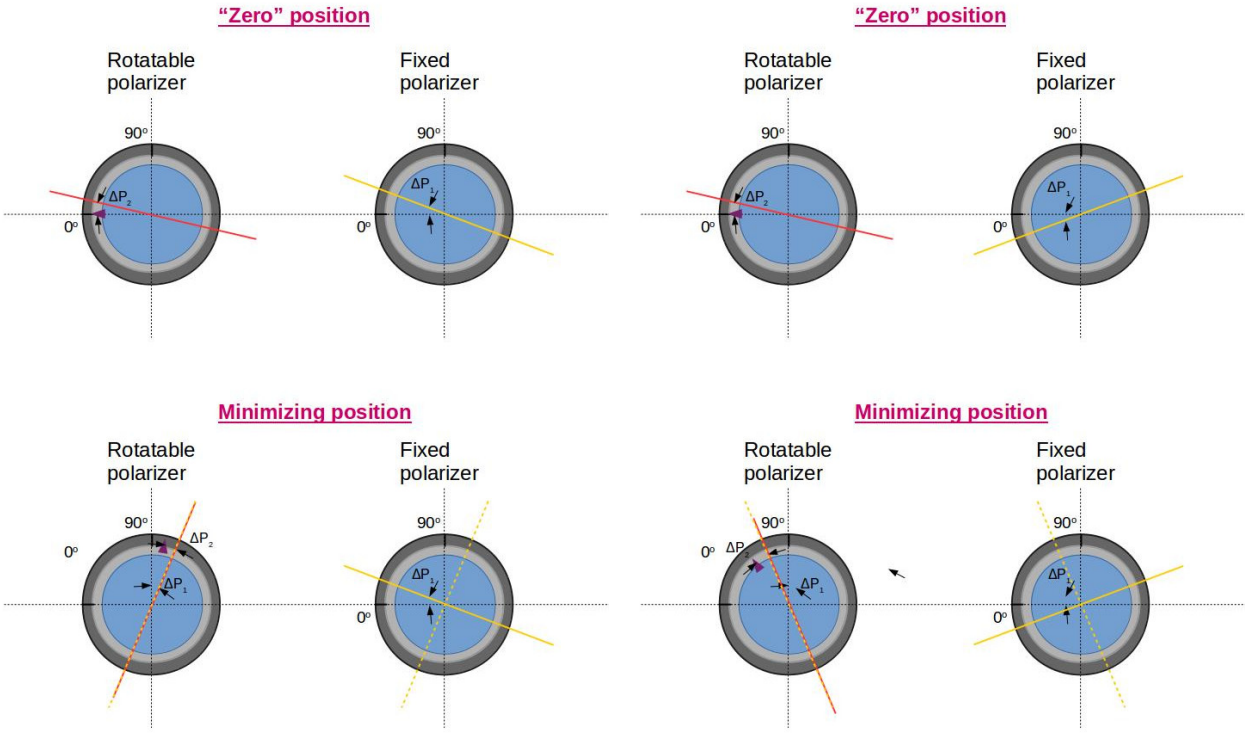

a b

Figure B.2: Schematic drawing of the axes orientation of the polarizers for one side(a) and the opposite side (b) of the fixed polarizer. Red and yellow solid lines indicate actual orientations of the axes of the rotatable and the fixed polarizers correspondingly. Yellow dashed line indicate the orientation, perpendicular to the actual orientation of the fixed polarizer. Violet arrow is a mark on the polarizer "holding" (light-grey ring), pointing to a measured angle value on the "scale" (dark-grey ring).

B.2 Compensator offset

To check the offset of the compensator, the positions of the polarizers from the previous measurement are swapped and the compensator (belonging to the ellipsometry set-up) is installed between them. In this measurement, the compensator angle C is changed in 20° steps from 0° to 120°, and for each step, we measure the intensity I for different rotatable polarizer angle P, which has the following dependence on the angles of the rotatable polarizer and compensator (a derivation is presented in the next section):

$$I(P,C) = \frac{1}{2} I_0 (1 + \cos^2(2C)\cos(2P) + \frac{1}{2}\sin(4C)\sin(2P)). \tag{B.5}$$

The amplitude of the intensity oscillations with the rotatable polarizer angle is minimal (equal to zero in an ideal case) when the axis of the compensator is turned by ±45° with respect to the fixed polarizer axis (which in the ideal case would result into a circularly polarized light after the compensator and therefore constant intensity with the rotatable polarizer orientation). This is illustrated on the fig. B.3. Therefore, measured points are fitted with (B.5) for a certain compensator angle (see fig.B.4) and the corresponding amplitudes are determined. The resulting experimental dependence of the amplitude on compensator angle is then fitted with $\Delta I(C) = I_{max}(C) - I_{min}(C)$, where $I_{max}(C)$ and $I_{min}(C)$ are minima and maxima of the (B.5) for a given compensator angle C (see fig. B.5). Compensator angle $C_{min} = 22.385°$, corresponding to the minimum of this fit function, is the position at which the compensator axis has an angle of ±45° w.r.t. the axis of the fixed polarizer.

This allows to determine an offset of the compensator, since it satisfies the following equation:

$$\Delta P_1 \pm 45° = C_{min} + \Delta C, \tag{B.6}$$

which results in $C_{min} = \Delta P_1 \pm 45° - C_{min} = 0.665° \pm 45° - 22.385 = 23.28°$ or $-66.72°$.

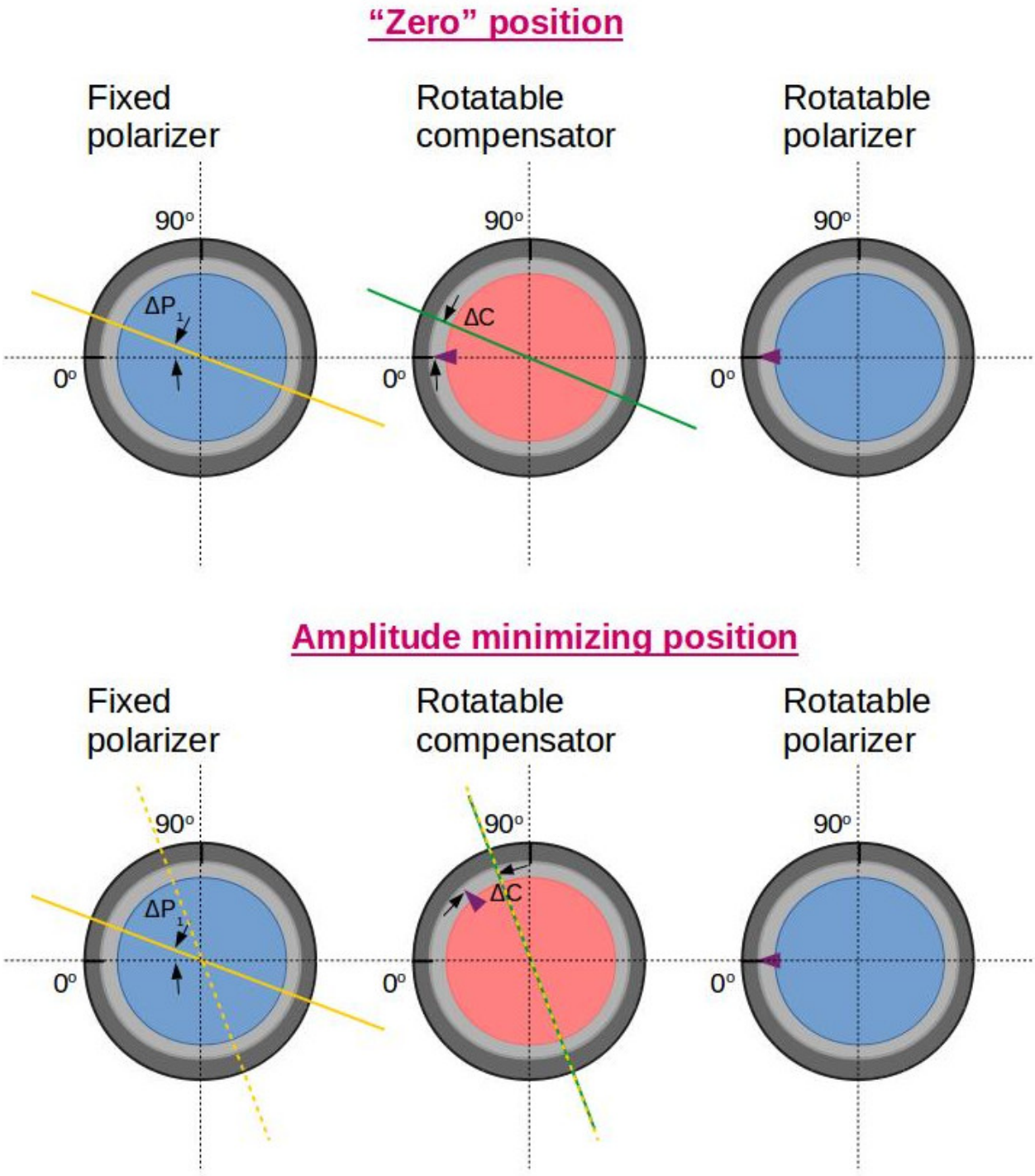

Figure B.3: Schematic drawing of the measurement set-up of the polarizers and the compensator and axes orientation of the fixed polarizer and the compensator. Green and yellow solid lines indicate actual orientations of the optical axes of the rotatable compensator and the fixed polarizer correspondingly. Yellow dashed line indicates an orientation which has 45° to the actual orientation of the fixed polarizer. Violet arrow is a mark on the compensator "holding" (light-grey ring), pointing to a measured angle value on the "scale" (dark-grey ring).

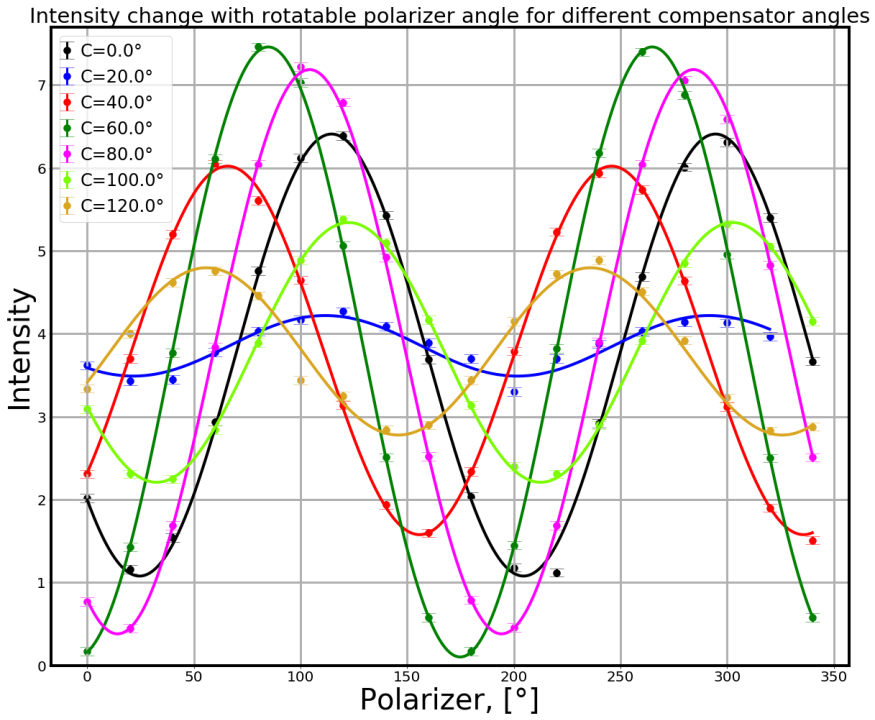

Figure B.4: Measured dependencies (dots) and fits with (B.5) law (solid lines) of the intensity on the rotatable polarizer angles for different compensator angles.

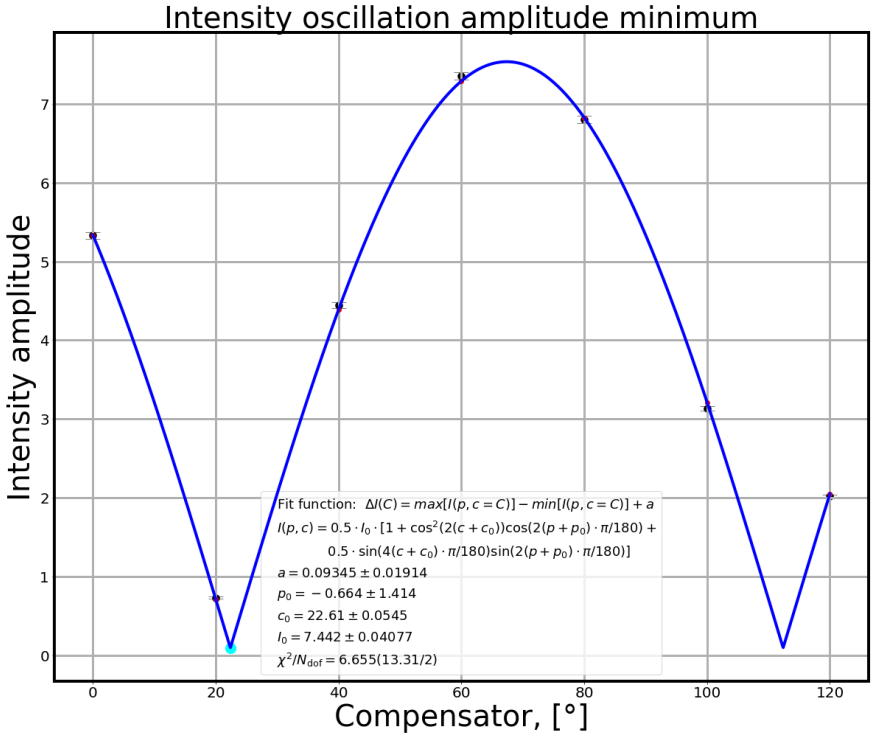

Figure B.5: Measurement (black dots connected by a red line) and fit (blue line) of the intensity amplitude dependence on the compensator angle. The cyan dot indicates the position of the amplitude minimum C_{min} at 22.385°.

B.3 Derivation of out-coming intensity dependence on polarizer and compensator angles in the set-up for compensator offset measurement

Alternatively to eq. (3.6), an electromagnetic harmonic wave lying in xy-plane and propagating in z-direction, can be expressed as

$$\vec{E}(z,t) = E_x\hat{x} \cdot e^{i(\omega t - k_\omega z)} + E_y\hat{y} \cdot e^{i(\omega t - k_\omega z + \Gamma)}. \tag{B.7}$$

The polarization of light is defined by the phas Γ and E_x and E_y components of the light. If $\Gamma = \pm\frac{\pi}{2}$ and $E_x = E_y$ the wave is circularly polarized.

To derive the outcoming intensity for the system described in the previous section, the Jones calculus will be applied. In it, polarization of light is described by 2×1 matrices (Jones vectors). The general form of a Jones vector is $\begin{bmatrix} E_x \\ E_y \end{bmatrix}$. Optical components in their turn are expressed by 2×2 Jones matrices. The polarization of transmitted light is obtained by sequential multiplication the Jones matrices of the components and the Jones vector of the incoming light.

Let us consider a system consisting of a fixed linear polarizer whose transmission axis is aligned along the x-axis, a rotatable compensator (a quarter-wave plate) with angle C to the x-axis and the rotatable linear polarizer with a transmission axis at the angle P to the x axis.

For such a system, the Jones matrix will be

$$H = T_3T_2T_1, \tag{B.8}$$

where T_1 is the Jones matrix of the polarizer

$$T_1 = \begin{bmatrix} 1 & 0 \\ 0 & 0 \end{bmatrix}. \tag{B.9}$$

The Jones matrix of the rotatable polarizer can be derived by considering the cases of full and null transmissions. The beam incident on the polarizer can be expressed as $\begin{bmatrix} \cos\Phi \\ \sin\Phi \end{bmatrix}$ and the Jones matrix of the compensator as

$$T_3 = \begin{bmatrix} a & b \\ c & d \end{bmatrix}. \tag{B.10}$$

The maximal transmission will be in case $P = \Phi$:

$$\begin{bmatrix} a & b \\ c & d \end{bmatrix} \begin{bmatrix} \cos P \\ \sin P \end{bmatrix} = \begin{bmatrix} \cos P \\ \sin P \end{bmatrix}. \tag{B.11}$$

In case of the orthogonal incidence ($\Phi = P + \frac{\pi}{2}$), the transmission will be zero:

$$\begin{bmatrix} a & b \\ c & d \end{bmatrix} \begin{bmatrix} \cos(P + \frac{\pi}{2}) \\ \sin(P + \frac{\pi}{2}) \end{bmatrix} = \begin{bmatrix} 0 \\ 0 \end{bmatrix}. \tag{B.12}$$

Solving these two equations one gets

$$T_3 = \begin{bmatrix} \cos^2 P & \sin P \cos P \\ \sin P \cos P & \sin^2 P \end{bmatrix}. \tag{B.13}$$

The Jones matrix for the quarter-wave plate is

$$T_2 = R(C)T_2'R(-C), \tag{B.14}$$

where

$$T_2' = \begin{bmatrix} 1 & 0 \\ 0 & e^{-i\Gamma} \end{bmatrix} \tag{B.15}$$

and

$$R(C) = \begin{bmatrix} \cos C & -\sin C \\ \sin C & \cos C \end{bmatrix}. \tag{B.16}$$

Therefore

$$T_2 = \begin{bmatrix} \cos C & -\sin C \\ \sin C & \cos C \end{bmatrix} \begin{bmatrix} 1 & 0 \\ 0 & e^{-i\Gamma} \end{bmatrix} \begin{bmatrix} \cos C & \sin C \\ -\sin C & \cos C \end{bmatrix}. \tag{B.17}$$

Combining equations (B.8), (B.9), (B.13), (B.17), one gets

$$H = \left(\cos(C - P)\cos C + \sin(C - P)e^{-i\Gamma}\sin C\right) \begin{bmatrix} \cos P & 0 \\ \sin P & 0 \end{bmatrix}. \tag{B.18}$$

The transmitted light can be represented as

$$\vec{J_2} = H\vec{J_1}, \tag{B.19}$$

where $\vec{J_1} = \begin{bmatrix} 1 \\ 0 \end{bmatrix}$ is the vector of the light incident on the system. Then, substituting expression (B.18), one gets

$$\vec{J_2} = \left(\cos(C - P)\cos C + \sin(C - P)e^{-i\Gamma}\sin C\right) \begin{bmatrix} \cos P \\ \sin P \end{bmatrix}. \tag{B.20}$$

The intencity of the incident light characterized by electric field vector $\vec{E}_0$ is given by

$$I_0 = \frac{\vec{E}_0 \cdot \vec{E^*}_0}{2} = \frac{E_0^2}{2} \text{ with } \vec{E}_0 = E_0\hat{x}. \tag{B.21}$$

and the electric field of the transmitted light is $\vec{E} = E_0\vec{J}_2$. Then the transmitted intensity is

$$\begin{aligned} I = & \frac{\vec{E} \cdot \vec{E^*}}{2} = \frac{E_0\vec{J}_2 \cdot E_0\vec{J^*}_2}{2} = I_0\vec{J}_2 \cdot \vec{J^*}_2 = \dots \\ = & I_0 \left(\cos^2 C \cos^2(C-P) + \sin^2 C \sin^2(C-P) + \frac{\sin(2C)\sin(2C-2P)}{2} \cos\Gamma \right) = \dots \\ = & \frac{1}{2} I_0 \left(1 + \left[\cos^2(2C) + \cos\Gamma \sin^2(2C) \right] \cos(2P) + \sin^2\left(\frac{\Gamma}{2}\right) \sin(4C)\sin(2P) \right) \end{aligned} \tag{B.22}$$

which in the case of the circularly polarized incident light ($\Gamma = \pm\frac{\pi}{2}$) gives

$$I = \frac{1}{2} I_0 \left(1 + \cos^2(2C)\cos(2P) + \frac{1}{2}\sin(4C)\sin(2P) \right) \tag{B.23}$$

which is the equation (B.5) from the previous section.

Bibliography

[Aar+13] M. G. Aartsen et al. "First Observation of PeV-Energy Neutrinos with IceCube". In: *Phys. Rev. Lett.* 111 (2 2013), p. 021103. DOI: 10.1103/PhysRevLett.111.021103. URL: https://link.aps.org/doi/10.1103/PhysRevLett.111.021103.

[Aar+15a] M. G. Aartsen et al. "A combined maximum-likelihood analysis of the high-energy astrophysical neutrino flux measured with IceCube". In: *Astrophys. J.* 809.1 (2015), p. 98. DOI: 10.1088/0004-637X/809/1/98. arXiv: 1507.03991 [astro-ph.HE].

[Aar+15b] M. G. Aartsen et al. "Flavor Ratio of Astrophysical Neutrinos above 35 TeV in IceCube". In: *Phys. Rev. Lett.* 114.17 (2015), p. 171102. DOI: 10.1103/PhysRevLett.114.171102. arXiv: 1502.03376 [astro-ph.HE].

[Aar+15c] M. G. Aartsen et al. "Search for Dark Matter Annihilation in the Galactic Center with IceCube-79". In: *Eur. Phys. J.* C75.10 (2015), p. 492. DOI: 10.1140/epjc/s10052-015-3713-1. arXiv: 1505.07259 [astro-ph.HE].

[Aar+17] M.G. Aartsen et al. "The IceCube Neutrino Observatory: instrumentation and online systems". In: *Journal of Instrumentation* 12.03 (2017), P03012–P03012. DOI: 10.1088/1748-0221/12/03/p03012. URL: https://doi.org/10.1088%2F1748-0221%2F12%2F03%2Fp03012.

[Aar+18a] M. G. Aartsen et al. "Multimessenger observations of a flaring blazar coincident with high-energy neutrino IceCube-170922A". In: *Science* 361.6398 (2018), eaat1378. DOI: 10.1126/science.aat1378. arXiv: 1807.08816 [astro-ph.HE].

[Aar+18b] M. G. Aartsen et al. "Neutrino emission from the direction of the blazar TXS 0506+056 prior to the IceCube-170922A alert". In: *Science* 361.6398 (2018), pp. 147–151. DOI: 10.1126/science.aat2890. arXiv: 1807.08794 [astro-ph.HE].

[Aar+19] M. G. Aartsen et al. "Detection of the Temporal Variation of the Sun's Cosmic Ray Shadow with the IceCube Detector". In: *The Astrophysical Journal* 872.2 (2019), p. 133. DOI: 10.3847/1538-4357/aaffd1. URL: https://doi.org/10.3847%2F1538-4357%2Faaffd1.

[AB77] R.M.A. Azzam and N.M. Bashara. *Ellipsometry and polarized light*. North-Holland personal library. North-Holland Pub. Co., 1977. ISBN: 9780444870162. URL: https://books.google.de/books?id=1_4uAQAAIAAJ.

[Agh+18] N. Aghanim et al. "Planck 2018 results. VI. Cosmological parameters". In: (2018). arXiv: 1807.06209 [astro-ph.CO].

[Ago+18] M. Agostini et al. "Improved Limit on Neutrinoless Double-β Decay of ^{76}Ge from GERDA Phase II". In: *Phys. Rev. Lett.* 120 (13 2018), p. 132503. DOI: 10.1103/PhysRevLett.120.132503. URL: https://link.aps.org/doi/10.1103/PhysRevLett.120.132503.

[AH15] Markus Ahlers and Francis Halzen. "High-energy cosmic neutrino puzzle: a review". In: *Reports on Progress in Physics* 78.12 (2015), p. 126901. DOI: 10.1088/0034-4885/78/12/126901. URL: https://doi.org/10.1088%2F0034-4885%2F78%2F12%2F126901.

[AH18] Markus Ahlers and Francis Halzen. "Opening a New Window onto the Universe with IceCube". In: *Prog. Part. Nucl. Phys.* 102 (2018), pp. 73–88. DOI: 10.1016/j.ppnp.2018.05.001. arXiv: 1805.11112 [astro-ph.HE].

[Ahl15] Markus Ahlers. "High-energy Cosmogenic Neutrinos". In: *Physics Procedia* 61 (2015). 13th International Conference on Topics in Astroparticle and Underground Physics, TAUP 2013, pp. 392 –398. ISSN: 1875-3892. DOI: https://doi.org/10.1016/j.phpro.2014.12.080. URL: http://www.sciencedirect.com/science/article/pii/S1875389214006932.

[Ahm+02] Q. R. Ahmad et al. "Direct Evidence for Neutrino Flavor Transformation from Neutral-Current Interactions in the Sudbury Neutrino Observatory". In: *Phys. Rev. Lett.* 89 (1 2002), p. 011301. DOI: 10.1103/PhysRevLett.89.011301. URL: https://link.aps.org/doi/10.1103/PhysRevLett.89.011301.

[Ahm+04] S. N. Ahmed et al. "Measurement of the Total Active ^{8}B Solar Neutrino Flux at the Sudbury Neutrino Observatory with Enhanced Neutral Current Sensitivity". In: *Phys. Rev. Lett.* 92 (18 2004), p. 181301. DOI: 10.1103/PhysRevLett.92.181301. URL: https://link.aps.org/doi/10.1103/PhysRevLett.92.181301.

[Ake+19a] M. Aker et al. *An improved upper limit on the neutrino mass from a direct kinematic method by KATRIN*. 2019. arXiv: 1909.06048 [hep-ex].

[Ake+19b] M. Aker et al. *Suppression of Penning discharges between the KATRIN spectrometers*. 2019. arXiv: 1911.09633 [physics.ins-det].

[AKM09] Shin'ichiro Ando, Marc Kamionkowski, and Irina Mocioiu. "Neutrino Oscillations, Lorentz/CPT Violation, and Dark Energy". In: *Phys. Rev.* D80 (2009), p. 123522. DOI: 10.1103/PhysRevD.80.123522. arXiv: 0910.4391 [hep-ph].

[Alb+18] J. B. Albert et al. "Search for Neutrinoless Double-Beta Decay with the Upgraded EXO-200 Detector". In: *Phys. Rev. Lett.* 120 (7 2018), p. 072701. DOI: 10.1103/PhysRevLett.120.072701. URL: https://link.aps.org/doi/10.1103/PhysRevLett.120.072701.

[Alp+15] B. Alpert et al. "HOLMES". In: *The European Physical Journal C* 75.3 (2015), p. 112. ISSN: 1434-6052. DOI: 10.1140/epjc/s10052-015-3329-5. URL: https://doi.org/10.1140/epjc/s10052-015-3329-5.

[Alt+19] K. Altenmüller et al. "Muon-induced background in the KATRIN main spectrometer". In: *Astroparticle Physics* 108 (2019), pp. 40 –49. ISSN: 0927-6505. DOI: https://doi.org/10.1016/j.astropartphys.2019.01.003. URL: http://www.sciencedirect.com/science/article/pii/S0927650518302597.

[Ans+18] S. Ansoldi et al. "The blazar TXS 0506+056 associated with a high-energy neutrino: insights into extragalactic jets and cosmic ray acceleration". In: *Astrophys. J. Lett.* (2018). [Astrophys. J.863,L10(2018)]. DOI: 10.3847/2041-8213/aad083. arXiv: 1807.04300 [astro-ph.HE].

[Are+16] M. Arenz et al. "Commissioning of the vacuum system of the KATRIN Main Spectrometer". In: *Journal of Instrumentation* 11.04 (2016), P04011–P04011. DOI: 10.1088/1748-0221/11/04/p04011. URL: https://doi.org/10.1088%2F1748-0221%2F11%2F04%2Fp04011.

[Are+18a] M. Arenz et al. "Calibration of high voltages at the ppm level by the difference of ^{83m}Kr conversion electron lines at the KATRIN experiment". In: *The European Physical Journal C* 78.5 (2018), p. 368. ISSN: 1434-6052. DOI: 10.1140/epjc/s10052-018-5832-y. URL: https://doi.org/10.1140/epjc/s10052-018-5832-y.

[Are+18b] M. Arenz et al. "First transmission of electrons and ions through the KATRIN beamline". In: *Journal of Instrumentation* 13.04 (2018), P04020–P04020. DOI: 10.1088/1748-0221/13/04/p04020. URL: https://doi.org/10.1088%2F1748-0221%2F13%2F04%2Fp04020.

[Ase+11] V. N. Aseev et al. "Upper limit on the electron antineutrino mass from the Troitsk experiment". In: *Phys. Rev. D* 84 (11 2011), p. 112003. DOI: 10.1103/PhysRevD.84.112003. URL: https://link.aps.org/doi/10.1103/PhysRevD.84.112003.

[Bab+12] M Babutzka et al. "Monitoring of the operating parameters of the KATRIN Windowless Gaseous Tritium Source". In: *New Journal of Physics* 14.10 (2012), p. 103046. DOI: 10.1088/1367-2630/14/10/103046. URL: https://doi.org/10.1088%2F1367-2630%2F14%2F10%2F103046.

[Bab14] Martin Babutzka. "Design and development for the Rearsection of the KATRIN experiment". PhD thesis. Karlsruher Institut für Technologie, 2014. URL: https://publikationen.bibliothek.kit.edu/1000045598/3413342.

[Bar+09] I. R. Barabanov et al. *Research of the natural neutrino fluxes by use of large volume scintillation detector at Baksan*. 2009. arXiv: 0908.1466 [hep-ph].

[Bau+13] S. Bauer et al. "Ellipsometry with polarisation analysis at cryogenic temperatures inside a vacuum chamber". In: *Review of Scientific Instruments* 84.12 (2013), p. 123103. DOI: 10.1063/1.4838555. eprint: https://doi.org/10.1063/1.4838555. URL: https://doi.org/10.1063/1.4838555.

[Bau14] Stephan Bauer. "Energy calibration and stability monitoring of the KATRIN experiment". PhD thesis. Westfälische Wilhelms-Universität Münster, 2014. URL: http://nbn-resolving.de/urn:nbn:de:hbz:6-04329567654.

[Beh16] Jan D. Behrens. "Design and commissioning of a mono-energetic photoelectron source and active background reduction by magnetic pulse at the KATRIN spectrometers". PhD thesis. Westfälische Wilhelms-Universität Münster, 2016. URL: http://www.katrin.kit.edu/publikationen/phd_behrens.pdf.

[Ber+15] Johannes Bergstrom et al. "Bayesian global analysis of neutrino oscillation data". In: *JHEP* 09 (2015), p. 200. DOI: 10.1007/JHEP09(2015)200. arXiv: 1507.04366 [hep-ph].

[BHS92] Pijushpani Bhattacharjee, Christopher T. Hill, and David N. Schramm. "Grand unified theories, topological defects, and ultrahigh-energy cosmic rays". In: *Phys. Rev. Lett.* 69 (4 1992), pp. 567–570. DOI: 10.1103/PhysRevLett.69.567. URL: https://link.aps.org/doi/10.1103/PhysRevLett.69.567.

[BK13] Vernon Barger and Wai-Yee Keung. "Superheavy Particle Origin of IceCube PeV Neutrino Events". In: *Phys. Lett.* B727 (2013), pp. 190–193. DOI: 10.1016/j.physletb.2013.10.021. arXiv: 1305.6907 [hep-ph].

[BKE70] M. Berman, H. R. Kerchner, and S. Ergun. "Determination of the Optical Properties of Absorbing Uniaxial Crystals from Reflectance at Oblique Incidence". In: *J. Opt. Soc. Am.* 60.5 (1970), pp. 646–648. DOI: 10.1364/JOSA.60.000646. URL: http://www.osapublishing.org/abstract.cfm?URI=josa-60-5-646.

[Bla06] Klaus Blaum. "High-accuracy mass spectrometry with stored ions". In: *Physics Reports* 425.1 (2006), pp. 1 –78. ISSN: 0370-1573. DOI: https://doi.org/10.1016/j.physrep.2005.10.011. URL: http://www.sciencedirect.com/science/article/pii/S0370157305004643.

[BM14] Richard A. Battye and Adam Moss. "Evidence for Massive Neutrinos from Cosmic Microwave Background and Lensing Observations". In: *Phys. Rev. Lett.* 112 (5 2014), p. 051303. DOI: 10.1103/PhysRevLett.112.051303. URL: https://link.aps.org/doi/10.1103/PhysRevLett.112.051303.

[BP34] H. Bethe and R. Peierls. "The "Neutrino"". In: *Nature* 133.1476-4687 (1934), p. 532. DOI: https://doi.org/10.1038/133532a0. URL: https://www.nature.com/articles/133532a0.

[BPT80] G Beamson, H Q Porter, and D W Turner. "The collimating and magnifying properties of a superconducting field photoelectron spectrometer". In: *Journal of Physics E: Scientific Instruments* 13.1 (1980), pp. 64–66. DOI: 10.1088/0022-3735/13/1/018. URL: https://doi.org/10.1088%2F0022-3735%2F13%2F1%2F018.

[BU88] John N. Bahcall and Roger K. Ulrich. "Solar models, neutrino experiments, and helioseismology". In: *Rev. Mod. Phys.* 60 (2 1988), pp. 297–372. DOI: 10.1103/RevModPhys.60.297. URL: https://link.aps.org/doi/10.1103/RevModPhys.60.297.

[Cha14] J Chadwick. "Intensitätsverteilung im magnetischen Spectrum der β-Strahlen von radium B + C". In: *Verhandl. Dtsc. Phys. Ges.* 16 (1914), p. 383. URL: http://cds.cern.ch/record/262756.

[CKN18] Bhavesh Chauhan, Bharti Kindra, and Ashish Narang. "Discrepancies in simultaneous explanation of flavor anomalies and IceCube PeV events using leptoquarks". In: *Phys. Rev.* D97 (2018).

[Cle+98] Bruce T. Cleveland et al. “Measurement of the Solar Electron Neutrino Flux with the Homestake Chlorine Detector”. In: *The Astrophysical Journal* 496.1 (1998), pp. 505–526. DOI: 10.1086/305343. URL: https://doi.org/10.1086%2F305343.

[Col13] IceCube Collaboration. “Evidence for High-Energy Extraterrestrial Neutrinos at the IceCube Detector”. In: *Science* 342.6161 (2013). ISSN: 0036-8075. DOI: 10.1126/science.1242856. URL: https://science.sciencemag.org/content/342/6161/1242856.

[Cow+56] C. L. Cowan et al. “Detection of the free neutrino: A Confirmation”. In: *Science* 124 (1956), pp. 103–104. DOI: 10.1126/science.124.3212.103.

[CP01] J.L. CAMPBELL and TIBOR PAPP. “WIDTHS OF THE ATOMIC K–N7 LEVELS”. In: *Atomic Data and Nuclear Data Tables* 77.1 (2001), pp. 1 –56. ISSN: 0092-640X. DOI: https://doi.org/10.1006/adnd.2000.0848. URL: http://www.sciencedirect.com/science/article/pii/S0092640X00908489.

[CW99] Michael Catanese and Trevor C. Weekes. “Very high-energy gamma-ray astronomy”. In: *Publ. Astron. Soc. Pac.* 111 (1999), p. 1193. DOI: 10.1086/316435. arXiv: astro-ph/9906501 [astro-ph].

[Dan+62] G. Danby et al. “Observation of High-Energy Neutrino Reactions and the Existence of Two Kinds of Neutrinos”. In: *Phys. Rev. Lett.* 9 (1 1962), pp. 36–44. DOI: 10.1103/PhysRevLett.9.36. URL: https://link.aps.org/doi/10.1103/PhysRevLett.9.36.

[Dey+18] Ujjal Kumar Dey et al. “Searching for Leptoquarks at IceCube and the LHC”. In: *Phys. Rev.* D98.3 (2018), p. 035014. DOI: 10.1103/PhysRevD.98.035014. arXiv: 1709.02009 [hep-ph].

[Dey18] Rajat K. Dey. “PeV neutrinos from local magnetars”. In: *Springer Proc. Phys.* 203 (2018), pp. 147–149. DOI: 10.1007/978-3-319-73171-1_32. arXiv: 1702.01928 [astro-ph.HE].

[DGR16] P. S. Bhupal Dev, Dilip Kumar Ghosh, and Werner Rodejohann. “R-parity Violating Supersymmetry at IceCube”. In: *Phys. Lett.* B762 (2016), pp. 116–123. DOI: 10.1016/j.physletb.2016.08.066. arXiv: 1605.09743 [hep-ph].

[Dre15] G. Drexlin. *Excited Molecules and Atoms as background source*. Tech. rep. Karlsruher Institut für Technologie (KIT), 2015. URL: fuzzy.fzk.de/bscw/bscw.cgi/d950495/95-TRP-5833-D1.3-GDrexlin.pptx.

[Dyb18] S. Dyba. “Background reduction by the inner wire electrode and set-up of the condensed krypton source at the neutrino mass experiment KATRIN”. PhD thesis. Westfälische Wilhelms-Universität Münster, 2018.

[ee03] Guido Altarelli (ed.) and Klaus Winter (ed.) *Neutrino mass*. Springer, 2003.

[Egu+03] K. Eguchi et al. “First results from KamLAND: Evidence for reactor anti-neutrino disappearance”. In: *Phys. Rev. Lett.* 90 (2003), p. 021802. DOI: 10.1103/PhysRevLett.90.021802. arXiv: hep-ex/0212021 [hep-ex].

[EIP12] Arman Esmaili, Alejandro Ibarra, and Orlando L. G. Peres. "Probing the stability of superheavy dark matter particles with high-energy neutrinos". In: *JCAP* 1211 (2012), p. 034. DOI: 10.1088/1475-7516/2012/11/034. arXiv: 1205.5281 [hep-ph].

[Elea] https://elementy.ru/novosti_nauki/432134/Est_li_voobshche_problema_s_kosmicheskimi_pozitronami.

[Eleb] .

[Erg67] S. Ergun. "Determination of Longitudinal and Transverse Optical Constants of Absorbing Uniaxial Crystals–Optical Anisotropy of Graphite". In: *Nature* 213.1476-4687 (1967), pp. 135–136. DOI: https://doi.org/10.1038/213135a0. URL: https://www.nature.com/articles/213135a0.

[Erh+14] M Erhard et al. "High-voltage monitoring with a solenoid retarding spectrometer at the KATRIN experiment". In: *Journal of Instrumentation* 9.06 (2014), P06022–P06022. DOI: 10.1088/1748-0221/9/06/p06022. URL: https://doi.org/10.1088%2F1748-0221%2F9%2F06%2Fp06022.

[Erh+18] M. Erhard et al. "Technical design and commissioning of the KATRIN large-volume air coil system". In: *Journal of Instrumentation* 13.02 (2018), P02003–P02003. DOI: 10.1088/1748-0221/13/02/p02003. URL: https://doi.org/10.1088%2F1748-0221%2F13%2F02%2Fp02003.

[Erh16] Moritz G. Erhard. "Influence of the magnetic field on the transmission characteristics and neutrino mass systematic of the KATRIN experiment". PhD thesis. Karlsruher Institut für Technologie, 2016. URL: http://nbn-resolving.org/urn:nbn:de:swb:90-650034.

[Ess04] K. Essig. "Investigation of the Penning trap between the spectrometers of the KATRIN experiment". PhD thesis. University of Bonn, 2004.

[Fan15] Ke Fang. "High-energy neutrino signatures of newborn pulsars in the local universe". In: *Journal of Cosmology and Astroparticle Physics* 2015.06 (2015), pp. 004–004. DOI: 10.1088/1475-7516/2015/06/004. URL: https://doi.org/10.1088%2F1475-7516%2F2015%2F06%2F004.

[Fer34] E. Fermi. "Versuch einer Theorie der β-Strahlen. I". In: *Zeitschrift für Physik* 88.3 (1934), pp. 161–177. ISSN: 0044-3328. DOI: 10.1007/BF01351864. URL: https://doi.org/10.1007/BF01351864.

[Fis14] Sebastian Fischer. "Commissioning of the KATRIN Raman system and durability studies of optical coatings in glove box and tritium atmospheres". PhD thesis. Karlsruher Institut für Technologie (KIT), 2014. URL: http://nbn-resolving.org/urn:nbn:de:swb:90-436973.

[FMS99] Daniele Fargion, B. Mele, and A. Salis. "Ultrahigh-energy neutrino scattering onto relic light neutrinos in galactic halo as a possible source of highest energy extragalactic cosmic rays". In: *Astrophys. J.* 517 (1999), pp. 725–733. DOI: 10.1086/307203. arXiv: astro-ph/9710029 [astro-ph].

[Frä+11] F.M. Fränkle et al. "Radon induced background processes in the KATRIN pre-spectrometer". In: *Astroparticle Physics* 35.3 (2011), pp. 128 –134. ISSN: 0927-6505. DOI: https://doi.org/10.1016/j.astropartphys.2011.06.009. URL: http://www.sciencedirect.com/science/article/pii/S0927650511001290.

[Fuk+98] Y. Fukuda et al. "Evidence for Oscillation of Atmospheric Neutrinos". In: *Phys. Rev. Lett.* 81 (8 1998), pp. 1562–1567. DOI: 10.1103/PhysRevLett.81.1562. URL: https://link.aps.org/doi/10.1103/PhysRevLett.81.1562.

[Fuk+99] Y. Fukuda et al. "Measurement of the Flux and Zenith-Angle Distribution of Upward Throughgoing Muons by Super-Kamiokande". In: *Phys. Rev. Lett.* 82 (13 1999), pp. 2644–2648. DOI: 10.1103/PhysRevLett.82.2644. URL: https://link.aps.org/doi/10.1103/PhysRevLett.82.2644.

[Ful19] A. Fulst. "doctoral thesis in preparation". PhD thesis. Westfälische Wilhelms-Universität Münster, 2019.

[Gas+17] L. Gastaldo et al. "The electron capture in 163Ho experiment – ECHo". In: *The European Physical Journal Special Topics* 226.8 (2017), pp. 1623–1694. ISSN: 1951-6401. DOI: 10.1140/epjst/e2017-70071-y. URL: https://doi.org/10.1140/epjst/e2017-70071-y.

[Gil+10] Woosik Gil et al. "The cryogenic pumping section of the KATRIN experiment". In: *Applied Superconductivity, IEEE Transactions on* 20 (July 2010), pp. 316 –319. DOI: 10.1109/TASC.2009.2038581.

[GK07] Carlo Giunti and Chung W Kim. *Fundamentals of neutrino physics and astrophysics*. Oxford university press, 2007.

[Gl13] Ferenc Glück et al. "Electromagnetic design of the large-volume air coil system of the KATRIN experiment". In: *New Journal of Physics* 15.8 (2013), p. 083025. DOI: 10.1088/1367-2630/15/8/083025. URL: https://doi.org/10.1088%2F1367-2630%2F15%2F8%2F083025.

[Glu08] Ferenc Glueck. *Background at FPD and the pre-spectrometer potential*. In: *XV KATRIN collaboration meeting*. https://fuzzy.fzk.de/bscw/bscw.cgi/d477645/95-TRP-4518-B1-FGlueck.ppt. 2008.

[GRE+69] D. L. GREENAWAY et al. "Anisotropy of the Optical Constants and the Band Structure of Graphite". In: *Phys. Rev.* 178 (3 1969), pp. 1340–1348. DOI: 10.1103/PhysRev.178.1340. URL: https://link.aps.org/doi/10.1103/PhysRev.178.1340.

[Gre13] Benjamin Grees. "Verbesserung der Nullellipsometrie bei festem Analysatorwinkel für das KATRIN-Experiment". PhD thesis. Westfälische Wilhelms-Universität Münster, 2013. URL: http://www.katrin.kit.edu/publikationen/dth_Benjamin_Grees_2013.pdf.

[Gre66] Kenneth Greisen. "End to the Cosmic-Ray Spectrum?" In: *Phys. Rev. Lett.* 16 (17 1966), pp. 748–750. DOI: 10.1103/PhysRevLett.16.748. URL: https://link.aps.org/doi/10.1103/PhysRevLett.16.748.

[Gro15] Stefan Groh. "Modeling of the response function and measurement of transmission properties of the KATRIN experiment". PhD thesis. Karlsruher Institut für Technologie (KIT), 2015. URL: http://nbn-resolving.org/urn:nbn:de:swb:90-465464.

[Gör14] Stefan Görhardt. "Background Reduction Methods and Vacuum Technology at the KATRIN Spectrometers". PhD thesis. Karlsruher Institut für Technologie (KIT), 2014. URL: http://nbn-resolving.org/urn:nbn:de:swb:90-380506.

[Hac17] Moritz T. Hackenjos. "KATRIN - First Light Commissioning and Modelling of the Beam Line". PhD thesis. Karlsruher Institut für Technologie, 2017.

[Han+17] V. Hannen et al. "Deconvolution of the energy loss function of the KATRIN experiment". In: *Astroparticle physics* 89 (2017). 51.03.01; LK 01, pp. 30–38. ISSN: 0927-6505, 1873-2852. DOI: 10.1016/j.astropartphys.2017.01.010.

[Har15] Fabian Harms. "Characterization and Minimization of Background Processes in the KATRIN Main Spectrometer". PhD thesis. Karlsruher Institut für Technologie (KIT), 2015. URL: http://nbn-resolving.org/urn:nbn:de:swb:90-500274.

[Hil11] Björn Hillen. "Untersuchung von Methoden zur Unterdrückung des Spektrometeruntergrunds beim KATRIN Experiment". PhD thesis. Westfälische Wilhelms-Universität Münster, 2011. URL: http://nbn-resolving.de/urn:nbn:de:hbz:6-22429660310.

[Icd] URL: https://icecube.wisc.edu/news/view/570.

[Ice] URL: https://icecube.wisc.edu/~kjero/Bootcamp/2015/Notebooks/Reconstruction_Introduction.html.

[ITW13] Alejandro Ibarra, David Tran, and Christoph Weniger. "Indirect Searches for Decaying Dark Matter". In: *Int. J. Mod. Phys.* A28 (2013), p. 1330040. DOI: 10.1142/S0217751X13300408. arXiv: 1307.6434 [hep-ph].

[IVA73] S. I. IVANOV. "Formative time of Penning discharge". In: *International Journal of Electronics* 34.6 (1973), pp. 769–775. DOI: 10.1080/00207217308938498. eprint: https://doi.org/10.1080/00207217308938498. URL: https://doi.org/10.1080/00207217308938498.

[JHL07] G. E. Jellison, J. D. Hunn, and Ho Nyung Lee. "Measurement of optical functions of highly oriented pyrolytic graphite in the visible". In: *Phys. Rev. B* 76 (8 2007), p. 085125. DOI: 10.1103/PhysRevB.76.085125. URL: https://link.aps.org/doi/10.1103/PhysRevB.76.085125.

[KA18] Niki Klop and Shin'ichiro Ando. "Effects of a neutrino-dark energy coupling on oscillations of high-energy neutrinos". In: *Phys. Rev.* D97.6 (2018), p. 063006. DOI: 10.1103/PhysRevD.97.063006. arXiv: 1712.05413 [hep-ph].

[KA59] J. Kruger and W. J. Ambs. "Optical Measurements on Thin Films of Condensed Gases at Low Temperatures∗". In: *J. Opt. Soc. Am.* 49.12 (1959), pp. 1195–1198. DOI: 10.1364/JOSA.49.001195. URL: http://www.osapublishing.org/abstract.cfm?URI=josa-49-12-1195.

[Kip19] Luke Kippenbrock. "Investigation of Background from the Inter-Spectrometer Penning Trap and Secondary Electron Emission in the KATRIN experiment". PhD thesis. University of Washington, 2019.

[KK05] KATRIN Collaboration and KATRIN Collaboration. *KATRIN design report 2004*. Tech. rep. 51.54.01; LK 01. Forschungszentrum, Karlsruhe, 2005. 245 pp. DOI: 10.5445/IR/270060419.

[KKK06] H. V. KLAPDOR-KLEINGROTHAUS and I. V. KRIVOSHEINA. "THE EVIDENCE FOR THE OBSERVATION OF $0\nu\beta\beta$ DECAY: THE IDENTIFICATION OF $0\nu\beta\beta$ EVENTS FROM THE FULL SPECTRA". In: *Modern Physics Letters A* 21.20 (2006), pp. 1547–1566. DOI: 10.1142/S0217732306020937. eprint: https://doi.org/10.1142/S0217732306020937. URL: https://doi.org/10.1142/S0217732306020937.

[KKK18] M. Kachelriess, O. E. Kalashev, and M. Yu. Kuznetsov. "Heavy decaying dark matter and IceCube high energy neutrinos". In: *Phys. Rev.* D98.8 (2018), p. 083016. DOI: 10.1103/PhysRevD.98.083016. arXiv: 1805.04500 [astro-ph.HE].

[Kle14] Marco Kleesiek. "A Data-Analysis and Sensitivity-Optimization Framework for the KATRIN Experiment". PhD thesis. Karlsruher Institut für Technologie (KIT), 2014. URL: http://nbn-resolving.org/urn:nbn:de:swb:90-433013.

[Kod+01] K. Kodama et al. "Observation of tau neutrino interactions". In: *Physics Letters B* 504.3 (2001), pp. 218 –224. ISSN: 0370-2693. DOI: https://doi.org/10.1016/S0370-2693(01)00307-0. URL: http://www.sciencedirect.com/science/article/pii/S0370269301003070.

[Kos12] Andreas Kosmider. "Tritium Retention Techniques in the KATRIN Transport Section and Commissioning of its DPS2-F Cryostat". PhD thesis. Karlsruher Institut für Technologie (KIT), 2012. URL: http://nbn-resolving.org/urn:nbn:de:swb:90-289595.

[Kra+05] Ch Kraus et al. "Final results from phase II of the Mainz neutrino mass searchin tritium β decay". In: *The European Physical Journal C - Particles and Fields* 40.4 (2005), pp. 447–468. ISSN: 1434-6052. DOI: 10.1140/epjc/s2005-02139-7. URL: https://doi.org/10.1140/epjc/s2005-02139-7.

[Lou+19] Arthur Loureiro et al. "Upper Bound of Neutrino Masses from Combined Cosmological Observations and Particle Physics Experiments". In: *Phys. Rev. Lett.* 123 (8 2019), p. 081301. DOI: 10.1103/PhysRevLett.123.081301. URL: https://link.aps.org/doi/10.1103/PhysRevLett.123.081301.

[LP06] Julien Lesgourgues and Sergio Pastor. "Massive neutrinos and cosmology". In: *Physics Reports* 429.6 (2006), pp. 307 –379. ISSN: 0370-1573. DOI: https://doi.org/10.1016/j.physrep.2006.04.001. URL: http://www.sciencedirect.com/science/article/pii/S0370157306001359.

[LR12] Cecilia Lunardini and Soebur Razzaque. "High Energy Neutrinos from the Fermi Bubbles". In: *Phys. Rev. Lett.* 108 (2012), p. 221102. DOI: 10.1103/PhysRevLett.108.221102. arXiv: 1112.4799 [astro-ph.HE].

[LS85] V.M. Lobashev and P.E. Spivak. "A method for measuring the electron antineutrino rest mass". In: *Nuclear Instruments and Methods in Physics Research Section A: Accelerators, Spectrometers, Detectors and Associated Equipment* 240.2 (1985), pp. 305 –310. ISSN: 0168-9002. DOI: https://doi.org/10.1016/0168-9002(85)90640-0. URL: http://www.sciencedirect.com/science/article/pii/0168900285906400.

[Luk+12] S. Lukić et al. "Measurement of the gas-flow reduction factor of the KATRIN DPS2-F differential pumping section". In: *Vacuum* 86.8 (2012), pp. 1126 –1133. ISSN: 0042-207X. DOI: https://doi.org/10.1016/j.vacuum.2011.10.017. URL: http://www.sciencedirect.com/science/article/pii/S0042207X11003800.

[Luo+06a] X. Luo et al. "Monte Carlo simulation of gas flow through the KATRIN DPS2-F differential pumping system". In: *Vacuum* 80.8 (2006), pp. 864 –869. ISSN: 0042-207X. DOI: https://doi.org/10.1016/j.vacuum.2005.11.044. URL: http://www.sciencedirect.com/science/article/pii/S0042207X05003891.

[Luo+06b] X. Luo et al. "Monte Carlo simulation of gas flow through the KATRIN DPS2-F differential pumping system". In: *Vacuum* 80 (2006). 51.54.01; LK 02, pp. 864–69. DOI: 10.1016/j.vacuum.2005.11.044.

[MAC14] CARLA and MACOLINO. "RESULTS ON NEUTRINOLESS DOUBLE-BETA DECAY FROM GERDA PHASE I". In: *Modern Physics Letters A* 29.01 (2014), p. 1430001. DOI: 10.1142/S0217732314300018. eprint: https://doi.org/10.1142/S0217732314300018. URL: https://doi.org/10.1142/S0217732314300018.

[Mer+12] S Mertens et al. "Stochastic heating by ECR as a novel means of background reduction in the KATRIN spectrometers". In: *Journal of Instrumentation* 7.08 (2012), P08025–P08025. DOI: 10.1088/1748-0221/7/08/p08025. URL: https://doi.org/10.1088%2F1748-0221%2F7%2F08%2Fp08025.

[MPS16] Nicolas Mileo, Alejandro de la Puente, and Alejandro Szynkman. "Implications of a Electroweak Triplet Scalar Leptoquark on the Ultra-High Energy Neutrino Events at IceCube". In: *JHEP* 11 (2016), p. 124. DOI: 10.1007/JHEP11(2016)124. arXiv: 1608.02529 [hep-ph].

[Mur00] Hitoshi Murayama. "Supersymmetry phenomenology". In: *Proceedings, Summer School in Particle Physics: Trieste, Italy, June 21-July 9, 1999*. 2000, pp. 296–335. arXiv: hep-ph/0002232 [hep-ph].

[Mur07] Kohta Murase. "High energy neutrino early afterglows gamma-ray bursts revisited". In: *Phys. Rev.* D76 (2007), p. 123001. DOI: 10.1103/PhysRevD.76.123001. arXiv: 0707.1140 [astro-ph].

[Mur17] Kohta Murase. "Active Galactic Nuclei as High-Energy Neutrino Sources". In: *Neutrino Astronomy: Current Status, Future Prospects*. Ed. by Thomas Gaisser and Albrecht Karle. 2017, pp. 15–31. DOI: 10.1142/9789814759410_0002. arXiv: 1511.01590 [astro-ph.HE].

[NPZF16] Hiroshi Nunokawa, Boris Panes, and Renata Zukanovich Funchal. "How Unequal Fluxes of High Energy Astrophysical Neutrinos and Antineutrinos can Fake New Physics". In: *JCAP* 1610.10 (2016), p. 036. DOI: 10.1088/1475-7516/2016/10/036. arXiv: 1604.08595 [hep-ph].

[Oli14] K.A. Olive. "Review of Particle Physics". In: *Chinese Physics C* 38.9 (2014), p. 090001. DOI: 10.1088/1674-1137/38/9/090001. URL: https://doi.org/10.1088%2F1674-1137%2F38%2F9%2F090001.

[Ost09] Beatrix Ostrick. "Eine kondensierte ^{83m}Kr-Kalibrationsquelle für das KATRIN-Experiment". PhD thesis. Westfälische Wilhelms-Universität Münster, 2009. URL: http://nbn-resolving.de/urn:nbn:de:hbz:6-91519454708.

[OW08] E W Otten and C Weinheimer. "Neutrino mass limit from tritium β decay". In: *Reports on Progress in Physics* 71.8 (2008), p. 086201. DOI: 10.1088/0034-4885/71/8/086201. URL: https://doi.org/10.1088%2F0034-4885%2F71%2F8%2F086201.

[Pau] W. Pauli. *Offener Brief an die Gruppe der Radioaktiven bei der Gauvereins-Tagung zu Tübingen, Dez 1930.* URL:https://cds.cern.ch/record/83282?ln=fr.

[PD+15] Nathalie Palanque-Delabrouille et al. "Neutrino masses and cosmology with Lyman-alpha forest power spectrum". In: *Journal of Cosmology and Astroparticle Physics* 2015.11 (2015), pp. 011–011. DOI: 10.1088/1475-7516/2015/11/011. URL: https://doi.org/10.1088%2F1475-7516%2F2015%2F11%2F011.

[Pet15] Simon Peters. "Adaption of the PC-Ellipsometry for the Condensed Krypton Calibration Source Setup, Converted for the Operation at the KATRIN-Experiment". Bachelor's thesis. Westfälische Wilhelms-Universität Münster, 2015.

[Pic+92a] A. Picard et al. "A solenoid retarding spectrometer with high resolution and transmission for keV electrons". In: *Nuclear Instruments and Methods in Physics Research Section B: Beam Interactions with Materials and Atoms* 63.3 (1992), pp. 345 –358. ISSN: 0168-583X. DOI: https://doi.org/10.1016/0168-583X(92)95119-C. URL: http://www.sciencedirect.com/science/article/pii/0168583X9295119C.

[Pic+92b] A. Picard et al. "Precision measurement of the conversion electron spectrum of83mKr with a solenoid retarding spectrometer". In: *Zeitschrift für Physik A Hadrons and Nuclei* 342.1 (1992), pp. 71–78. ISSN: 0939-7922. DOI: 10.1007/BF01294491. URL: https://doi.org/10.1007/BF01294491.

[Pra11] Mathias Prall. "Background Reduction of the KATRIN Spectrometers: Transmission Function of the Pre-Spectrometer and Systematic Test of the Main-Spectrometer Wire Electrode". PhD thesis. Westfälische Wilhelms-Universität Münster, 2011. URL: http://www.researchgate.net/publication/238418212_Transmission_Function_of_the_Pre-Spectrometer_and_Systematic_Tests_of_the_Main-Spectrometer_Wire_Electrode_%28PHD_thesis%29.

[Qui96] Chris Quigg. *Neutrinos from topological defects.* 1996. URL: lutece.fnal.gov/Notes/TDnus.ps.

[Rei09] Stefan Reimer. "Ein elektrostatisches Dipolsystem zur Eliminierung von Ionen in der DPS2-F des KATRIN Experimentes". PhD thesis. Karlsruher Institut für Technologie (KIT), 2009. URL: http://www.katrin.kit.edu/publikationen/dth-reimer.pdf.

[Res19] Oliver Rest. "Precision high voltage at the KATRIN experiment and new methods for an absolute calibration at ppm-level for high-voltage dividers". PhD thesis. Westfälische Wilhelms-Universität Münster, 2019. URL: https://www.uni-muenster.de/imperia/md/content/physik_kp/agweinheimer/theses/diss-oliver_rest.pdf.

[RKP15] Carsten Rott, Kazunori Kohri, and Seong Chan Park. "Superheavy dark matter and IceCube neutrino signals: Bounds on decaying dark matter". In: *Phys. Rev.* D92.2 (2015), p. 023529. DOI: 10.1103/PhysRevD.92.023529. arXiv: 1408.4575 [hep-ph].

[RM98] Jorg P. Rachen and P. Meszaros. "Photohadronic neutrinos from transients in astrophysical sources". In: *Phys. Rev.* D58 (1998), p. 123005. DOI: 10.1103/PhysRevD.58.123005. arXiv: astro-ph/9802280 [astro-ph].

[Roy99] Mou Roy. "Ultra high energy neutrinos from supernova remnants". In: *Journal of Physics G: Nuclear and Particle Physics* 25.1 (1999), pp. 129–134. DOI: 10.1088/0954-3899/25/1/011. URL: https://doi.org/10.1088%2F0954-3899%2F25%2F1%2F011.

[Rö+78a] F. Rösel et al. "Internal conversion coefficients for all atomic shells". In: *Atomic Data and Nuclear Data Tables* 21.2 (1978), pp. 91 –289. ISSN: 0092-640X. DOI: https://doi.org/10.1016/0092-640X(78)90034-7. URL: http://www.sciencedirect.com/science/article/pii/0092640X78900347.

[Rö+78b] F. Rösel et al. "Internal conversion coefficients for all atomic shells". In: *Atomic Data and Nuclear Data Tables* 21.4 (1978), pp. 291 –514. ISSN: 0092-640X. DOI: https://doi.org/10.1016/0092-640X(78)90009-8. URL: http://www.sciencedirect.com/science/article/pii/0092640X78900098.

[Sle13] Martin Slezák. "The source of monoenergetic electrons for the monitoring of spectrometer in the KATRIN neutrino experiment." PhD thesis. Karlsruher Institut für Technologie (KIT), 2013.

[Sle15] Martin Slezák. "Monitoring of the energy scale in the KATRIN neutrino experiment". PhD thesis. Charles University in Prague, 2015.

[SM16] Ian M. Shoemaker and Kohta Murase. "Probing BSM Neutrino Physics with Flavor and Spectral Distortions: Prospects for Future High-Energy Neutrino Telescopes". In: *Phys. Rev.* D93.8 (2016), p. 085004. DOI: 10.1103/PhysRevD.93.085004. arXiv: 1512.07228 [astro-ph.HE].

[Sno] "A Combination of preliminary electroweak measurements and constraints on the standard model". In: (2004). arXiv: hep-ex/0412015 [hep-ex].

[Spi11] Daniel Spitzer. "Alternative Ellipsometrie-Varianten bei kryogenen Temperaturen für das KATRIN-Experiment". PhD thesis. Westfälische Wilhelms-Universität Münster, 2011. URL: https://www.uni-muenster.de/Physik.KP/AGWeinheimer/Files/theses/Diplom_Daniel_Spitzer.pdf.

[Sre+99] P. Sreekumar et al. "Gev emission from the nearby radio galaxy centaurus a". In: *Astropart. Phys.* 11 (1999), pp. 221–223. DOI: 10.1016/S0927-6505(99)00054-7. arXiv: astro-ph/9901277 [astro-ph].

[Tan+18] M Tanabashi et al. "Review of Particle Physics: Particle Data Group". In: *Physical Review D* 98 (Aug. 2018).

[Thü07] Thomas Thümmler. "Präzisionsüberwachung und Kalibration der Hochspannung für das KATRIN-Experiment". PhD thesis. Westfälische Wilhelms-Universität Münster, 2007. URL: http://nbn-resolving.de/urn:nbn:de:hbz:6-16539562785.

[TP65] E. A. Taft and H. R. Philipp. "Optical Properties of Graphite". In: *Phys. Rev.* 138 (1A 1965), A197–A202. DOI: 10.1103/PhysRev.138.A197. URL: https://link.aps.org/doi/10.1103/PhysRev.138.A197.

[TRM05] Diego F. Torres, Gustavo E. Romero, and Felix Mirabel. "Neutrinos from microquasars". In: *Chin. J. Astron. Astrophys.* 5 (2005), S133–S138. DOI: 10.1088/1009-9271/5/S1/183. arXiv: astro-ph/0407494 [astro-ph].

[V+̈76] S. Väisälä et al. "Levels of ^{83}Kr populated in the decay of ^{83}Rb and ^{83}Br". In: *Phys. Rev. C* 13 (1 1976), pp. 372–376. DOI: 10.1103/PhysRevC.13.372. URL: https://link.aps.org/doi/10.1103/PhysRevC.13.372.

[Val09] Kathrin Valerius. "Spectrometer-related background processes and their suppression in the KATRIN experiment". PhD thesis. Westfälische Wilhelms-Universität Münster, 2009. URL: http://nbn-resolving.de/urn:nbn:de:hbz:6-28479494638.

[VWZ] P. Vogel, L.J. Wen, and C. Zhang. "Neutrino oscillation studies with reactors". In: *Nature Communications* (). ISSN: 2041-1723. DOI: 10.1038/ncomms7935.

[Vé+06] D. Vénos et al. "Precise energy of the weak 32-keV gamma transition observed in 83mKr decay". In: *Nuclear Instruments and Methods in Physics Research Section A: Accelerators, Spectrometers, Detectors and Associated Equipment* 560 (May 2006), pp. 352–359. DOI: 10.1016/j.nima.2005.12.213.

[Wan+13] N Wandkowsky et al. "Validation of a model for radon-induced background processes in electrostatic spectrometers". In: *Journal of Physics G: Nuclear and Particle Physics* 40.8 (2013), p. 085102. DOI: 10.1088/0954-3899/40/8/085102. URL: https://doi.org/10.1088%2F0954-3899%2F40%2F8%2F085102.

[Wan13] Nancy Wandkowsky. "Study of background and transmission properties of the KATRIN spectrometers". PhD thesis. Karlsruher Institut für Technologie (KIT), 2013. URL: http://nbn-resolving.org/urn:nbn:de:swb:90-366316.

[WBB98] M. S. Westley, G. A. Baratta, and R. A. Baragiola. "Density and index of refraction of water ice films vapor deposited at low temperatures". In: *The Journal of Chemical Physics* 108.8 (1998), pp. 3321–3326. DOI: 10.1063/1.475730. eprint: https://doi.org/10.1063/1.475730. URL: https://doi.org/10.1063/1.475730.

[Weg10] Anne Wegmann. "Laserellipsometrie für die kondensierte ^{83m}Kr-Konversionselektronenquelle des KATRIN-Experiments". PhD thesis. Westfälische Wilhelms-Universität Münster, 2010. URL: https://www.uni-muenster.de/Physik.KP/AGWeinheimer/Files/theses/Diplom_Anne_Wegmann.pdf.

[Wei99] Thomas J. Weiler. "Cosmic ray neutrino annihilation on relic neutrinos revisited: A Mechanism for generating air showers above the Greisen-Zatsepin-Kuzmin cutoff". In: *Astropart. Phys.* 11 (1999), pp. 303–316. DOI: 10.1016/S0927-6505(98)00068-1. arXiv: hep-ph/9710431 [hep-ph].

[WL01] Eli Waxman and Abraham Loeb. "TeV Neutrinos and GeV Photons from Shock Breakout in Supernovae". In: *Phys. Rev. Lett.* 87 (7 2001), p. 071101. DOI: 10.1103/PhysRevLett.87.071101. URL: https://link.aps.org/doi/10.1103/PhysRevLett.87.071101.

[WS97] A. Widom and Yogendra Srivastava. "Charged Lepton Oscillations and (g-2) Measurements". In: (Jan. 1997).

[Wu+57] C. S. Wu et al. "Experimental Test of Parity Conservation in Beta Decay". In: *Phys. Rev.* 105 (4 1957), pp. 1413–1415. DOI: 10.1103/PhysRev.105.1413. URL: https://link.aps.org/doi/10.1103/PhysRev.105.1413.

[Yoo+08a] Jung-Sik Yoon et al. "Cross Sections for Electron Collisions with Hydrogen Molecules". In: *Journal of Physical and Chemical Reference Data* 37.2 (2008), pp. 913–931. DOI: 10.1063/1.2838023. eprint: https://doi.org/10.1063/1.2838023. URL: https://doi.org/10.1063/1.2838023.

[Yoo+08b] Jung-Sik Yoon et al. "Cross Sections for Electron Collisions with Hydrogen Molecules". In: *Journal of Physical and Chemical Reference Data* 37.2 (2008), pp. 913–931. DOI: 10.1063/1.2838023. eprint: https://doi.org/10.1063/1.2838023. URL: https://doi.org/10.1063/1.2838023.

[Zac09] Michael Zacher. "Electromagnetic design and field emission studies for the inner electrode system of the KATRIN main spectrometer". MA thesis. Westfälische Wilhelms-Universität Münster, Jan. 2009. URL: https://www.uni-muenster.de/Physik.KP/AGWeinheimer/theses/Diplom_Michael_Zacher.pdf.

[Zac15] Michael Zacher. "High-field electrodes design and an angular-selective photoelectron source for the KATRIN spectrometers". PhD thesis. Westfälische Wilhelms-Universität Münster, 2015.

[Zbo+13] M Zbořil et al. "Ultra-stable implanted83Rb/83mKr electron sources for the energy scale monitoring in the KATRIN experiment". In: *Journal of Instrumentation* 8.03 (2013), P03009–P03009. DOI: 10.1088/1748-0221/8/03/p03009. URL: https://doi.org/10.1088%2F1748-0221%2F8%2F03%2Fp03009.

[Zbo11] Miroslav Zbořil. "Solid electron sources for the energy scale monitoring in the KATRIN experiment". PhD thesis. Westfälische Wilhelms-Universität Münster, 2011. URL: http://nbn-resolving.de/urn:nbn:de:hbz:6-91469497689.

[ZK66] G. T. Zatsepin and V. A. Kuzmin. "Upper limit of the spectrum of cosmic rays". In: *JETP Lett.* 4 (1966). [Pisma Zh. Eksp. Teor. Fiz.4,114(1966)], pp. 78–80.

[ZM18] B. Theodore Zhang and Kohta Murase. *Ultrahigh-energy cosmic-ray nuclei and neutrinos from engine-driven supernovae*. 2018. arXiv: 1812.10289 [astro-ph.HE].

[Gil+10] W. Gil et al. "The Cryogenic Pumping Section of the KATRIN Experiment". In: *IEEE Transactions on Applied Superconductivity* 20.3 (2010), pp. 316–319. DOI: 10.1109/TASC.2009.2038581.

[Gil+12] W. Gil et al. "Status of the Magnets of the Two Tritium Pumping Sections for KATRIN". In: *IEEE Transactions on Applied Superconductivity* 22.3 (2012), pp. 4500604–4500604. DOI: 10.1109/TASC.2011.2175353.

[How+04] M. A. Howe et al. "Sudbury neutrino observatory neutral current detector acquisition software overview". In: *IEEE Transactions on Nuclear Science* 51.3 (2004), pp. 878–883. ISSN: 0018-9499. DOI: 10.1109/TNS.2004.829527.

[Pla+14] Planck Collaboration et al. "Planck 2013 results. XVI. Cosmological parameters". In: *A&A* 571 (2014), A16. DOI: 10.1051/0004-6361/201321591. URL: https://doi.org/10.1051/0004-6361/201321591.

[Zub11] K. Zuber. *Neutrino Physics, Second Edition*. Aug. 2011. DOI: 10.1201/b11065.